Effect of Dispersion Method on the Thermal and Wear Properties of Graphene Nano Platelet Filler Modified Polyurethane

By:

Mohammad Rizwan Al-Rahman

A thesis submitted in partial fulfillment of the requirements for the degree of

Master of Science

Department of Mechanical Engineering

University of Alberta

Abstract

Polyurethane is used in various applications, for example as liner for piping systems, pipelines, pressure vessels and valve trims, where it may be subjected to elevated temperature as well as high rate of erosion. At elevated temperatures, polyurethane erodes at a faster rate. In this research, the aim was to investigate the erosive wear and improve the thermal conductivity of polyurethane and find a correlation between the thermal and wear properties of polyurethane that is reinforced by graphene. Two different dispersion methods (Three Roll Milling and Sonication Dispersion) were explored to find their effect on the overall thermal and wear performance of polyurethane, as well as the quality of distribution and exfoliation of the graphene filler nanoparticles. Thermal conductivity and wear performance of polyurethane at elevated temperatures were evaluated and compared for both three roll milling and sonication dispersion process separately. Experiments were performed with a filler loading ranging from 0% to 4% by weight and at temperatures of 22ºC, 60ºC and 100ºC. Dispersion by three roll milling method provided a higher degree of alignment, as determined by characterizing the samples using XRD analysis and SEM imaging, compared to that under sonication method. The alignment of graphene particles affected the thermal conductivity of polyurethane, which resulted in an anisotropic higher thermal conductivity in the axial direction. Overall, a higher thermal conductivity was achieved with an increase in graphene filler content. The bulk isotropic thermal conductivity of the samples prepared by three roll milling method also increased for all the three tested temperatures with increase in filler loading. However, with an increase in temperature, there was no noticeable change in the thermal conductivity. With temperature rising from 22ºC to 100ºC, the erosion rate of pure polyurethane increased by nearly 30-fold. By embedding graphene as a reinforcement, the final erosion rate, when compared to that of pure polyurethane at 100°C, was reduced by 76.14% when using three roll milling method for dispersion, and by 71.3% when using sonication process for dispersion. This suggests that samples prepared by three roll milling method demonstrated better performance with respect to wear due to reinforcing particles being aligned in the through thickness direction in the samples. Evaluation of the surface morphology indicated that the pure polyurethane samples underwent ductile erosion with plastic deformation. By dispersing graphene, the mode of erosion had a ductile to brittle transition. Thus, it was found that graphene can be used as a reinforcement to increase the wear performance of polyurethane at elevated temperatures. Thus, this finding also opens new possibilities for use of polyurethane in other applications.

Table of Contents

List of Figures

List of Tables

Nomenclature and Abbreviations

Symbols:

Cp	Specific heat capacity (J/kgK)
E	Erosion (mg/g)
q	Local Heat Flux Density (W/m)
k	Thermal conductivity (W/m-K)
C	Volumetric Heat Capacity (J/m^3K)
v	Phonon Velocity (m/s)
l	Mean Free Path Length (m)
n	Positive integer
Q	Heat flux (W)
SA	Surface area (m^2)
T	Temperature (°K)
ΔT	Temperature gradient (°K)
V	Volume (m^3)
v	Velocity (m/s)
W	Weight (kg)

Greek Symbols:

θ	Diffraction angle (°)
λ	Wavelength of impinging X-Ray beam (m)
α	Attack angle (°)

Subscripts:

D	Deformation
C	Cutting
N	Normal
T	Tangential
P	Particle
3RM	Three-Roll Mill

S	Sonication

Abbreviation:

GNP	Graphene nanoplatelets
PU	Polyurethane polymer
GNP-PU	Graphene reinforced polyurethane nanocomposite
3RM	Three-Roll Mill
S	Sonication
XRD	X-ray diffraction
TDI	Toluene diisocayanate
MDI	Diphenylmethane diisocyanate
NDI	Naphthalene diisocyanate
TPS	Transient plane source
M	Mass
DSC	Differential scanning calorimetry
SEM	Scanning electron microscopy
FRPC	Fiber reinforced polymer composites
PMC	Polymer matrix composites
CNT	Carbon nanotubes
MWCNT	Multi wall carbon nanotube
DMTDA	Di(methylthio)toluenediamine
MEK	Methyle ehyle ketone
DMF	Dimethyleformamide
wt	Weight
WAXD	Wide angle X-ray diffraction

1. Introduction:

In the petrochemical, mining, agricultural and manufacturing industries, handling of two-phase fluids with solid particles causes accelerated degradation of the surfaces of various structures and equipment due to corrosion and abrasion/erosion-induced wear. These include piping, drill strings, valve trims, pumps, heat exchangers, hoppers, chutes, and other structures. Over time, this wear process greatly depreciates the life and efficiency of the equipment and structures, and increases operation costs [1]. The life of these structures can sometimes be prolonged in various ways, at the cost of shutting down the operation to perform preventive maintenance, such as by rotating sections of pipelines on a regular basis, replacing with more resilient materials, or implementing piping layout design changes to improve flow geometries [2]. These damage processes can be mitigated by using polymer liners such as those made from polyurethane [3]. Plastic and rubber piping systems also experience similar wear in high temperature environments [4][5]. However, as shown by previous research by Ashrafizadeh et al, the properties of polyurethanes are strongly affected by temperature, and the desirable wear characteristics diminish in elevated temperature environments [6]. Hot fluids, heat input from pumps and motors attached to piping, and even heat generated within liners from friction of viscous fluids flowing at high velocity, may cause the temperature of a polymer pipe liner to increase. Since polyurethanes are poor heat conductors as compared to metallic components, its applications are limited to low temperature environments. Therefore, this research project explores the usage of highly thermally conductive graphene nanoplatelets to reinforce and increase the thermal conductivity and erosive wear resistance of polyurethane for the use as materiel for liners. Previous research by Akram et al [7] has already that polyurethane's thermal conductivity can be enhanced by using infused graphene by sonication method. Hence, this research will further investigate how dispersion by three-roll milling will influence the thermal conductivity and wear rate, and how that compares to the erosion and wear performance of nanocomposites prepared by sonication method.

2. Objectives:

This study has the following three objectives:

- To enhance the thermal conductivity of polyurethane by embedding nano-graphene platelets;
- To enhance the erosive wear characteristics of polyurethane at elevated temperatures by embedding nano-graphene platelets for use as liners for piping systems;
- To investigate the effect of different dispersion techniques, such as sonication and three roll milling on alignment, settling, thermal conductivity and erosive wear of graphene nano platelet nanocomposite polyurethane materials.

3. Literature Review:

3.1. Polymer Materials:

Polymers, or plastics, are a complex form of engineering materials. Examples of naturally occurring polymers include silk, wool, DNA, cellulose and proteins. Examples of synthetic polymers are polyurethane, nylon, polyethylene, polyester, Teflon (polytetrafluoroethylene) and epoxy. Polymers get their broad range of properties from their chemical structure, which is composed of macromolecular chains [[8]–[11]]. The atoms are fixed in place by covalent bonds (sharing of electron pairs between atoms) within the macromolecules. The chain links are connected through temperature dependent dipoles (attraction due to difference in electronegativity), hydrogen bonds (weak bond between proton of one molecule to an electronegative atom of another) and Van Der Waals bonds (weak distant dependent interaction between atoms or molecules). The macromolecules are formed by the polymerization (linking) process of organic units known as monomers. The polymerization process can take place by either addition of monomers through double or triple carbon bonds, which is known as chain growth, or through condensation of monomers, which is known as step growth. Step growth is the stepwise reaction between functional groups of monomers [[9], [10], [12]]. The polymerization process goes through the free radical formation step first, also known as the initiation step, followed by the propagation step, where there is no change in free radical, and finally the termination step where there is a decrease in the number of free radicals. The polymers' physical properties are dependent on how the chains are linked, whether they are linear with end to end links, or branched with side chains. This affects the molecules' degree of freedom [[9], [12], [13]]. Properties such as mechanical strengths and melting temperatures are elevated by an increase in degree of polymerization, which is the average number of monomer units in a chain molecule [14]. Polymers can be classified into different categories.

Thermosetting polymers are composed of crosslinked chains that are bonded by covalent bonds. Once cured (polymerized), they harden and take a permanent molded shape. Curing is initiated by application of heat or catalysts. Once a thermoset polymer is cured, further elevation of temperature can cause thermal degradation or decomposition, instead of re-melting, which can deteriorate the material properties. However, due to the cross linking of the molecules in a thermoset, they are typically more brittle. With less crosslinking, they become more elastic [15]. Thermoplastic polymers are composed of linear chain links. Compared to thermosets, thermoplastics generally have a higher form of crystallinity (regularity), with slightly varying lengths of chains. With elevated temperatures, thermoplastics can be repeatedly melted and

solidified by cooling. Elastomers, such as rubber, are a form of thermoset polymers that have pronounced viscoelastic properties, but very weak intermolecular forces, leading to typically lower strength. Synthetic fibers are a form of long chain polymers that are made through chemical synthesis by extruding process. Examples of synthetic fibers are Kevlar and Nylon.

The intermolecular forces of the polymer chains weaken with increase in temperature. This increases the chain mobility and is known as relaxation. The relaxation mechanisms vary depending on the temperature as well as the chemical structure. With elevated temperatures, thermoplastics can be repeatedly melted and solidified by cooling [[11], [12]]. During heating, at a certain temperature point, the rate of thermal expansion of amorphous polymer can be seen to change at a different rate. This temperature is known as the glass transition temperature, at which the molecules in the amorphous region in the polymer can rearrange itself without any external forces. The glass transition temperature, if measured in Kelvin, is generally at 60% of the melting temperature of the polymer. Above the glass transition temperature, the polymer is ductile solid, and elastomers are more elastic [9], [11], [12], [16].

Due to the varying degree of physical properties attainable with synthetic polymers, they are now widely used in a broad range of applications ranging from commercial usage for consumer items such as plastic bottles, tires, food packaging, clothing, sporting equipment etc. to industrial usage such as optical fibres, electrical and heat insulators, valves, seals, gaskets, piping system and corrosive resistant coating.

3.2. Polyurethane:

Polyurethanes (PU) can be either a thermoset or a thermoplastic polymer. PU, an organic group of polymer joined by carbamate (urethane) links, are regularly used in everyday lives. PU were initially developed by Otto Bayer and his team in I.G. Farben in the 1930s. During that time, it was primarily used as a rubber substitute for foams and coatings during World War II [[15]–[20]]. Now, applications for PU include, but are not limited to, apparels, appliances, automotive, mining, structural integrity, building construction, composite wood, electronics, flooring, furnishing, marine, medical and packaging. PU is proving to be more and more useful regularly due to its many desirable attributes such as wide range of tailorable hardness, high load bearing capacity, flexibility, abrasion and impact resistance, tear resistance, resistance to swelling, strong bonding, low density, ease of manufacturing, cost and energy savings, high elasticity, low thermal and electrical conductivity, and capability of forming into fine threads [[21]–[26]]. The wide variety of applications for PU comes from their broad spectrum of properties that can be achieved due to their type and degree of cross linking.

The name polyurethane comes from the Urethane group (-NH-CO-O-), as shown in Figure 1. Polyols, isocyanate, and the curative/chain extender are the three main building blocks of PU [[10], [16], [27]–[33]]. The two main types of polyols are polyethers and polyesters. The polyols are responsible for the flexibility of PU. PU derived from polyether have lower toughness and strength but have higher stability against reaction with water [[30], [34]]. Hardness of PU comes from the isocayanates [[18], [30], [34]]. Isocayanates used in castable PU are 2,4-toluene diisocayanate (TDI), diphenylmethane-4,4'-diisocyanate (MDI), and napthalene diisocyanate (NDI) [[16], [18], [28]–[30], [35]]. TDI has the greatest technical importance out of the three and is most widely used [36]. Typically, TDI can be obtained as a mixture of 2,4- and 2,6- isomers at a ratio of 80:20.

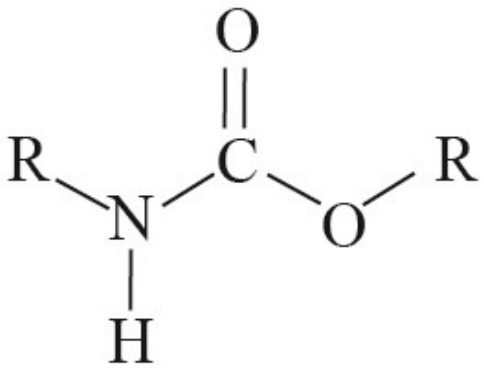

Figure 1: A urethane group

Although in the building construction and petroleum industry, the load bearing and pressure bearing components are primarily metal, polymers such as PU are starting to gain wider usage. Compared to metals, PU have lower density, are easier to form into complex shapes, require lower energy and labor input, have higher chemical and wear resistance, and lower modulus of elasticity [[23], [26], [30], [34]]. PU can also be used for absorbing shock and reducing noise. But poor thermal conductivity of PU often causes heat building up that leads to material degradation. Replicating the desirable properties of PU can be achieved by utilising rubber, but this involves costlier and more complicated processing steps, as well as reduction in load bearing capacity and wear resistance [[25], [34], [37]]. The capability of producing thicker cross-sections more effortlessly with PU is their main advantage over other polymers. Their ease of processing, material properties and wide range of proven usage makes PU highly desirable as matrix for composite materials [38].

3.3. Nanocomposites:

Composite materials are the combination of distinct materials that are insoluble with each other and typically have significantly different properties, with the objective of achieving more desirable properties of the composite over the individual constituents. The main continuous bonding component of composite materials is classified as the matrix. The reinforcing fillers are dispersed into the matrix, and these are either particles in particle-reinforced composites, or fibers, in fiber-reinforced composites [[9], [39]–[42]]. Nanocomposites are materials that are made of two or more components where at least one of the components are in nanometer scale [[43], [44]]. The purpose of the filler materials is to enhance certain properties of the nanocomposite that is low or non-existent in the matrix. The filler modifiers can be either particulate in shape, fibrous or layered, as shown in Figure 2 [[45]–[47]]. In addition to mechanical properties such as fracture toughness, tensile strength, modulus of elasticity and abrasion resistance, other properties such as electrical and thermal conductivity, permeability, flame retardation, bacterial resistance can also be enhanced by filler loading [[44], [48]].

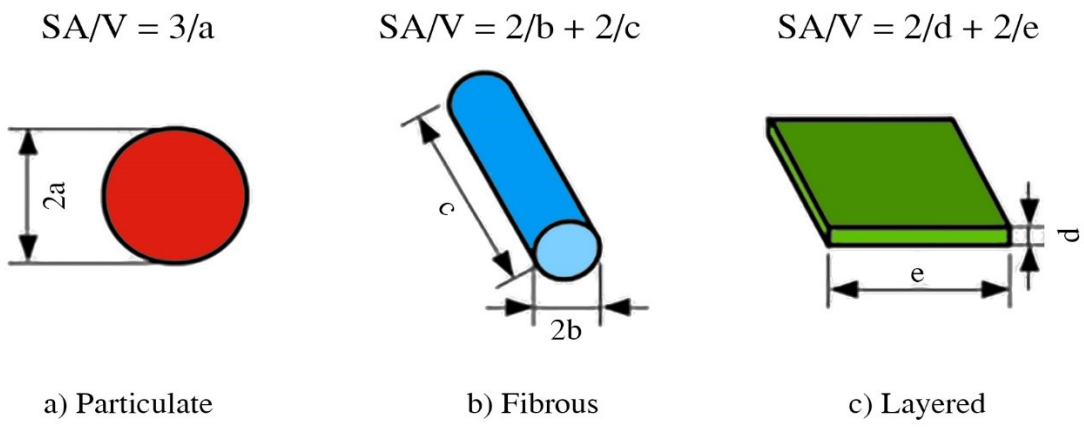

Figure 2: Filler modifier shapes and their surface area to volume ratio (SA/V), where a, b, c, d and e are filler characteristic's dimensions (adapted from [45])

Metals, ceramics and polymers are the three main types of nano composite matrix materials. This research project focuses on the usage of polymer as the matrix due to the above-mentioned advantages of polymers, mainly polyurethane. Depending on the final desired properties, a suitable material is chosen for usage as the filler material. Different types of filler materials are metallic such as copper or silver, ceramic such as boron nitride or silicon carbide, or carbon based, such as carbon black [[46], [47], [49]–[51]]. Optimum

combined properties of nanocomposites are derived not only from the individual properties of the matrix and fillers, but also from the interaction between the matrix and filler.

Parameters such as filler shape, filler size, filler loading amount, matrix type, distribution, and dispersion can affect the final property of the nanocomposite material. The level of surface interaction between the reinforcement fillers and the surrounding matrix governs the amount of modification of properties of the combined nanocomposite material [[52]–[56]]. Higher contact area between the filler material and the matrix leads to more property transfer from the filler material to the nanocomposite material. Thus, nanocomposites, compared to macro or micro scale filler composite materials, can have superior properties, because they have higher surface area per unit volume for the same percentage by weight quantity of filler. This is shown in Figure 2 and can be seen that as the size decreases, the ratio of surface area to volume increases. Thus, a higher property transfer is achieved at the same level of filler loading percentage by using smaller filler particles [[46], [57]–[66]]. It can also be seen from the shape comparison that fibrous and layered filler gives higher contact ratio compared to particulate fillers. Similarly, higher filler concentrations lead to higher filler-matrix surface interaction, that leads to more property transfer [[60], [67]–[70]]. An even distribution of the reinforcement particles through out the matrix gives a homogenous nanocomposite that can be described as fully distributed. When the filler particles are fully separated from one another, it is then known as fully dispersed or exfoliated, as shown in Figure 3. Fully exfoliated fillers are desirable as they give higher surface interaction with the matrix, thus cause better property enhancement of the composite material. However, this is more difficult to achieve, as described in a later section.

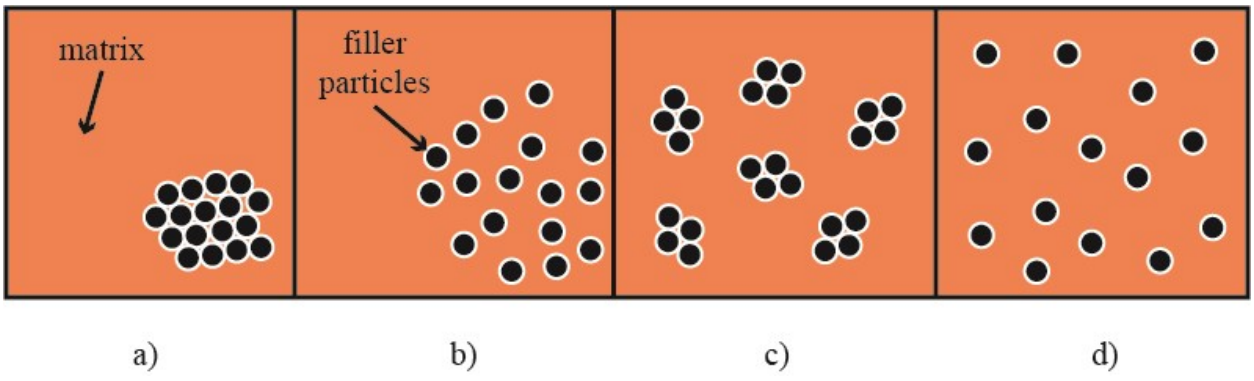

Figure 3: (a) Poor dispersion and distribution, (b) good dispersion but poor distribution, (c) good distribution but poor dispersion, (d) good dispersion and distribution

3.4. Graphene Nano Particles:

Carbon, chemical element with symbol C, is the fourth most abundant element in the universe by mass. The atoms of carbon tend to bond together in unique ways that is termed as allotropes of carbon, and these allotropes of carbon each have uniquely different properties. Graphite, diamond and amorphous carbon are the most common allotropes. Graphite is naturally occurring and is made up of overlapping layers of two-dimensional sheet of carbon bonded in a hexagonal lattice. Graphene is a single atomic layer of such carbon atoms in honey comb lattice [[71], [72]]. It was only in 2004 that researchers first succeeded in obtaining and examining graphene. [73] In 2009, graphene was shown to be the strongest material to be ever tested, with a tensile strength and Young's modulus of respectively 130 GPa and ~1 TPa. Graphene also has a low density of 1.5 g/cm^3 and is very efficient in conducting heat and electricity.

Carbon nanotubes (CNT) and graphene nanoplatelets (GNP) are the two most widely used nano-sized carbon allotropes used for reinforcing polymers. Intermolecular forces such as Van Der Waals forces act between single layers of graphene. Thus, each GNP can consist of tens of monoatomic layers. Due to a comparatively strong attractive intermolecular force, separating each layer of graphene to produce a properly dispersed nanocomposite structure can be difficult. Even after exfoliating the nanoparticles applying external forces, re-agglomeration can often take place due to the intermolecular forces [[74], [75]]. Multi-layered graphene nanoplatelet sheets have been reported to have an average thickness of 5 nm and a diameter of about 5 to 20 μm [76]. [[77], [78]]. A single layer graphene has a thickness of 0.335 nm, and the length of the carbon-carbon sp2 hybridized bond in two-dimensional planar monolayer of graphene is 0.142 nm. Due to this two-dimensional shape, GNP displays anisotropic behaviour in properties such as toughness, strength, optical performance, electrical and thermal conductivity. Thus, when GNP are used as the filler in nanocomposites, a high degree of alignment of the GNP within the matrix can raise the anisotropic behavior of the whole nanocomposite material [[49], [79], [80]]. Despite the anisotropic behaviour, GNP still prove to be a very promising filler modifier for nanocomposites due to their superior mechanical properties, higher exposed surface area and lower manufacturing costs compared to other filler materials.

Depending on the application, GNP can be more favourable as compared to CNT, not only because of lower cost, but also because GNP have lower density. This makes them more feasible for commercial high-volume production. Furthermore, CNT only conduct heat effectively in one direction (one-dimensional) where as

GNP are effective in conducting heat in two directions (two-dimensional); this gives GNP superior bulk thermal conductivity [43]. With an increased amount of filler loading, GNP also maintain a lower viscosity of the blend compared to CNT, which makes nanocomposite processing easier with GNP [81]. Also, due to the surface interaction as described before, GNP can potentially be a better choice as filler material than CNT.

3.5. Nanocomposite Preparation Procedures

Due to the varying types of matrix and filler types used to make nanocomposites, different combinations of fabrication and dispersion methods are used accordingly. Considerations must be made for factors such as the desired level of dispersion, curing time (pot life), curing temperature of the matrix resin and viscosity of a solution. Slight variations in temperature, or duration of each step, can affect polymerization process or the degree of dispersion, and thus affect the final property of the nanocomposites. Therefore, preparation of nanocomposite materials can be intricately challenging due to the required precision involved. Higher filler loading leads to higher viscosity of blends and solutions as well which raises difficulty in fabrication of nanocomposites. Higher filler loading may also lead to more re-agglomeration due to higher Van Der Waals force as particles are closer together [[67], [69], [75], [82], [83]]. This has been reported to cause reduction of polymer properties such as toughness.

When the matrix is a thermoset, in-situ polymerization is often used to mix the filler and matrix [84]. In many cases, the nanoparticles are first dispersed into the monomer of the polymer resin. During this step, as the viscosity rises with increase of filler loading, temperature may be elevated, or solvents may be added to lower the viscosity of the solution and promote filler dispersion and distribution [85]. The hardener, Part B, is then added to the mixture and left to cure either at room temperature or elevated temperature [[84], [86], [87]]. By having the fillers dispersed into the monomers, when covalent bonds start to form to create cross-linked chains of the thermoset polymer matrix, it may also do so in-between filler particles, instead of only around it. This can reduce re-agglomeration and lead to better surface interaction [[84], [87]].

Instead of dispersion in the monomer, the filler may also be dispersed in a solvent first, and then the mixture can be mixed with the resin. This method is known as solution mixing and it is a widely used fabrication method [[84], [87], [88]]. This method is often favourable as the dispersion of the fillers is effective in the solvent due to polarity and low viscosity of the solvent. The surface tension of the liquid may also help to

exfoliate the graphene by minimizing the interfacial tension between fillers. In the case of GNP, the solvent surface tension must be higher than that of GNP which has a surface tension of 34.4 mN/m. For this reason, solvents such as DMF (Dimethyleformamide) are often used, having a surface tension of 37.1 mN/m [[89]–[92]]. After dispersion, the solvent should be removed quickly to avoid filler re-agglomeration or settling. This can be done by curing at a high elevated temperature to evaporate the solvent or curing in a vacuum chamber to lower the evaporation temperature. To make this procedure less difficult, a solvent with a low boiling temperature should be selected.

3.5.1. Dispersion Methods

The most common methods used to disperse nanoparticles in polymer are mechanical agitation, ultra-sonication and three roll milling. Ball milling is another method that may be used; however, this method has been reported to be damaging to filler particles. For this research, one focus is to compare thermal and wear performance between nanocomposites prepared by ultrasonication and three roll milling.

3.5.1.1. Mechanical Agitation

Mechanical agitation involves the usage of one or multiple high-speed impellers to create shear forces that mix the solution as well as disperse the filler materials. Parameters such as rotational speed, time, temperature and impeller type effect the final dispersion quality [[84], [93]]. Mechanical agitation can be followed by other methods of dispersion in conjunction with it. This is because re-agglomeration has been reported following mechanical agitation, and the dispersion quality of the nanoparticles is not as good as what can be achieved by either ultrasonication or three roll milling [94], [95].

3.5.1.2. Ultrasonication

For research purposes, ultrasonication is a widely used process to disperse nanoparticles due to its proven results and ease of use [[68], [80], [84], [96]–[100]]. In this process, ultrasonic frequency vibrational energy is applied to the nanoparticles. This energy input helps peel off individual layers bonded by the Van Der Waals forces. The applied ultrasonic wave also help to stir and distribute filler particles throughout the solution or liquid [93]. This is very effective when a solution has a low viscosity. Thus, for resins with high

viscosity such as polyurethane, temperature must be controlled or solvents such as acetone or MEK may be used to reduce viscosity [84].

A solution or blend can be sonicated by either an ultrasonic probe, or ultrasonic bath. Ultrasonic baths typically require more energy as they vibrate the whole volume of material, however they provide an even application of vibrational energy. Ultrasonic probes provide more concentrated energy, which can generate a large amount of localised heating. It has been shown by Tessema et al [98] that ultrasonication can increase thermal conductivity in nanocomposites. It is important to control the amplitude or duration of the ultrasonic vibration because it has also been reported that a large amount of concentrated heat or vibration can damage GNP [[96], [101]]. Such disintegration of GNP particles lowers their desirable properties and consequently reduces the overall properties of the nanocomposites [[84], [96]]. Furthermore, re-agglomeration proceeding ultrasonication can still potentially be an issue with this dispersion method if the rheology is not controlled. And although this is a proven dispersion method in small scale research, for large scale applications or production line manufacturing, ultrasonication is hardly feasible. Ultrasonication does not actively align the nanoparticles during the dispersion method, although some degree of alignment may occur after the dispersion method due to intermolecular forces or when the particles settle due to gravity.

3.5.1.3. Three Roll Milling

Three Roll Mills (3RM) are machines with three rollers that have smooth surfaces and are spaced at small distances apart. They spin in opposite directions to each other at different speeds to create shear forces to mix and disperse materials that are fed into the mill. This method is also known as calendaring. The spacing between the rollers, rotation speed and temperature of the rollers are variables that can be controlled. Three roll mills with micrometer scale gaps are most used for nanoparticle dispersion. Other variations such as single roll mill to five roll mills also do exist, with much larger spacing and size of rollers for industrial scale applications. To achieve a higher degree of dispersion, a solution or blend can be repeatedly fed into the three-roll-mill with the spacing between the mills decreased each consecutive time. Similarly, in manufacturing production lines, a mixture can be fed through several of such three roll milling machines in series. In comparison to ultrasonication, three roll milling can provide uniform shearing of the entire volume of the material.

The smallest gap that can be achieved by the three roll mills are between 1 to 5 micro meters [102], which is in the order scale of the diameter of a graphene nanoplatelet. Due to the high shear forces during the calendaring process, generated heat may raise the temperature of the mixture. Therefore, temperature needs to be monitored and controlled, as well as solvents may be used to control the rheology of the mixture. Calendaring is often used for thermoplastic polymers or to disperse fillers in liquid polymers or oligomers of thermosetting matrices which can be later polymerized.

By using the 3RM technique, it has been reported that for a GNP/silicone composite, 18% improvement in thermal conductivity was achieved for a 25 wt % loading of commercially available GNP [103]. Other experiments have shown a thermal conductivity increase of 6% for 1 wt % filler loading and 14% increase for 2 wt % filler loading of GNP in epoxy by using 3RM technique for dispersion [104]. These tests were performed below the glass transition temperature of epoxy, and in this experiment, the percolation threshold was 0.3 wt % filler loading at which the electrical and thermal conductivity had decreased. GNP/epoxy nanocomposite prepared by 3RM technique had showed three orders of higher electrical conductivity compared to sonication and high shear mixing at similar filler loading. Due to the high shear forces and the narrow microchannel through which the fillers are passed through in the 3RM method, depending on the shape of the filler particles, it is possible to obtain highly dispersed and aligned nanofillers [105]. Research experiments with multi-walled carbon nanotubes (MWCNT) with high aspect ratios have shown that at moderate filler loading of 2 to 4 wt %, 3RM may induce extended alignment. However, at high filler loading, the viscosity of the mixture becomes too high and this does not allow particles to align. The alignment was noted for the MWCNT of aspect ratios (length to diameter) from 94.4 to 289.4. Alignment was not achieved for any aspect ratios below that range.

3.6. Thermal Conductivity

Conduction is the transfer of heat energy in a material. Heat always flows from high temperature to low temperature. This phenomenon is governed by first law of thermodynamics. Fourier law describes the relation between conduction and the temperature gradient as

$$q = -k * \Delta T \quad (1)$$

where q is the local heat flux density, k is thermal conductivity coefficient and ΔT is the temperature gradient [106]. The thermal conductivity, which may be measured in W/mK (watt per meter kelvin), is a measure of the amount of heat energy that can be transferred through a material through conduction. The higher the thermal conductivity, the faster the heat flows through that material, and this is a property of the material. Copper, for example, has a very high thermal conductivity of 400 W/mk, which is why it is used in heat sinks and heat exchangers. PU foams on the other hand, have a very low thermal conductivity of 0.02 W/mK, and are often used for building insulation. Materials with high thermal conductivity typically also have high electrical conductivity, which is the measure of a material's ability to conduct electrical charge.

Electrons and phonons are the energy carriers which enable solid materials to transport heat [107]. In metals, the majority of heat transfer is due to free electron transfer. In polymers, due to the absence of free electrons, the majority of the heat transfer is due to phonons [108]. Phonons are the minute vibration or excitation of atoms or molecules in a lattice structure due to applied energy that can spread through the material [[46], [109], [110]]. When heat energy is applied to a material, the closest atom begins to vibrate. This vibration energy is transferred to the next atom and so on through the material. Thus, in polymers, it takes longer for heat to transfer as they have a disordered atomic structure, and hence the path of energy transfer is longer. This phenomenon explains why polymers typically have low thermal conductivity [109], but with more crystalline structure, higher thermal conductivity can be achieved, and those polymers with amorphous structure have lower thermal conductivity. This is because crystalline structures enable quicker phonon transfer through a shorter path. Other than the lattice structure, impurities, chemical constituents, degree of polymerization and phonon scattering (that occurs at interfaces of lattice structure) can lead to a decrease of thermal conductivity.

Graphene has free electrons present for heat transfer, but like polymers, majority of the heat transfer takes place due to phonons. But unlike polymers, graphene has a highly organised hexagonal two-dimensional lattice structure as described before. Thus, its thermal conductivity is much more superior to polymers. GNP have a thermal conductivity in the range of 3000 to 5000 W/mK in the in-plane direction. This is superior even to metals such as copper (400 W/mK) or cast iron (58 W/mK) [[48], [77], [88], [109], [111], [112]]. The bonding between each of the layers of GNP are due to weaker Van Der Waals forces, whereas covalent bonds exist in the lattice of each layer in the in-plane direction. Hence, there exist interfaces between each layer of the platelet. Therefore, GNP displays anisotropic behaviour and the thermal conductivity in the through-plane direction of the GNP is much lower at 6 W/mK [[109], [112]–[114]].

The mean free path can be described as the average length of a path covered by phonon between each consecutive phonon scattering [115]. Debye-Equation describes the mathematical equation for calculating thermal conductivity in solids [[116], [117]]. This formula, as shown in Eq. 2, shows that the thermal conductivity is directly proportional to the volumetric heat capacity, C, the phonon velocity, v, and the mean free path, l.

$$k = C * v * l/3 \quad (2)$$

The mean free path in GNP is about 600 nm whereas the mean free path of most polymers is in the single digit nanometer range [[118]][[119]]. The mean free path is lower in polyurethane due to phonon scattering from defects or boundaries between amorphous and crystalline zones [[46], [49], [110], [114]], resulting in low thermal conductivity. Chemical structure, degree of polymerization, structural defects, and processing conditions are also some of the other factors that can affect the overall thermal conductivity in polymers.

3.6.1. Thermal Conductivity in Nanocomposites

There are three main parameters that affect the degree of enhancement of thermal conductivity in nanocomposites. They are the type of filler and polymer material, the morphology, and the interaction between the filler and polymer. The type of filler and polymer material is important because the thermal conductivity varies for different filler material types as well as the material of the matrix, thus the combined thermal conductivity of the nanocomposite is dependent upon the individual thermal conductivity of the filler and the matrix. The morphology or shape of filler is of interest, particularly in GNP, as GNP display anisotropic thermal conductivity, which in turn can be replicated in the whole nanocomposite if alignment

of GNP is achieved [120]. The interaction between the filler and polymer is the most important factor that influences the enhancement of thermal conductivity [49]. The interfacial interaction between GNP and polymer is quite low due to the chemically inert surface that GNP possess. Hence, phonon scattering takes place at interfaces due to the discrepancy between phonon vibration modes. This phonon scattering at the interface, which is known as Kapitza resistance, is believed to be the main limiting factor in enhancement of thermal conductivity in nanocomposites [[49], [79], [100], [104], [113], [121]–[126]].

Percolation threshold is the critical value below which long range connectivity of the matrix through the filler does not exist. By increasing the filler loading in the matrix, the average inter-platelet distance decreases. A thermal conduction pathway may be created by increasing the filler loading above the percolation threshold, as shown in Figure 4. In such a case, phonon scattering can be minimized because the heat transfer primarily takes place in the graphene. Hence, by reducing the distance between graphene platelets, a high number of pathways can be introduced to increase thermal conductivity [49].

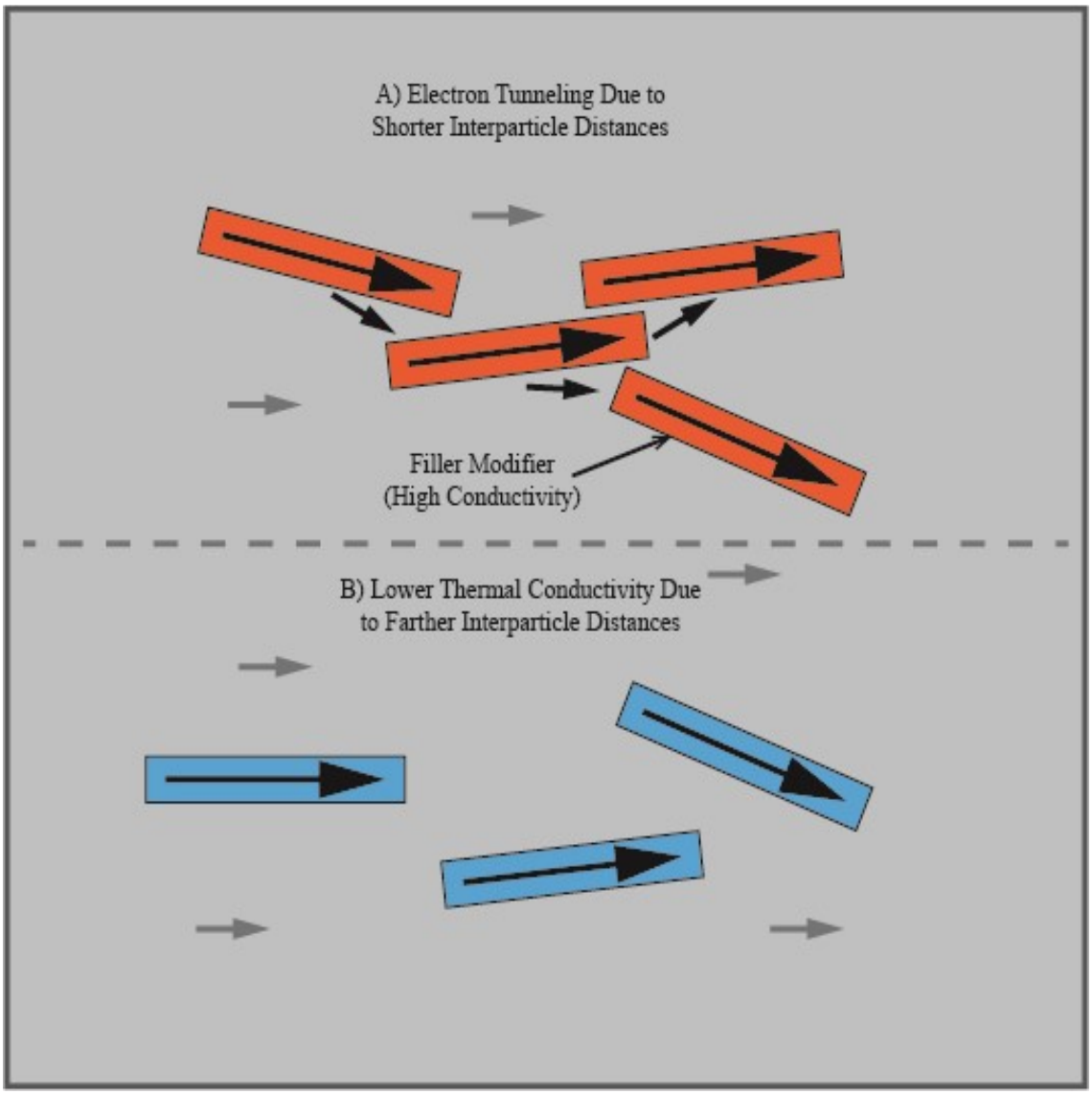

Figure 4: Graphical representation of percolation threshold for thermal conductivity

However, a high filler loading may not always be feasible due to cost or difficulty in processing from high viscosity. In such cases, and for cases below percolation, chemically functionalised GNP may be used. Chemically functionalised GNP have covalent and non-covalent bonds in between the GNP and polymer. This interface interaction reduces phonon scattering that typically occurs in conventional filler modified nanocomposites. Thus, thermal conductivity of the nanocomposite can be increased [[124], [127]–[132]].

3.6.2. Thermal Conductivity Measurement

Thermal conductivity can be measured in either steady state conditions, where the material is in complete equilibrium, or non-steady state conditions, where the measurements are taken when the material is being heated. Examples of non-steady state thermal conductivity measurements include the transient hot wire method, transient plane source method, transient line source method, laser flash method, 3ω-method and time-domain thermoreflectance method. The hot disk transient plane source method can be used to measure thermal conductivity of flat surfaces with high accuracy. It uses a disk-shaped sensor, as shown in Figure 5, which is both a heat source as well as a resistance temperature sensor. The sensor is made from nickel wire that is double spiralled and isolated by Kapton covers. To measure the thermal conductivity, the sensor is usually placed between two identical samples. It must be ensured that there is full contact and no air gaps in between the sensor and sample material. The sensor probe heats the sample, and with a data acquisition module, the temperature increase is measured as a function of time. Based on the heating rate of the sample from the known amount of heat energy applied, the thermal conductivity and thermal diffusivity can be determined. The hot disk method can find both thermal diffusivity and thermal conductivity and can be used to measure properties of inhomogeneous and/or anisotropic materials [133]. They can also offer the ability to measure in small samples, and measurements are in general fast. On top of its accuracy, and ease of set up and measurement, the hot disk method has a wide thermal conductivity measurement range (0.5 to 500 W/mK) and does not damage the sample [[134], [135]]. The hot disk method can be used to measure anisotropic thermal conductivity if the sample specific heat capacity is known. Since the power and time can be controlled, the probing depth, which is the measurement of how much the heat travels through the sample, can also be controlled by this method.

Figure 5: Hot disk transient plane source disk shaped sensor

3.7. Erosive Wear

Erosive wear is the gradual deformation or degradation of the surface of a material due to impact from solid particles in gas or liquid. Over time, the striking particles cut away and remove the material from the exposed surface. Piping systems are prone to erosive wear when transporting fluid with solid particles [[136]–[138]]. Although pipelines also wear due to corrosion, erosion is the main cause for wear in pipelines from slurry transportation. Variables such as the impacting particles' shape, size, hardness, velocity, impingement angle and the eroded surface property effect the rate of erosion of the material [139]. Through many research experiments, it has been found that ductile materials erode the most at 30° impingement angle between the eroding surface and erodent particles whereas brittle materials erode most at above 60° impingement angle as shown in Figure 6 [140].

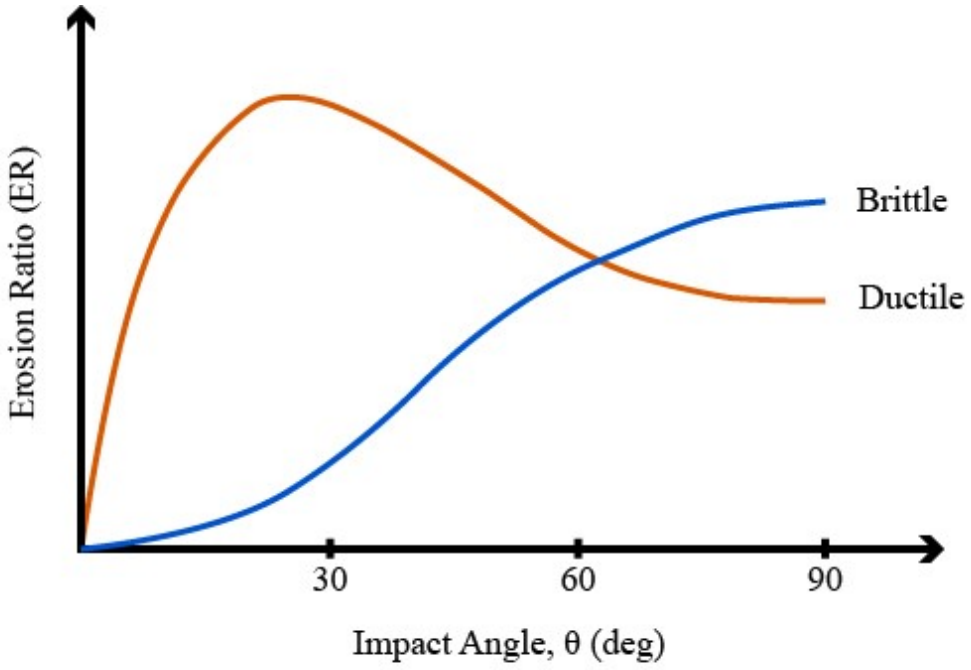

Figure 6: Effect of impact angle on erosion rate (adapted from [141])

3.7.1. Erosion Mechanisms

For both brittle and ductile materials, erosion occurs by a combination of cutting and deformation. The cutting mechanism is caused by the velocity component of the striking particle in parallel to the eroding surface. If particles possess sufficient energy, it may tear loose surface material. The deformation mechanism is caused by the velocity component of the striking angle that is perpendicular to the eroding surface. With sufficient kinetic energy, particles can cause plastic deformation or cracks at stresses higher than the yield strength of the material [[142]–[144]]. According to Clark and Wong [[145], [146]], the total erosion E_T, can be expressed as a function of the deformation erosion, E_D, and cutting erosion, E_C, according to the equation below:

$$E_T = E_D + E_C \quad (3)$$

Where E_D and E_C are represented as :

$$E_D = (\tfrac{1}{2} M_P (V_N^2))/ \varepsilon \quad (4)$$

$$E_C = (\tfrac{1}{2} M_P (V_T^2 \sin 2\alpha))/ \varphi \quad (5)$$

V_N and V_T are the normal and tangential velocity components of the eroding particles with an angle of attack α, and M_P is the total mass of the impacting particles. ε and φ are related to the specific energy required for deformation erosion and cutting erosion; These constants need to be determined experimentally as they depend on the test conditions. However, Eq. 3 to Eq. 5 do not reflect the dependence of erosion on the material property.

The ductility of an eroded material has been reported by many authors to be the main material property that dictates how it will erode [[142], [144], [147], [148]]. Hence, based on the surface material property, erosion can be categorised into ductile erosion and brittle erosion. Ductile erosion from particles at an angle causes cutting whereas at an angle perpendicular to the surface, it creates craters and fracture. Brittle erosion on the other hand, creates a web network of subsurface cracks as shown in Figure 7. Material can experience a combined erosion mechanism simultaneously, or one may be predominant based on the surface material's property.

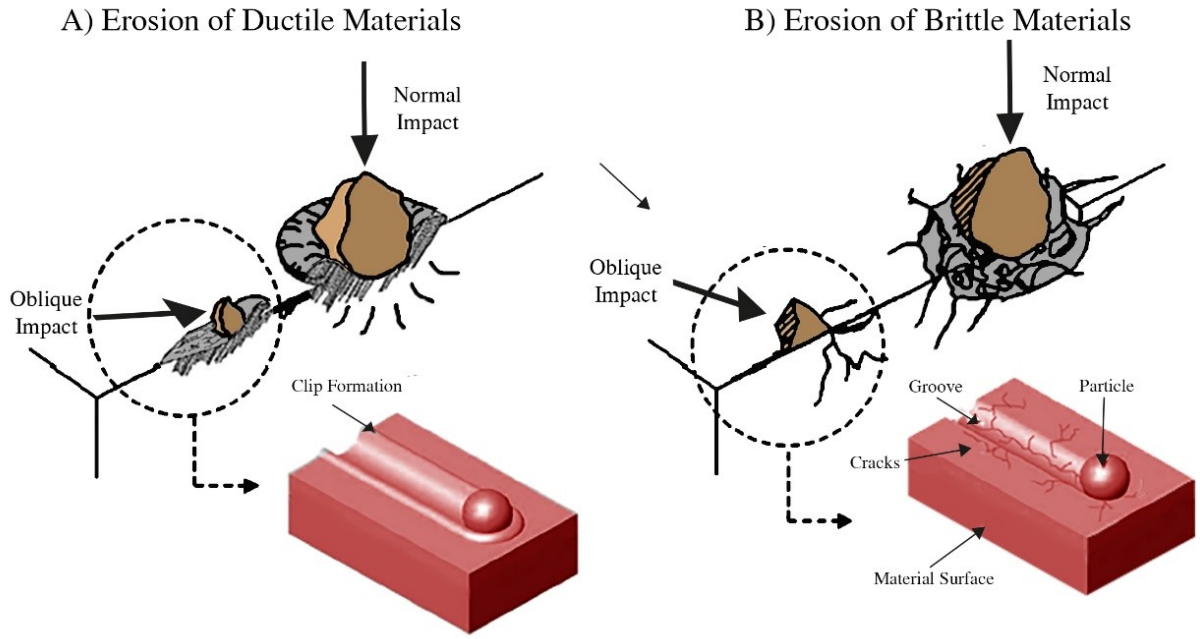

Figure 7: Difference between ductile and brittle erosion (adapted from [139])

3.7.2. Erosion of Polyurethane

Polyurethane liners are frequently used in pipelines to protect them from erosion caused by solid particles. It has been previously noted that temperature distribution within PU, whether it is due to operating temperature of the piping system or friction, affects the wear resistance of the PU. To this day, no direct link between thermal conductivity and wear resistance in PU has been established although it can be attributed to many other complex variables which are temperature dependent. Previous research has shown that for a temperature increase from 25°C to 100°C, the erosion rate increased by up to 170% for pure PU [6]. For two PU samples with similar tensile and tear strengths, Ping et al showed that the respective difference in erosion rate between them can be due to a difference in elongation at break of the two samples [149]. Even with similar hardness, different PU have also shown to have different erosion rates [150]. Other studies such as that by Li et al [151] have shown that for materials with similar rebound resilience but increasing hardness, tensile modulus and tensile strength, erosion rate increased. Softer materials with lower tensile strengths eroded less. Contradicting results from other studies showed that there is no clear correlation between the wear rate of rubber elastomers and their mechanical properties [152]. Instead, higher rebound resistance was shown to correlate to higher erosion resistance. With increase in temperature, PU experiences large changes in mechanical properties. It has been shown that at elevated temperatures, the ultimate strength and the elastic modulus of PU decreases [6]. For rubber, it has been reported that higher the temperature difference between the erosion test temperature and glass transition temperature of the rubber, the lower is the erosion rate [[153], [154]].

Polyurethane, due to its complex long chain structure, can have both plastic deformation and elastic behaviour when load is applied. This arises from irreversible breakage of some of the cross-chain links that form polyurethane. Plastic deformation creates residual stresses in areas and gives rise to hysteresis. Hysteresis, which is the fractional energy lost as heat energy in a deformation cycle in polymer, is a factor that affects the erosion rates in PU. The hysteresis from cyclic stress-strain loading can elevate the sample temperature, and for PU, higher hysteresis has been observed to lead to higher erosion rate [[155], [156]]. As described before, erosion of any material is composed of both a ductile and brittle mechanism, and hysteresis in PU can alter the mechanism of erosion in PU. Since it is indicative that higher temperature increase in polyurethane leads to higher erosion rates, for PU liners to last longer, methods to maintain a lower temperature within the PU during operation should be explored. With many researches indicating that temperature elevation effects the erosive wear rate of PU negatively [[156], [157]], it becomes apparent to find indirect methods to mitigate elevation of temperature within PU to lower erosion rate.

3.7.3. Erosion in Polymer Matrix Composite Materials

Because of their excellent mechanical properties, composite materials have been used as structural materials in numerous applications such as piping for hydraulic or pneumatic transportation, and turbine and helicopter blades. In these applications, failure due to erosion is a critical failure mode. Due to greater and earlier usage of fiber reinforced composite materials, research in erosion testing of fiber reinforced composites is more extensive than that of nanoparticle reinforced composite materials. Erosion characteristics of composite materials are more complex compared to their neat matrix materials. Tilly and Sage were one of the first to experiment on and present solid particle erosion on polymer matrix composite materials [[158]–[160]]. Their studies showed that glass fiber or carbon fiber reinforcement of Nylon reduced the erosion resistance. However, steel particles embedded in ethylene propylene improved the erosion resistance. A comprehensive study of erosion mechanism by Zahavi and Schmitt [161] revealed that in fiber reinforced composites, material is firstly removed in the matrix resin which eventually exposes the fibers. Over time, the reinforced fibers break due to bending failure from the impacting particles and unsupported matrix underneath. Otherwise, the reinforcement fibers wear away slowly and exposes the matrix underneath which erodes quicker. Erosion tests performed on epoxy based unidirectional glass fiber reinforced polymer composites with irregular silica sand at various eroding angles have demonstrated that the erosion mechanism changes from ductile to brittle at 60° impingement angle between solid particles and the eroding surface, at which the erosion loss was the highest [143]. Erosion modelling of multiple angle of attack of solid particles on reinforced composites has revealed that at certain angles, there exists particle-to-particle interaction, which effects the erosion rate [159]. Particles hitting the eroding surface reflect at angles determined by the exposed surface morphology and reinforcement type. These reflected particles in turn collide with other incoming particles and changes the attack angle and reduce the kinetic energy of the subsequent eroding particles.

Previous research on erosive wear performance of nanoparticle reinforced polymer matrix has yielded promising results. Polyurethane matrix composites with aluminum oxide of up to 64 wt % reinforcement has shown that by increasing particle reinforcement, the erosion wear resistance increased. However, further increase in filler loading started to deteriorate the erosive wear performance [[26], [162]]. This increase in erosive wear resistance was attributed to an increase in hardness with particle reinforcement. Epoxy resins reinforced with low graphene oxide contents of 0.05% to 0.5% by weight exhibited remarkable wear resistance enhancement with increase in filler loading. On top of enhancements in flexural strengths, flexural modulus and impact strength, at 0.5 wt % filler loading, wear rate reduced by up to 95%

when compared to neat epoxy [158]. Unsaturated polyester containing vapor grown carbon fiber nano-filler up to 5 wt % reinforcement had previously been erosion tested with 11.5 micrometer erodent particles from angles of 15° to 90°. Other experiments have shown that the erosion rate of the nanofiller reinforced material was much lower than neat unsaturated polyester [162]. Zhao et al had performed solid particle erosion tests on nano-silica particle filled polyacrylate-based nanocomposite coatings with both sharp and round edged erodent particles [162]. Filler content was up to 50%, and erosion tests revealed that both the neat polymer resin and nanocomposite coatings underwent brittle erosion. Compared to neat polymers, the nanocomposite coatings were able to withstand erosion much better with higher filler content against the sharp-edged erodent particles. However, the erosion rate was unaffected by increasing the filler loading percentage when eroded with round edged erodent particles. Alignment of the filler nanoparticles can also affect the erosion rate of nanoparticle reinforced composite materials [163]. Erosion tests performed at different impingement angles on carbon nanotube reinforced epoxy composites had shown that vertically aligned CNT eroded the least. Isotropic, or randomly dispersed, carbon nanotubes (CNT) eroded the most. Horizontally aligned CNT eroded the second most, at a larger rate than neat epoxy. In this experiment, all the samples exhibited ductile erosion behaviour and had the highest erosion rate at 30° to 45° impingement angles. Since isotropic CNT reinforcement degraded the erosion resistance of the material, it is important to consider alignment of the reinforcing filler when designing composite materials for erosion services. The presence of filler reinforcement hinders the mobility of polymer chains during the curing stage and thus effects the final cross-linked structure of the polymer matrix. Examination of the eroded surface morphology suggests that erosion rate had decreased due to the presence of the vertically aligned CNT fillers that prevented cutting, chipping, crack formation and deformation of the matrix by the impact of the solid particles. Due to the impact of the solid particles, the horizontally aligned CNT that is exposed on the eroding surface would de-bond and wear away from the matrix and ultimately leave long cavities of non-reinforced matrix, which results in greater wear and mass loss of the composite material.

3.7.4. Method for Erosion Testing

A standard method for erosion testing by solid particle impingement has been developed by ASTM G76 [164]. This method has been used as a screening test for ranking material erosion rates under simulated environments. According to ASTM G76, the erosion test is done by impinging consistent sized abrasive particles into the test specimen with the aid of pressurised gas flowing through a nozzle. The apparatus to be used for this testing allows for controlling the particle velocity, impact angle and distance of the nozzle from the eroding sample. The minimum dimension of the sample is to be 10 mm X 30 mm X 2 mm in terms of width, length and thickness respectively. The test particles must be nominal 50-um Al_2O_3. The top surface of the sample must be 10mm±1mm from the end of the nozzle. The data collection process involves measuring the mass of the sample before and after the erosion test, as well as measuring the mass of eroding particles that were used. The erosion rate is thus given by dividing the loss of mass of sample material, by the mass of solid particles used.

3.8. Characterisation

Nanocomposites with excellent property enhancement are typically found in materials that are both homogenous and isotropic. Hence, it is desirable to have uniform filler distribution as well as high dispersion of filler particles within the matrix [[83], [93], [98], [99], [101], [111], [165]]. A uniform distribution is achieved when the filler particles are evenly spread throughout the nanocomposite material, whereas the highest degree of dispersion is achieved when the particles are fully exfoliated. Varying property enhancements are achievable with the degree of dispersion. In 'phase separated' dispersion, the filler particles are still agglomerated, whereas in 'intercalated dispersion', the polymer chains develop through individual particle agglomerates. As explained before, higher degrees of dispersion lead to better surface interaction between the filler and matrix [[44], [86]]. As dispersion and distribution relates to two different arrangement mechanisms of the filler particles, it must be clearly differentiated that a nanocomposite material with fillers well dispersed does not mean it is also well distributed, and vice versa, as previously shown in Figure 3.

Other than re-agglomeration, which affects the homogeneity of the nanocomposite, issues such as settling, and alignment can also occur during the fabrication of a nanocomposite material. This can greatly affect the bulk properties of the final nanocomposite. Settling is when filler particles sink to the bottom of a

solution or blend during the curing process due to the effects of gravity. Alignment, which is more of an issue with two-dimensional filler such as GNP, is when the filler particles orient themselves in a specific direction, leading to anisotropic properties within the nanocomposite. Since with increase in filler loading, the nanocomposite structure becomes less transparent, and the particle sizes are in the nano to micro scale, visual or microscopic inspection for agglomeration, settling or alignment are not always practical. Thus, more advanced techniques for structural property characterization should be used.

3.8.1. Scanning Electron Microscopy

Scanning electron microscopy (SEM) is the usage of high energy electrons in a focused beam to scan the surface of solid specimens [166]. Reflected electrons and secondary radiation can provide information such as surface morphology, chemical composition, crystalline structure and orientation of the materials. SEM instruments such as the EVO MA10 Scanning Electron microscope (SEM) (Zeiss, Oberkochen, Germany) can provide details of up to 2000 times magnification with enough contrast and clarity in the nano-meter scale to detect nano-particles [167]. SEM can be used as a complementary tool in conjunction with other methods to verify the quality of dispersion of nano particles [168]. Although SEM is not suitable for bulk characterisation since its field of view is narrow, it is a good tool to make sample point characterisations. In cases where the surface is not electrically conductive, conductive coating such as gold needs to be applied to the surface. This conductive layer on the surface inhibits charging, reduces thermal damage, and improves the secondary electron signal which can help to increase the image contrast between the nanofillers and the matrix.

3.8.2 X-Ray Diffraction

X-ray Diffraction (XRD) technique utilises X-ray beams projected on to a sample at different angles, and then analyse the reflected scattered beams. The X-rays are generated by a cathode ray tube, filtered to produce monochromatic radiation. X-ray diffraction is based on constructive interference of monochromatic X-rays. Graphical representation of the amplitude (intensity) of the reflected wave over the range of angle can be used to characterise the sample. XRD analysis is often preferred over microscopy techniques since it can provide the ability to analyse a greater volume of material.

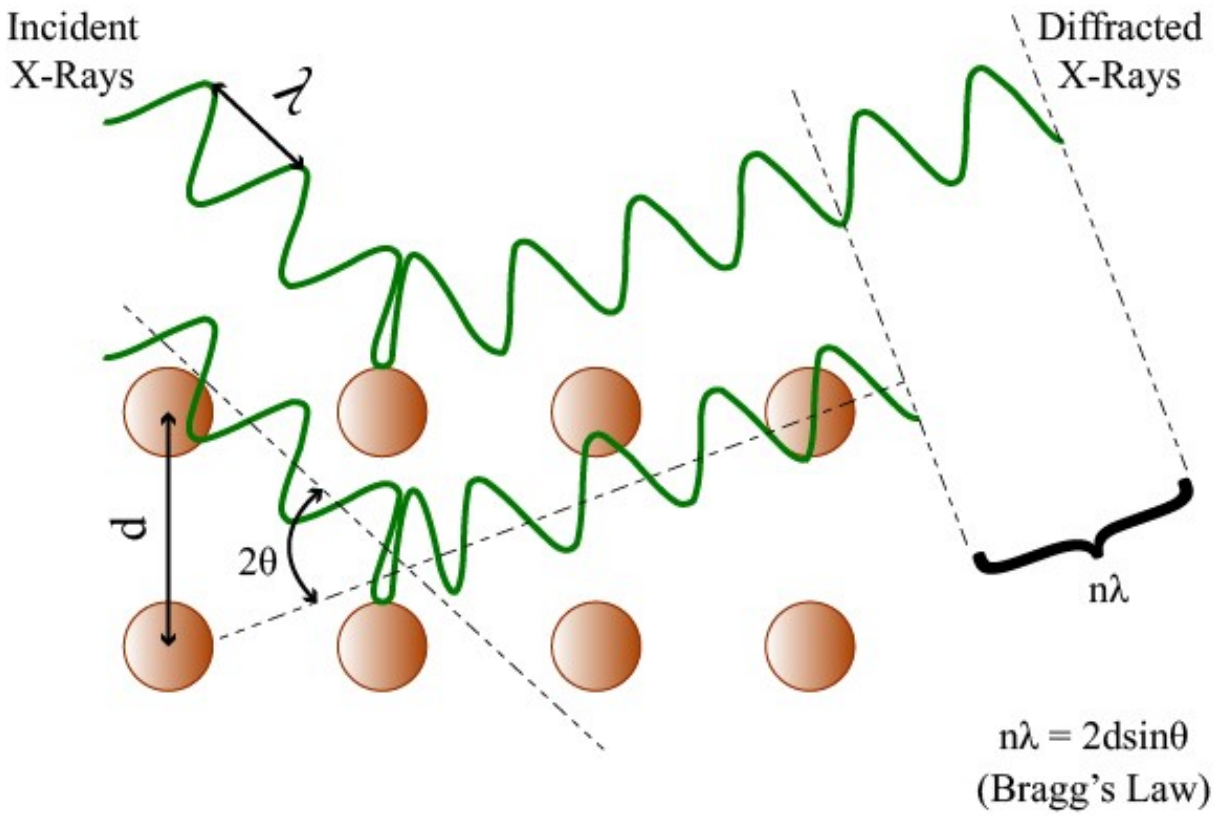

Figure 8: Schematic figure showing XRD diffraction scattering

X-ray scattering typically has a wavelength in the range of around 0.1 nm [169]. When waves of the same frequency are out of phase by one full cycle, one of the waves will be lagging by one full wavelength. Thus, the peaks of the wave coincide to create constructive waves. By Following Bragg's law, incident X-ray radiation produces a Bragg peak due to the constructive interference of the reflected waves from different crystal lattice planes with a d-spacing between them as explained schematically in Figure 8 [170]. The relationship between the wavelength of the X-ray, λ, the d-spacing between the crystal lattice planes, d, and the diffracted intensity and angle, Θ, is given by Eq. 6 as follows:

$$n\lambda = 2d\sin\theta \quad (6)$$

where *n* is a positive integer. Crystalline materials show a sharp peak in XRD analysis whereas amorphous materials do not show any peaks. XRD analysis spectrum of a material consisting of different compositions can be predicted by superimposing the XRD analysis spectrum of the individual components in the material. Since the X-ray wavelength is in the nano-meter scale, and due to the similar scale of d-spacing in GNP, XRD analysis is suitable for differentiating between the different degrees of dispersion within the matrix. Unmodified GNP or graphite usually shows a clear peak, where as properly exfoliated GNP do not display

any peaks on the graph as shown in Figure 9. By this method, one can determine whether the filler GNP platelets inside a nanocomposite sample of known substances has been completely exfoliated [86]. When the diffraction peaks occur at angles larger than 2°, wide-angle X-ray diffraction (WAXD) technique can be used to analyse features that are in the nano-meter scale.

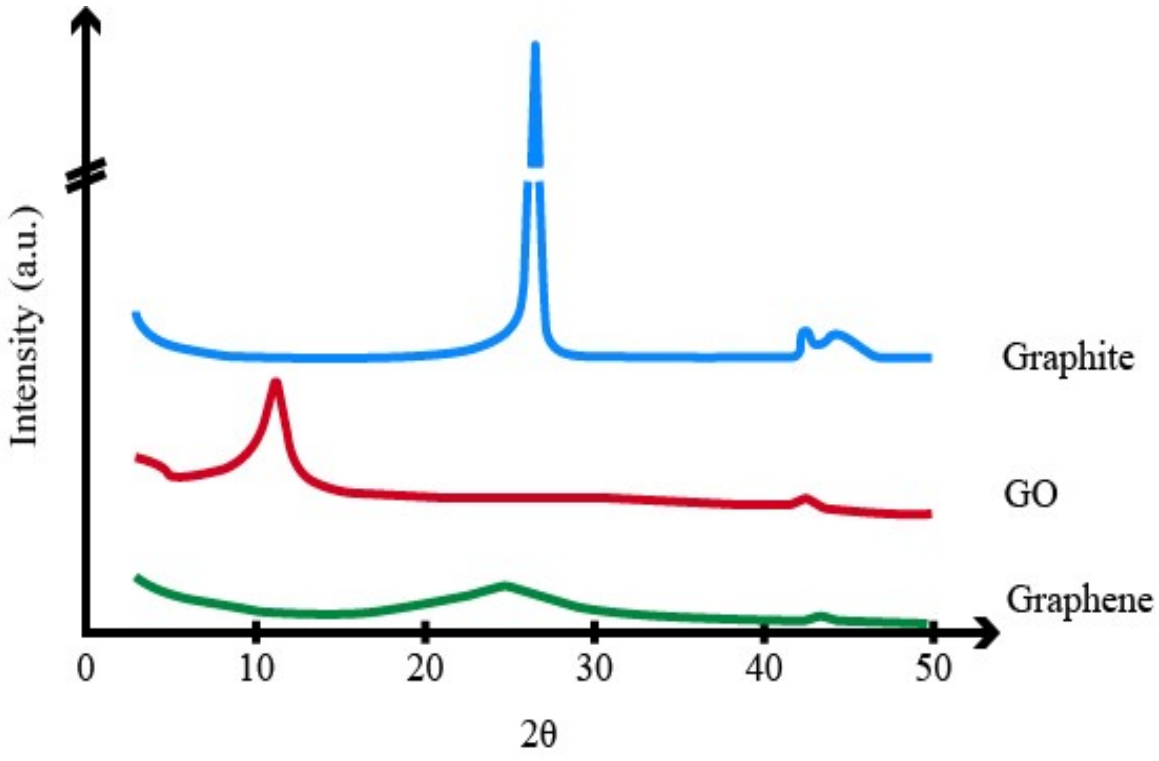

Figure 9: XRD patterns of graphite, graphene oxide and graphene (adapted from [171])

4. Experimental Setup

In this section, it will be described in detail as to how the nanocomposite samples were prepared by the two different dispersion methods, ultrasonication and three roll milling (3RM). After the samples were made, they were characterized to assess possible filler re-agglomeration, settling and alignment. Following these characterisation steps, erosional and thermal conductivity testing were performed. Related procedures are also explained in the following.

4.1. Sample Preparation

A two-part castable polyurethane, NR 606 (Normac Adhesive Products Inc., Burlington, ON, Canada) was used as the polymer matrix. It has a Shore A hardness of 70 and was the PU of choice due to its usage in high wear applications and protective coatings [172], a long working pot-life of 40 minutes, and transparency. The PU pre-polymer resin, part A, is a reaction product of polyether and toluene diisocyanate (TDI), and the hardener, part B, is di(methylthio)toluenediamine (DMTDA).

Graphene nanoplatelets (GNP) of Grade M (XG Sciences, Inc., Lansing, MI, USA) was used as the filler material [77]. GNP particles have a nominal average thickness of 7 nm and a surface area to weight ratio of 120 to 150 m^2/g, with an average diameter of 5 microns. The GNP have a manufacturer tested thermal conductivity of 3,000W/mK and 6W/mK in radial and axial direction, respectively. Their tensile modulus and tensile strength are correspondingly 1,000 GPa and 5 GPa. Both acetone and methyl ethyle ketone (MEK) were used as solvents (Fisher Scientific Company, Ottawa, ON, Canada) [[173], [174]]. As the purpose of this research is to compare the thermal conductivity and erosion wear performance of GNP-PU nanocomposites prepared by two different dispersion methods, all the steps during sample preparation were kept identical, except the step involving the dispersion. Pure PU was cured, and its properties compared to GNP-PU nanocomposite samples with 1 wt%, 2 wt%, 3 wt% and 4 wt% (weight percentage filler loading), prepared by both the ultrasonication and 3RM dispersion techniques. Thus, nine different sample sets were prepared for testing.

Firstly, GNP was weighed precisely in a beaker with an AV313 Adventurer Digital Balance (Ohaus, Parsippany, NJ, USA) [175] to the mass that is required to meet the desired weight percentage filler loading

of the sample to be prepared. The weighed GNP was then blended by magnetic stirring with 20 ml of acetone for 2 hours. Meanwhile, the monomer PU Part A was heated in an oven to 60°C. The preheated monomer was then mixed with the GNP-acetone mixture and stirred with a magnetic stirrer/heater for 30 minutes at 60°C and 100 rpm. This fabrication step was performed to evenly distribute GNP in the solution of monomer and acetone while maintaining a low viscosity. It is after this step, and before in-situ polymerisation, dispersion by either sonication and 3RM was selected. Sonication was performed for 3 hours on the mixture using a Q500 sonicator (Qsonica, Newtown, CT, USA), set to a power, amplitude, and frequency of 500 Watts, 90%, and 20 kHz, respectively [176]. For the other set of samples, solutions were subjected to 3RM three times using an Exakt 80E (Exakt Technologies, Broadway Extension, Oklahoma City, USA) [177], with a gap between the rollers of 120 μm and 5 μm and the fastest roll turning at 150 rpm. A decrease in solution level was noted during the ultrasonication process, indicating that the heat generated through the vibrating probe caused much of the acetone solvent to evaporate from the solution. Similarly, a decrease in solution mass resulted in 3RM due to acetone evaporation due to heat generated by the shearing of the material between the rollers.

After both the dispersion methods were completed, solutions were repeatedly heated to 80°C under applied vacuum at -80 kPa for 1 hour with intermittent stirring to prevent GNP from settling. Heat and vacuum were applied to evaporate and degas any remaining acetone from the solution of PU monomer phase. Subsequently, the hardener Part B was added to the monomer Part A (with dispersed GNP) according to the manufacture's recommendation, i.e., a 100/15 ratio by mass of Part A to Part B. The resulting mixture was stirred thoroughly and then poured into a mould that was preheated to the curing temperature of 90°C. Before placing the mould into the oven set at 90°C to cure for 10 hours, vacuum was once again applied to remove any trapped air bubbles that might have been entrained during the addition of the Part B hardener.

Square sample pieces, each 5 cm by 5 cm wide and 6 mm thick, were cut from the cured plates of nanocomposite material with different GNP filler loadings and made by the two different dispersion techniques. Note that after initial fabrication trials, MEK was disregarded as a solvent. MEK has a higher boiling point than acetone. Hence, removing MEK from the Part A was more difficult and required much higher temperature. MEK also lowered the viscosity of the solution significantly more than acetone. The much lower viscosity resulted in much of the GNP settling out during the curing process. It is interesting to note that this phenomenon was realized after cured nanocomposite samples curved upwards resulting in warped samples instead of flat samples. It was deduced that a high difference in coefficient of thermal

expansion throughout the cross-sectional thickness caused the warping, that is, when samples cooled down to room temperature after curing at an elevated temperature, there was a difference in contraction between the top and bottom surface. However, it should be noted that the warping effect may have also occurred due to non-uniform curing of the sample.

4.2. Material Characterisation

An EVO MA10 scanning electron microscope (Zeiss, Oberkochen, Germany) [167] was used to analyse the morphology of the nanocomposites' cross-sectional area after cryo-fracturing [178]. SEM was also employed to image neat GNP. Note that cryo-fracturing was employed to prepare samples for SEM because shear forces from cutting may destroy features in the cross-sectional surface that is of interest. Hence, liquid nitrogen was used to freeze nanocomposite samples, and the frozen brittle samples were fractured to reveal the cross-sectional surface without damaging the area of interest. Moreover, since PU is an electrical insulator, gold coating was applied to the samples to increase the surface electrical conductivity to avoid charge buildup and resulting poor SEM image quality. Similarly, SEM images of neat GNP were taken by gold coating.

WAXD (Wide Angle XRD) was performed on each samples prepared by both ultrasonication and 3RM. A Ultima IV Multipurpose X-ray diffraction system (Rigaku Corporation, Tokyo, Japan) with a cobalt tube and wavelength of 1.78899Å, applying a voltage of 38 kV and a current of 38 mA, was used for sample analysis [179]. WAXD was also performed on pure PU sample as well as neat GNP powder for comparison. In this manner, XRD spectrums of the individual nanocomposite constituents can be superimposed to better comprehend the XRD spectra of the final nanocomposites, i.e., the spectrum and/or peaks from PU, GNP and any other elements that may be present in the sample can be discerned clearly. Also, the XRD data for neat GNP can be used to determine the degree of dispersion of GNP in the nanocomposites. WAXD was performed, from 5° to 90°, on both the top and bottom surface of the samples to provide indication of particle settling. Since the XRD spectrum and peaks are dependent on the concentration and alignment of the GNP producing it, it is expected that settling of GNP particles would produce difference signatures between the two surfaces [[180], [181]].

4.3. Thermal Conductivity Testing

The thermal conductivity data of the nanocomposite samples were measured using a Thermtest Transient Plane Source (TPS) 2500S Hot Disk thermal constants analyzer (TCA) (Thermtest Inc., Fredericton, NB, Canada) with CS5501 sensors at 25°C, 60°C and 100°C [182]. The tests were performed on each type of sample, i.e., 0 wt% GNP-PU, 1 wt% GNP-PU_s, 1 wt% GNP-PU_{3RM}, 2 wt% GNP-PU_s, 2 wt% GNP-PU_{3RM}, 3 wt% GNP-PU_s, 3 wt% GNP-PU_{3RM}, 4 wt% GNP-PU_s, and 4 wt% GNP-PU_{3RM}.

To perform a thermal conductivity test, the TPS sensor was clamped in between a pair of sample pieces composed of the same nanocomposite, ensuring tight contact between sensor and sample without air gaps. The sample and sensor assembly was placed inside a thermally insulated chamber, as shown in Figure 10, where the temperature was controlled and isothermal tests were performed. The temperature control involved circulating heated silicone oil through the chamber walls from a reservoir unit using circulation bath and pump. The bulk (isotropic) thermal conductivity was measured for the various sample types. The average thermal conductivity was calculated from 20 sets of thermal probing at 50 mW that lasted for probing periods of 5 seconds, 10 seconds and 20 seconds. Thermal conductivity results from different probing periods were used to check for sample homogeneity. After each test, the results were checked for the probing depth to ensure that probing did not surpass the actual sample thickness, in which case the tests were repeated for a lower probing period. Prior to taking measurements at a specific temperature, a wait time of 3 hours was applied to let the samples subsequently reach equilibrium measurement temperatures of 25°C, 60°C and 100°C. There also was a wait period of 15 minutes between each thermal probing to let the sample cool down to the target temperatures of 25°C, 60°C and 100°C.

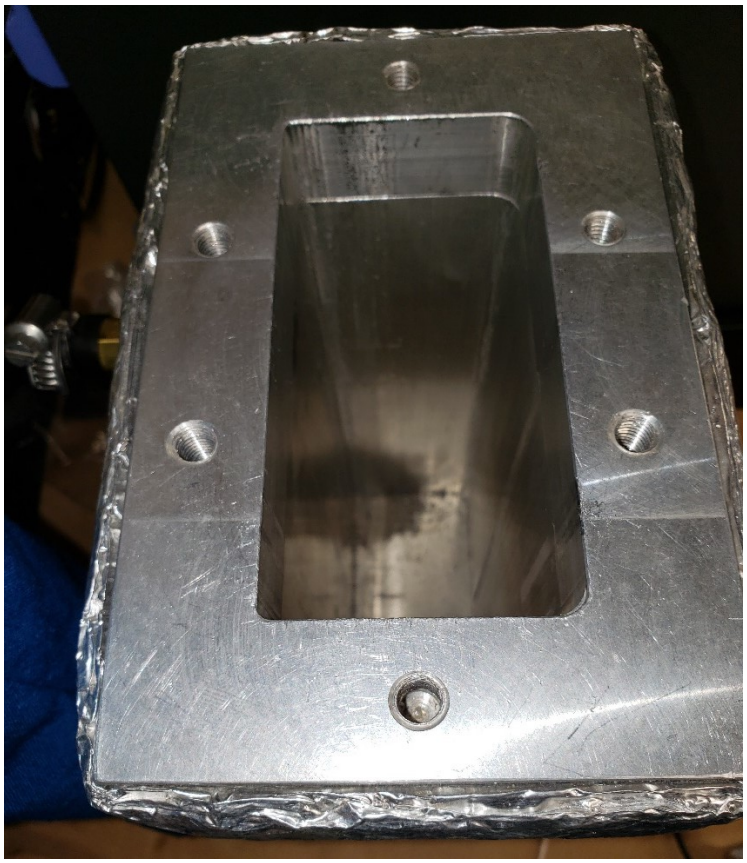

Figure 10: Insulated chamber for thermal conductivity testing

Specific heat capacities were measured for 0 wt% GNP-PU, 3 wt% GNP-PU_s, 3 wt% GNP-PU_{3RM}, by using a differential scanning calorimeter (DSC) following the ASTM E1269 standard. For the DSC, experiments a Mettler Toledo DSC 2 Instrument with 40 µL Mettler Toledo standard aluminum crucibles (Mettler-Toledo, LLC, Columbus, OH, US) was utilised [183]. Specific heat capacities obtained by DSC were used as an input parameter required to assess anisotropic thermal conductivity via the TPS method. Anisotropic thermal conductivities, at different probing depths, were measured for 0 wt% GNP-PU, 3 wt% GNP-PU_s and 3 wt% GNP-PU_{3RM} to assess possible filler alignment and settling between the different dispersion methods.

4.4. Erosion Testing

The erosion rate of pure PU and GNP-PU nanocomposites with different GNP filler loading and dispersion methods was measured by using a modified ASTM G76 erosion testing apparatus. This modified apparatus, as shown in Figure 11 and Figure 12, allows for changing the temperature of a stream of gas and solid particles flowing through a nozzle. The experimental setup is also capable of adjusting the angle of the sample with respect to the nozzle. For the purpose of this research, the erosion rate was measured at temperatures of 25°C, 60°C and 100°C while the samples were set at a 30° impingement angle. The erosion test assembly was set to this angle since ductile materials are most prone to erosion at this angle.

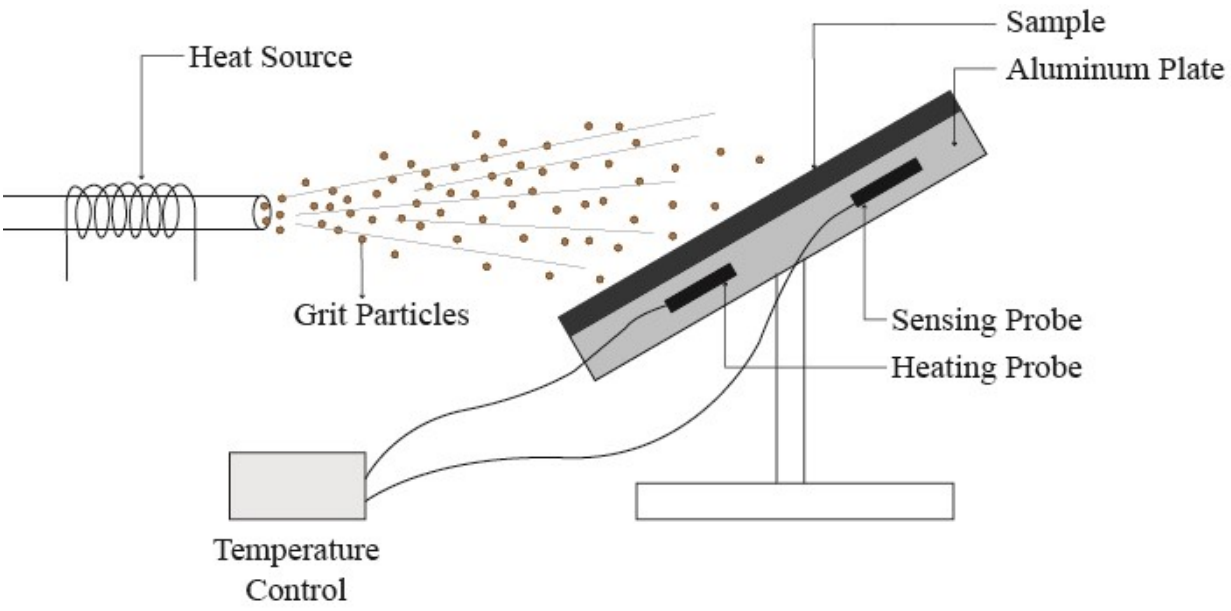

Figure 11: Schematic of modified ASTM G76 erosion testing setup (adapted from [6])

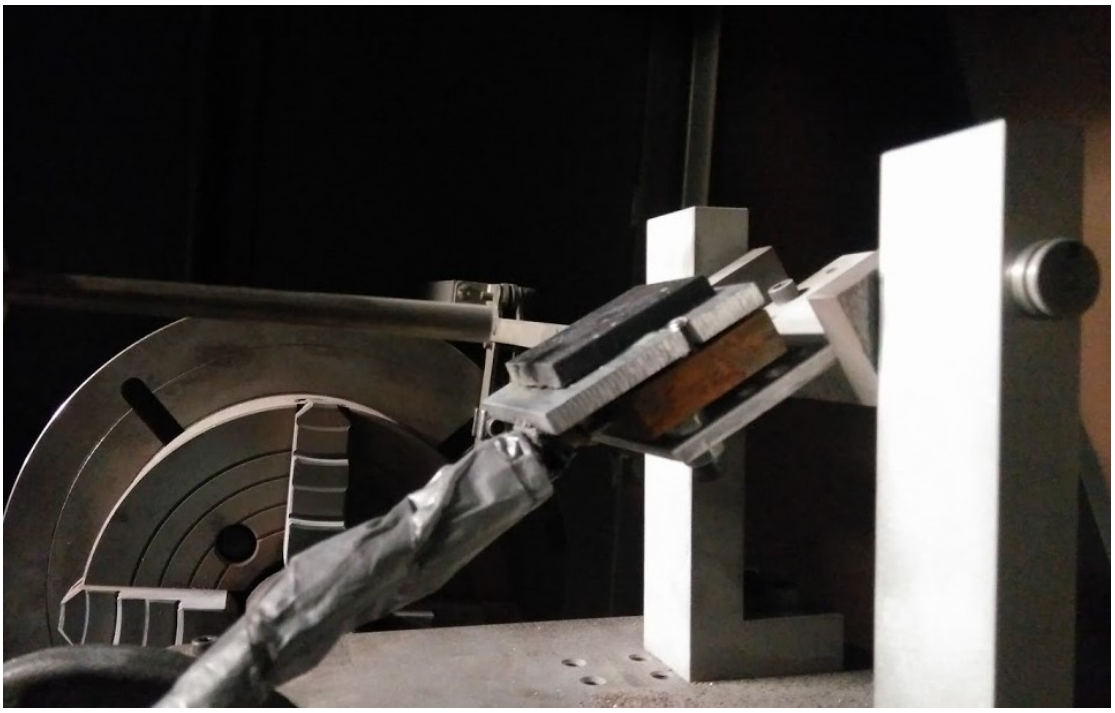

Figure 12: Modified ASTM G76 erosion testing setup

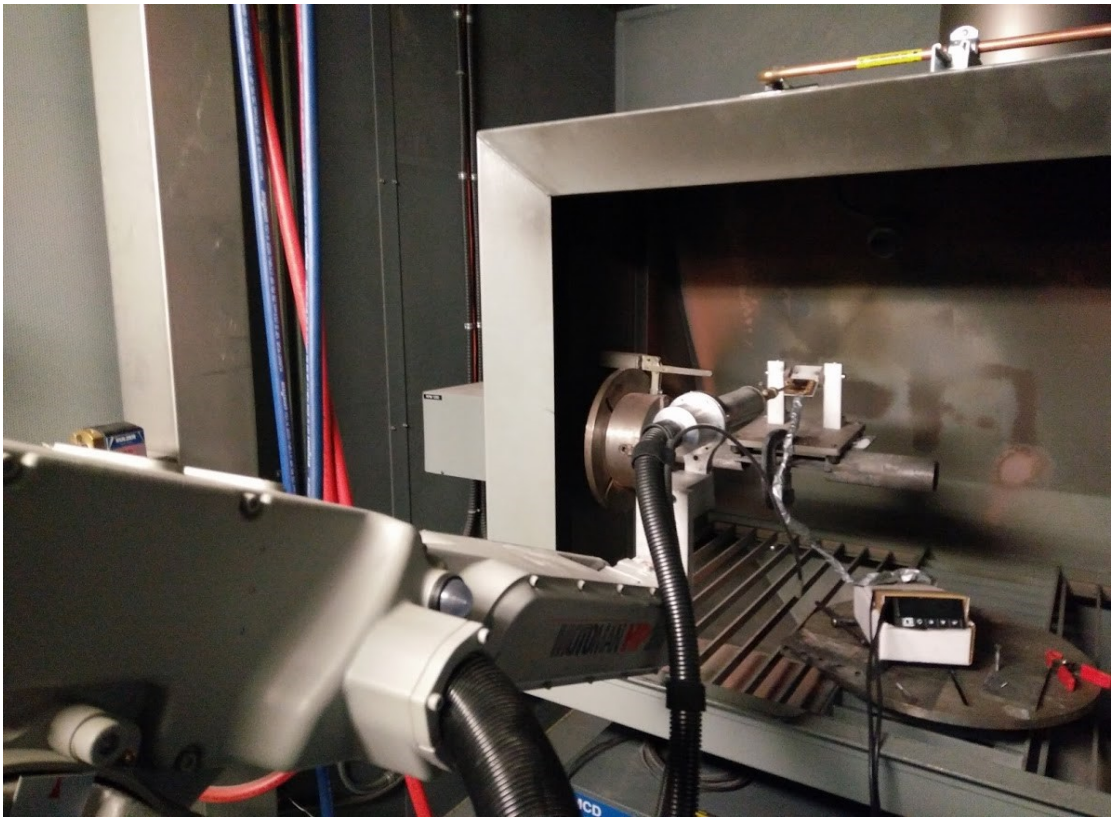

Figure 13: Motoman HP20 robot arm being used to hold nozzle in position

A programmable extended-reach robotic handling arm, Motoman HP20 (HP-20, Motoman, Yaskawa Electric Corp., Waukegan, IL, USA) [184], as shown in Figure 13, was used to bring the nozzle in place and hold its position to spray the eroding grit particles. A total of 27 different samples were bonded to aluminum substrates using 3M epoxy adhesive (3M DP460, 3M Scotch-Weld, St. Paul, MN, USA) [185]. Experiments were divided into three groups of nine samples, i.e., one group for each of the three different temperatures of 25°C, 60°C and 100°C. The nine samples in each group were 0 wt% GNP-PU, 1 wt% GNP-PU_s, 1 wt% GNP-PU_{3RM}, 2 wt% GNP-PU_s, 2 wt% GNP-PU_{3RM}, 3 wt% GNP-PU_s, 3 wt% GNP-PU_{3RM}, 4 wt% GNP-PU_s and 4 wt% GNP-PU_{3RM}. The mass of each of the samples with the aluminum substrate was measured precisely using the AV313 Adventurer Digital Balance [175]. Then, samples were preheated to the desired test temperature before running an erosion test. Grit particles of size #54, which is 300 μm on average, were weighed each time along with a hopper. The hopper was attached to the volumetric powder feeder 5MPE (Oerlikon Metco, Westbury, NY, USA), which is the control unit for temperature and pressure of the gas stream. Erosion tests were performed with the solid particles impinging each of the sample for 200 seconds, at a pressure of 435 KPa (63.1 psi), and temperatures of 25°C, 75°C and 125°C on samples preheated to 22°C, 60°C and 100°C, respectively. After each erosion test, each sample was thoroughly cleaned to remove any solid particles and then weighed again precisely. The mass of the solid grit particles remaining in the hopper was also determined. The final erosion rate was thus measured as the difference in the mass loss of the test sample divided by the difference in the mass of the eroding solid particles.

5. Results and Discussion

5.1. SEM Imaging of Neat GNP and GNP-PU Nanocomposites

SEM imaging of neat GNP, as shown in Figure 14, reveals that particles are of different sizes varying from around 1 μm to 30 μm. The thickness of the platelets also varies between each of the particles, and particles are randomly shaped and deviate strongly from circular shape. SEM images of cryo-fractured cross sectional surfaces, as shown in Figure 15 and Figure 16, reveals that the GNP filler was well distributed within the PU matrix, with noticeable few agglomerates. There are also no visible signs of damage to the platelets under freeze fracturing. Figure 15 shows a cavity in the top right of the image which was likely created by a platelet being separated perpendicularly from the sample surface during the cryo-fracturing. Figure 16 shows that it is possible for platelets to self-align when in close proximity to one another. Although this does not represent the bulk of the samples, it does provide valuable insight into how particles are arranged inside the matrix.

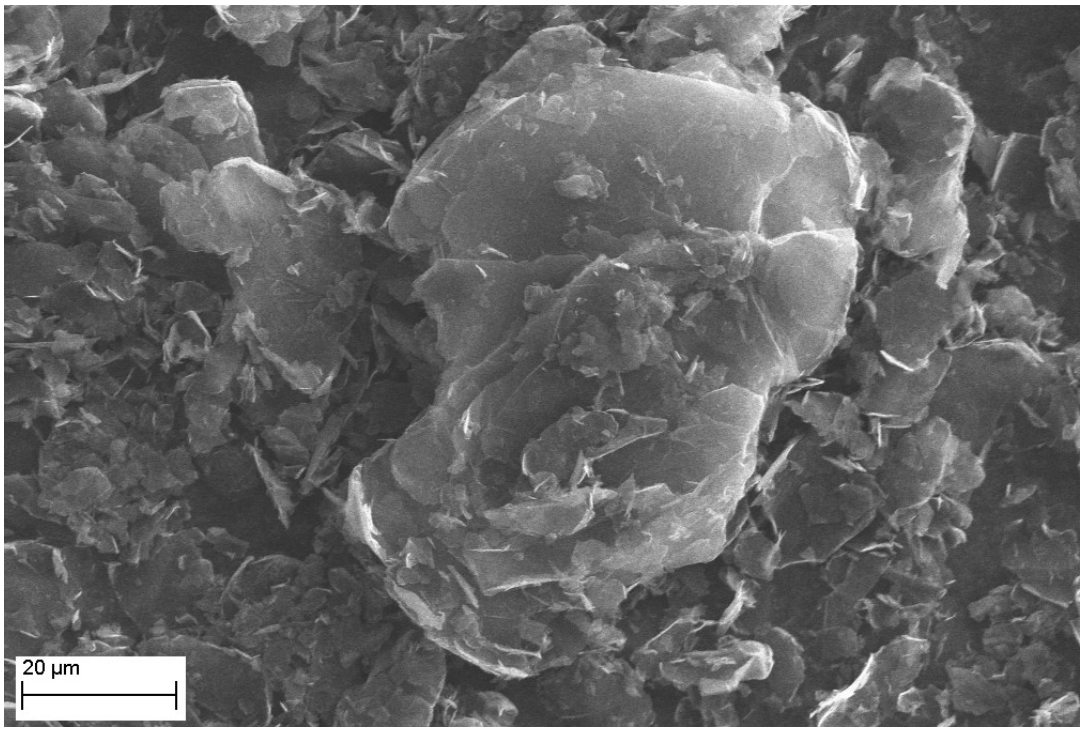

Figure 14: SEM image of neat GNP under 802X magnification

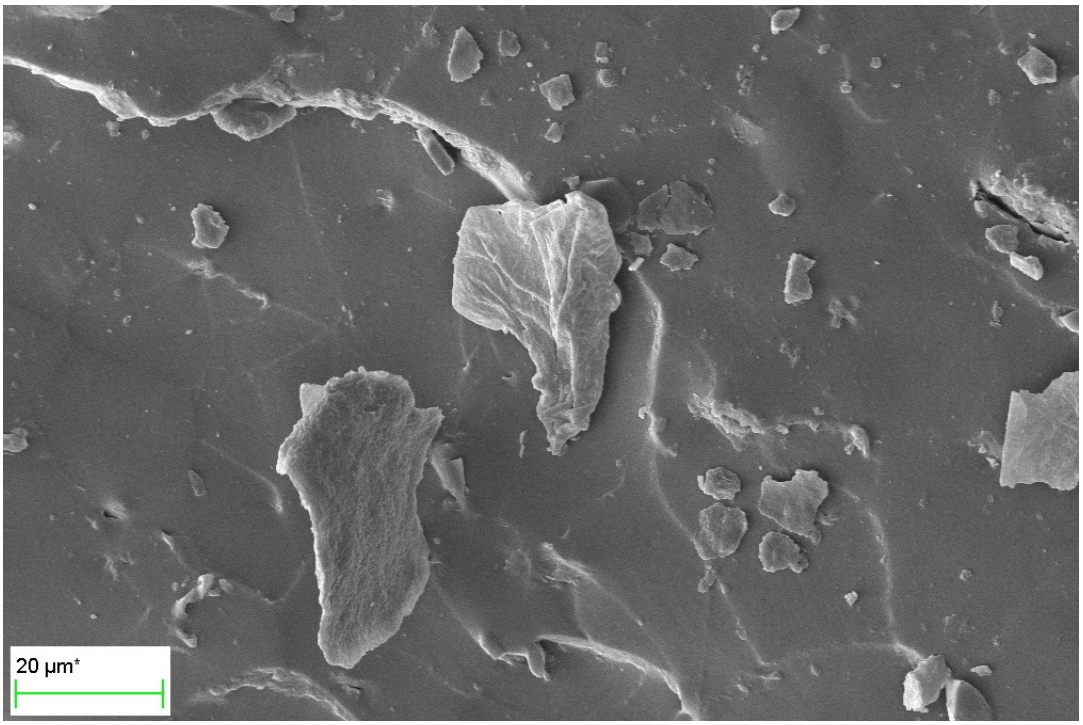

Figure 15: SEM image of freeze fractured cross sectional surface showing GNP embedded in PU in 1 wt% GNP-PU nanocomposite material at 772X magnification

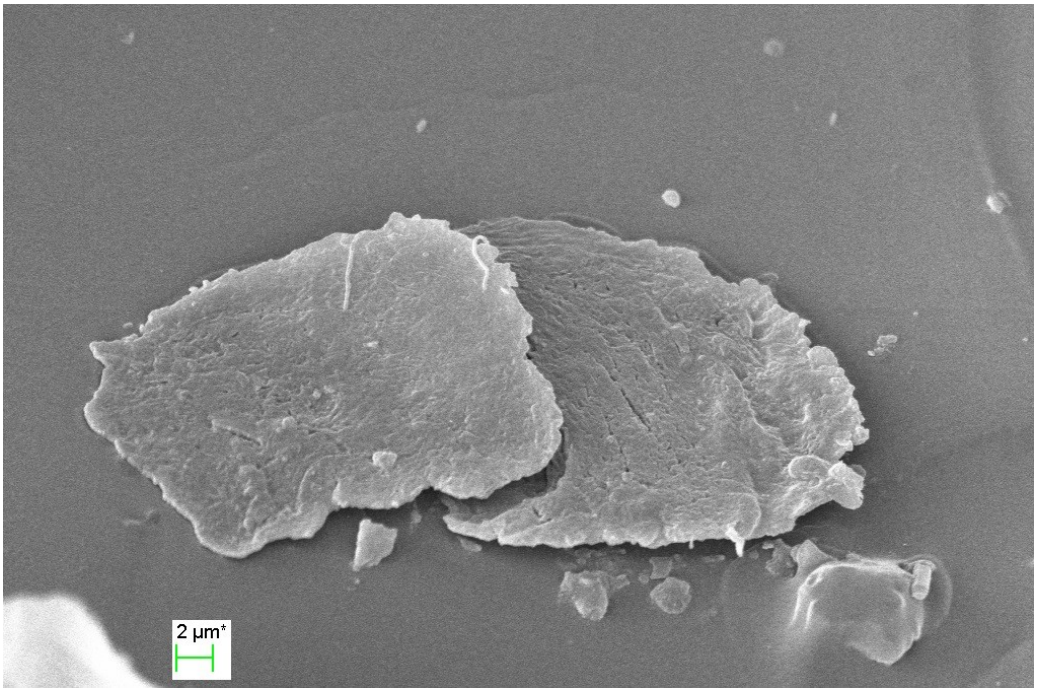

Figure 16: SEM image of freeze fractured cross sectional surface showing GNP embedded in PU in 1 wt% GNP-PU nanocomposite material at 2000X magnification

5.2. XRD Analysis

The XRD results were plotted for pure PU and neat (un-exfoliated) GNP in the same graph to help distinguish the peaks from XRD analyses of nanocomposites. The graph, shown in Figure 17, reveals that pure polyurethane has one major broad peak at an angle of around 23.5°. Neat GNP exhibits a distinct peak with high intensity at an angle of 31°. Clearly, the PU peak is much broader and less intense than the peak of GNP, which is to be expected given that PU is amorphous whereas GNP features a lattice structure. Using Eq.6 from Section 3.8.2, the angle at which the diffraction occurs and the wavelength of the incoming X-ray, d-spacing between platelets of 3.35 angstroms is determined. In previous research the d-spacing for graphite was ascertained as 3.36 angstroms [171], which closely matches the present results. Minor peaks in the XRD spectrum of GNP are assumed to be due to impurities, such as bonded oxygen or residual acid content as mentioned in the manufacturer's data sheet [77]. From the XRD spectrum, it can be deduced that GNP as used in this research are not mono layers, but rather stacked platelets, as also indicated by SEM images in the previous section. The data sheet from the manufacturer specifies the thickness of platelets to be 6 nm to 8 nm, which also confirms that multiple sheets are stacked as it is known that a single graphene sheet is about 0.3 nm.

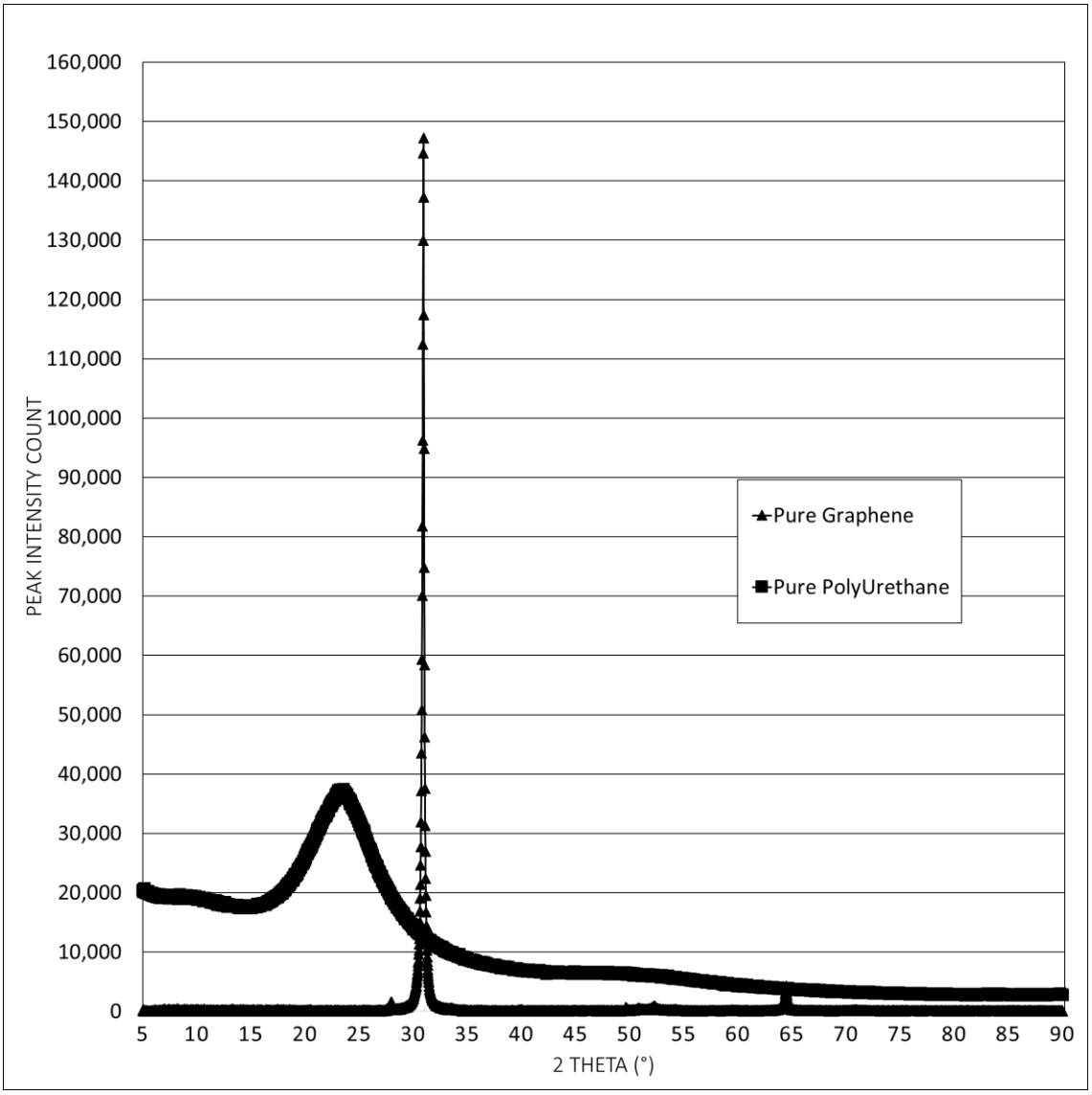

Figure 17: XRD Analysis graph of pure PU and un-exfoliated GNP

It is expected that the XRD spectrums of GNP-PU nanocomposites will have strong similarity to the superimposed XRD curves of pure PU and GNP as shown in Figure 17, assuming that the filler particles in the nanocomposites are not exfoliated. XRD plots for the top and bottom surface of GNP-PU nanocomposites prepared by the different dispersion methods are presented in the Appendix Figure A1 to Figure A4. The analytics from the XRD scattering results of the different samples are presented in Table 1.

Table 1: XRD analysis of top and bottom surface of GNP-PU nanocomposites

	Sonicated				3RM			
	1%	2%	3%	4%	1%	2%	3%	4%
Top Surface Highest Intensity Count	26,621	41,429	48,055	64,187	20,366	13,140	53,481	45,392
Bottom Surface Highest Intensity Count	25,798	39,701	46,240	50,641	23,613	26,489	59,051	54,023
Top Surface Diffraction Angle 2Θ for Peak Intensity	30.92	30.92	30.98	30.92	30.94	30.84	30.94	30.92
Bottom Surface Diffraction Angle 2Θ for Peak Intensity	30.96	30.94	30.96	30.94	30.92	30.88	30.92	30.92
Combined Peak Intensity Count	52,419	81,130	94,295	114,828	43,979	39,629	112,532	99,415
Normalized Combined Peak Intensity Count (per wt % GNP)	52,419	40,565	31,432	28,707	43,979	19,815	37,511	24,854

From XRD graphs of GNP-PU nanocomposites shown in Figure A1 to Figure A4, and correlating the findings for pure PU and GNP, the broad peak at 23.5° angle is associated with polyurethane while the sharp peak at 31° arises from the presence of graphite. Since the peak intensity is dependent on the concentration of the element that is giving rise to the peak at that diffraction angle, it is supposed that the greater the magnitude of the graphite peak, the greater concentration of un-exfoliated GNP is in the material [186]. The peak intensity count of GNP for both the top and bottom surfaces of each sample were compiled to provide a representation of the degree of dispersion of the GNP in the samples. Peak intensities were further also normalised by dividing values by the GNP filler weight percentage of the nanocomposite.

Figure 18 depicts the normalised total XRD peak intensities for the nanocomposite samples of varying filler loading prepared by the two different dispersion methods. It indicates that for the sonication method, higher degree of GNP dispersion was attained with increase in filler loading. The degree of dispersion increased as judged by a decrease in the total peak count with increase in filler loading. On the other hand, by 3RM, trends are less clear, yet it appears that the degree of dispersion is higher than for sonication at lower filler loadings. Nevertheless, unlike for the sonication method, no clear evidence exists to conclude that exfoliation quality improved with increase in filler loading for the 3RM method.

Data in Table 1, indicates that at lower filler loading the diffraction angle at which XRD peaks occur are slightly lower than 31°, which is more prominent for the 3RM method, suggesting an increase in d-spacing. The increase in d-spacing between the crystal lattice, can be due to intercalation of polymer chains between layers of GNP [170]. The increase in d-spacing is less noticeable at higher filler loadings. Judging from the differences between the top and bottom surface XRD peak counts, there is no indication of settling in the sonication dispersion method. XRD peak counts are much larger in the bottom surface of the samples prepared by 3RM process which suggests that there may be settling of agglomerated filler platelets in the nanocomposite samples prepared by 3RM.

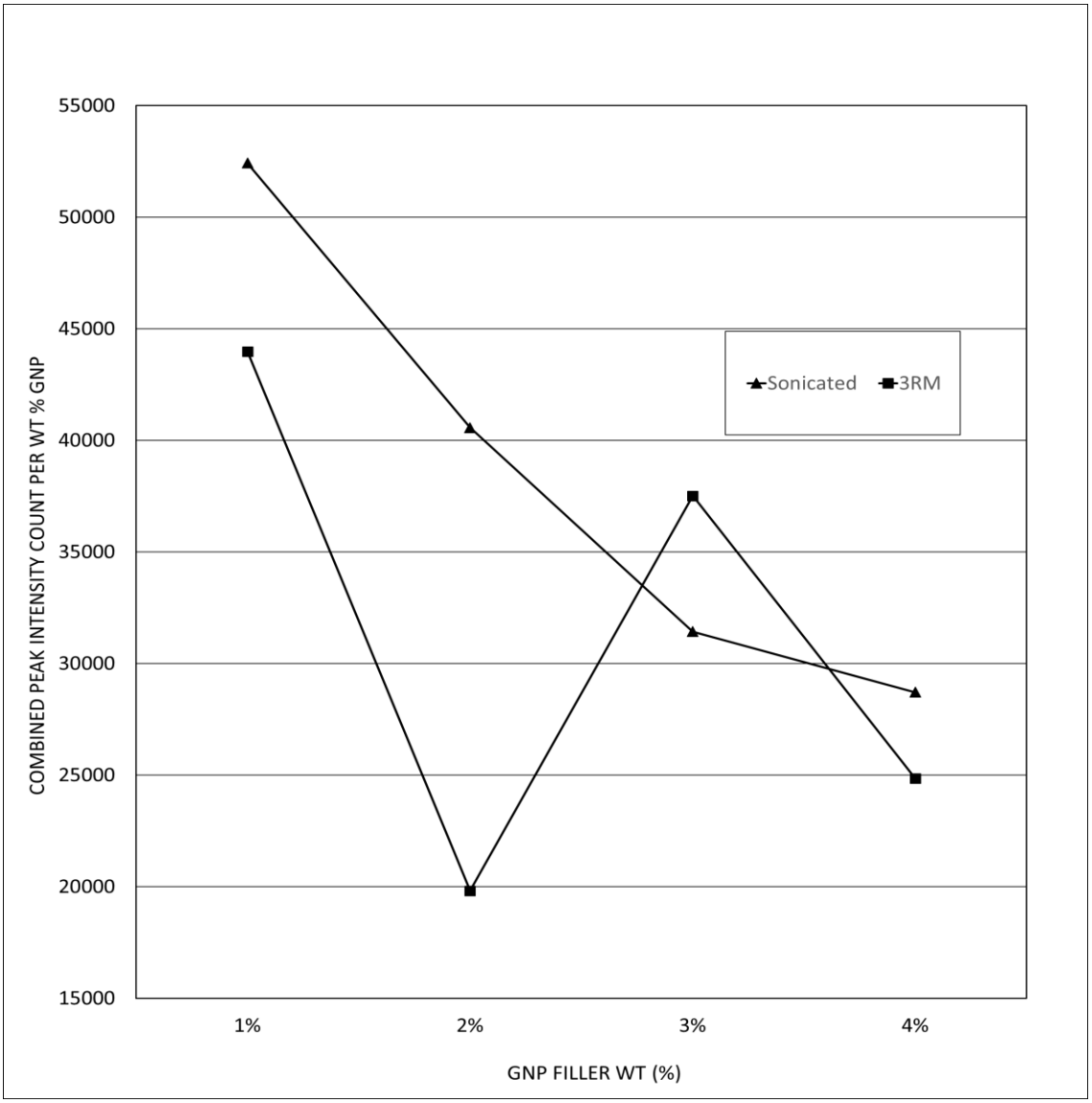

Figure 18: Normalised XRD peak intensity count against varying GNP concentration

5.3. Differential Scanning Calorimetry

DSC measurements taken for pure PU over a range of -10°C to 150°C over three repeated cycles, as shown in Figure A5 in the Appendix, revealed that the glass transition temperature is -8°C. Thus, over the temperature range of the erosion test, the polyurethane was in its rubbery phase. Besides pure PU, nanocomposites with 3 wt% GNP dispersed by sonication and 3RM were characterized via DSC. Resulting data revealed that specific heat capacity and volumetric heat capacity increased with temperature for all three materials. However, for the 3 wt% GNP-PU_{3RM} sample, the specific and volumetric heat capacity is lower over the whole temperature range compared to pure PU and 3 wt% GNP-PU_S, as presented in Figure 19 and Figure 20.

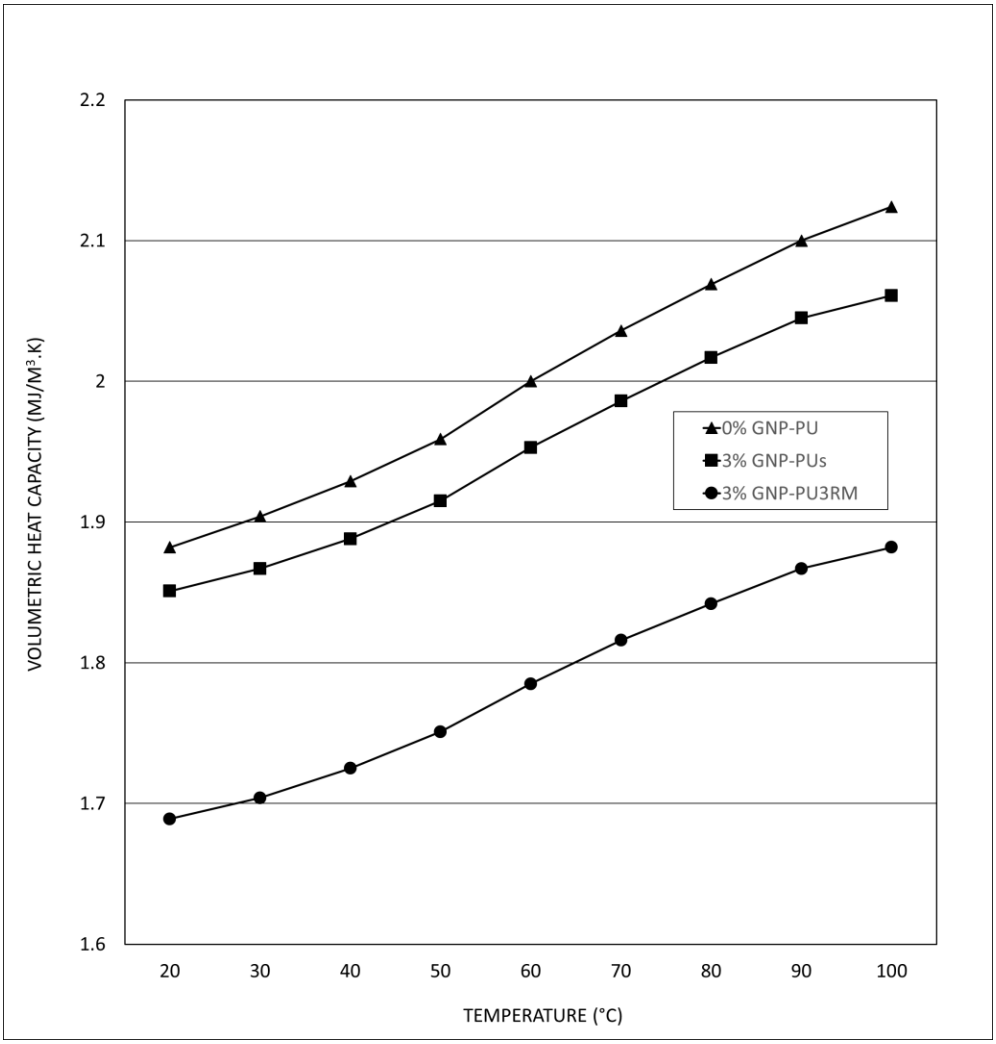

Figure 19: Volumetric heat capacity of pure PU and 3 wt% GNP-PU nanocomposite samples

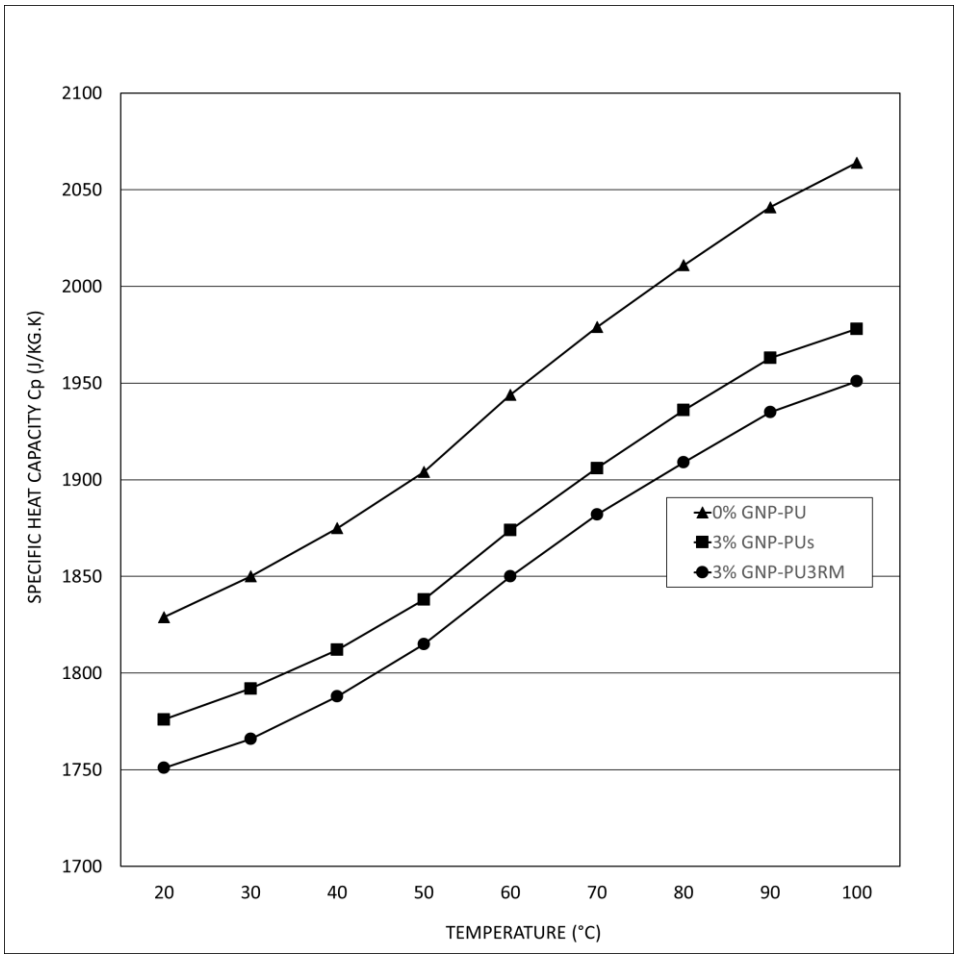

Figure 20: Specific heat capacity of pure PU and 3 wt% GNP-PU nanocomposite samples

5.4. Isotropic Thermal Conductivity Measurements

The bulk thermal conductivity of pure PU was measured first to verify calibration of the TPS device. At room temperature the bulk isotropic thermal conductivity of pure PU was found to be 0.19 W/mK. Previous experiments performed by Akram reported a bulk thermal conductivity of 0.2 W/mK at room temperature [7]. Other research available in the technical literature reported the thermal conductivity of non-porous PU to be 0.19 W/mK [187]. For the nanocomposite samples, data from thermal conductivity testing of at temperatures of 22°C, 60°C and 100°C are depicted in Figure 21 to Figure 23, respectively.

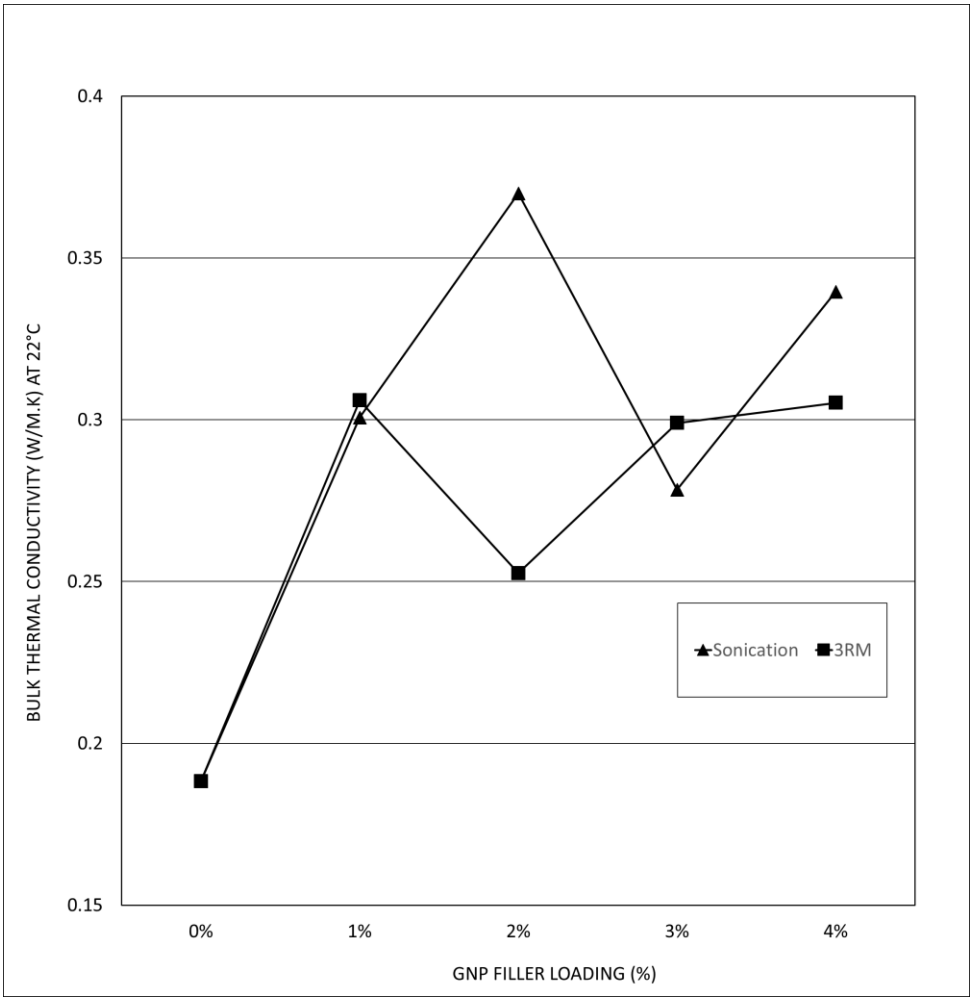

Figure 21: Bulk isotropic thermal conductivity at 22°C of pure PU and GNP-PU nanocomposites

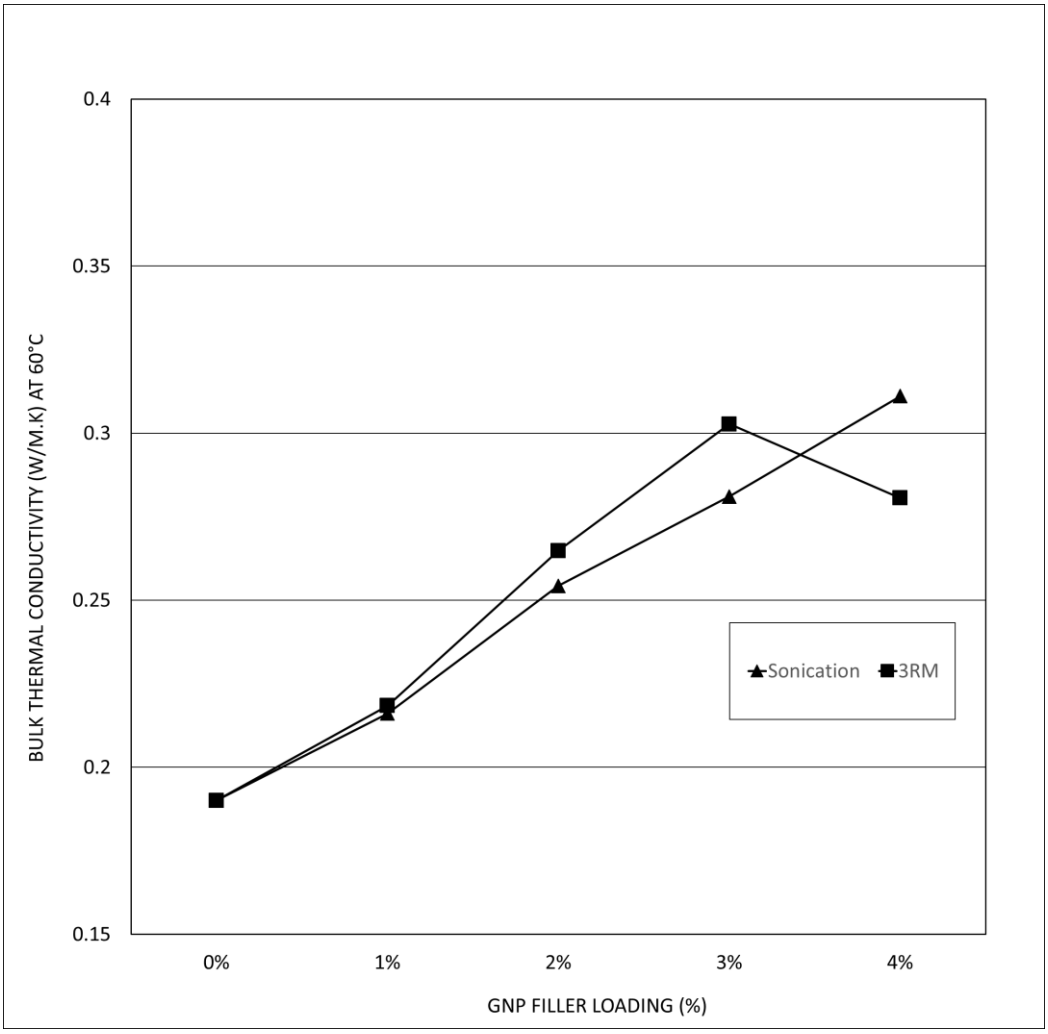

Figure 22: Bulk isotropic thermal conductivity at 60°C of pure PU and GNP-PU nanocomposites

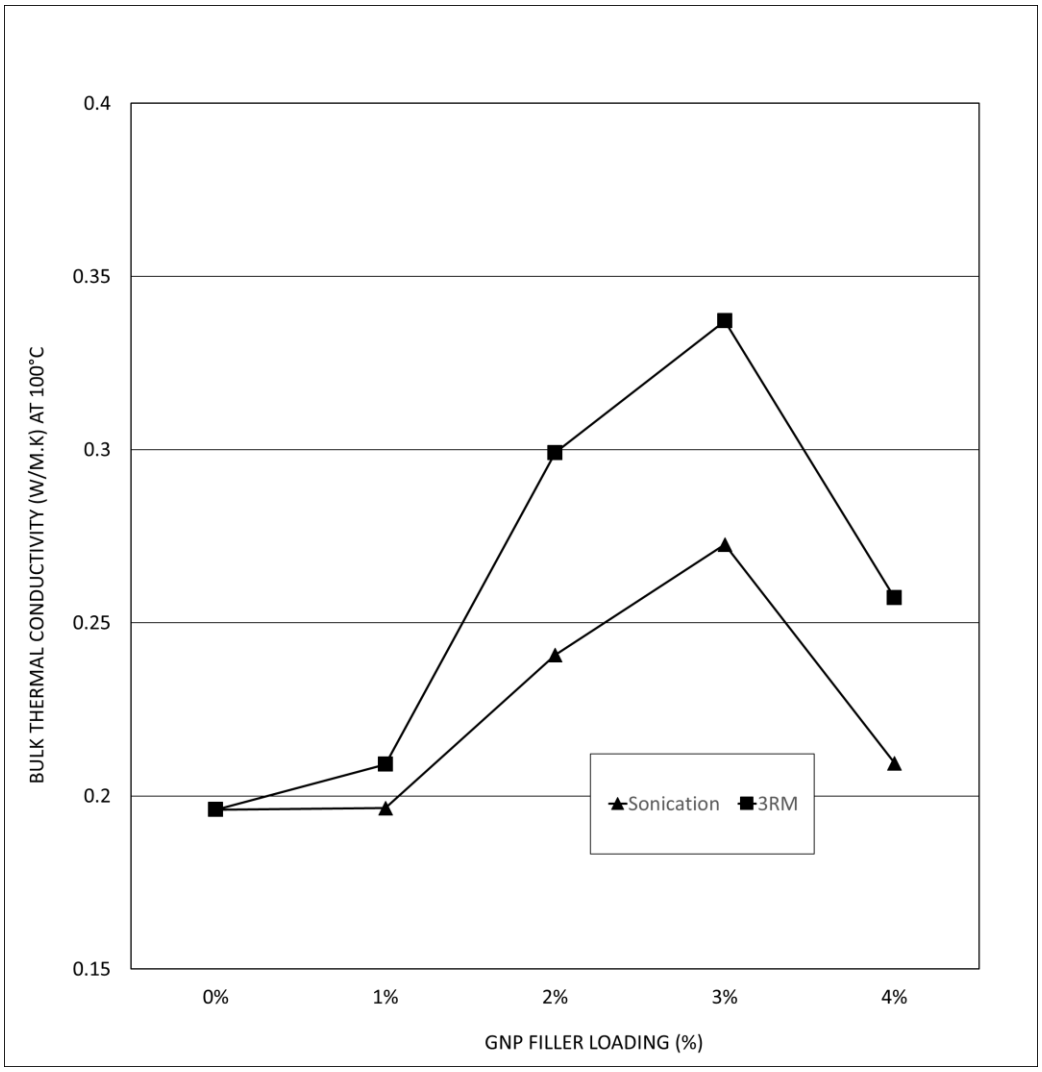

Figure 23: Bulk isotropic thermal conductivity at 100°C of pure PU and GNP-PU nanocomposites

In Figure 21 to Figure 23, it can be observed that thermal conductivity increased with increasing filler loading. Especially at elevated temperatures, thermal conductivity of GNP-PU nanocomposites prepared by 3RM is higher compared to those samples prepared by the sonication method. This trend is not as much apparent at the lower test temperatures. Thermal conductivity of nanocomposites with 3 wt% filler loading prepared by the sonication method increased by 47.8%, 47.8% and 39.1% at 22°C, 60°C and 100°C, respectively, as compared to pure PU. In contrast, for the same filler loading, nanocomposites made by 3RM, the thermal conductivity increased correspondingly by 58.8%, 59.2% and 72.0%. Higher thermal conductivity of nanocomposites prepared via 3RM may be attributed to filler alignment and/or a higher degree of filler dispersion, as concluded by XRD analysis. Due to higher filler alignment, graphene platelets are in closer proximity to each other, reducing phonon scattering. Filler alignment may further promote

phonon transfer by decreasing the mean free path between particles. In this manner, quasi-percolating behavior yielding directional conductive networks may been have developed in samples produced via 3RM [[46], [49], [57], [62], [187]]. At all three temperatures, for both types of dispersion method, it can be observed that between 2 wt% and 3 wt% filler loading, the rate of thermal conductivity increase with filler loading is declining. As mentioned earlier, assuming percolation type behavior, a threshold in filler loading for rapid increasing thermal conductivity exists beyond which a rise in conductivity occurs at a lower rate. In a previous paper it was noted that the percolation threshold GNP filler percentage for electrical conductivity was 0.3 wt% [104], which is lower than what was tested by the present experiments. However, mechanisms for the transport of electrical charge and phonons are different, so a correlation cannot necessarily be expected. Research on thermal conductivity of GNP-PU dispersed by 3RM indicated a thermal percolation threshold of 1 wt% filler loading [188]. Other research has found the thermal percolation threshold of GNP dispersed in polymer to be as low as 0.17 wt % [109].

In some instances, especially in Figure 21Figure 23, a sharp decrease in thermal conductivity is observed at higher filler loading, specifically, beyond 3 wt% GNP. Although XRD analysis indicated that the ratio of normalized exfoliated GNP increased with the increase in filler loading, a greater amount of agglomerated GNP may be present in samples with high filler loading which degraded the quasi-percolating directional conductive networks, leading to the sharp decrease in thermal conductivity. In other words, the positive effect on thermal conductivity enhancement resulting from better exfoliation was annulled by a more negative effect on thermal conductivity due to agglomeration. It should be noted that high filler loadings make handling and processing of nanocomposites more difficult due to rapidly increasing viscosity, thus filler dispersion is more challenging and air is more easily entrapped inside the sample, which may contributed to the drop in thermal conductivity at the high filler loadings.

As seen in Figure 20, due to an increase in specific heat capacity with temperature, and following Eq.(2), it is expected that thermal conductivity will increase with temperature for all samples. However, as seen in Figure 24 and Figure 25, for both the 3RM and sonication methods, thermal conductivity does not increase significantly with temperature. It is noted that for some of the samples, there is even a slight decrease in thermal conductivity with temperature. At room temperature, the thermal conductivity of the GNP nanocomposites was significantly higher than for pure polyurethane, so this strong initial effect seems to be merely maintained at elevated temperatures. Since it was ascertained that specific heat capacity increased with temperature for the samples, any decrease in thermal conductivity at higher temperatures can be

speculated to be due to a decrease in either phonon velocity, *v,* or the mean free path, *l*. This has been described in literature stating that for solid crystalline materials, thermal conductivity is proportional to the mean free path, *l,* which is proportional to $1/T^x$, where T is temperature greater than 20°K and x is a value between 1 and 2 [189]. Notably, the GNP-PU_{3RM} samples with 2 wt% and 3 wt% exhibited an increase in thermal conductivity with temperature. These are the same samples that showed an anomaly in trend in XRD curves compared to the other samples.

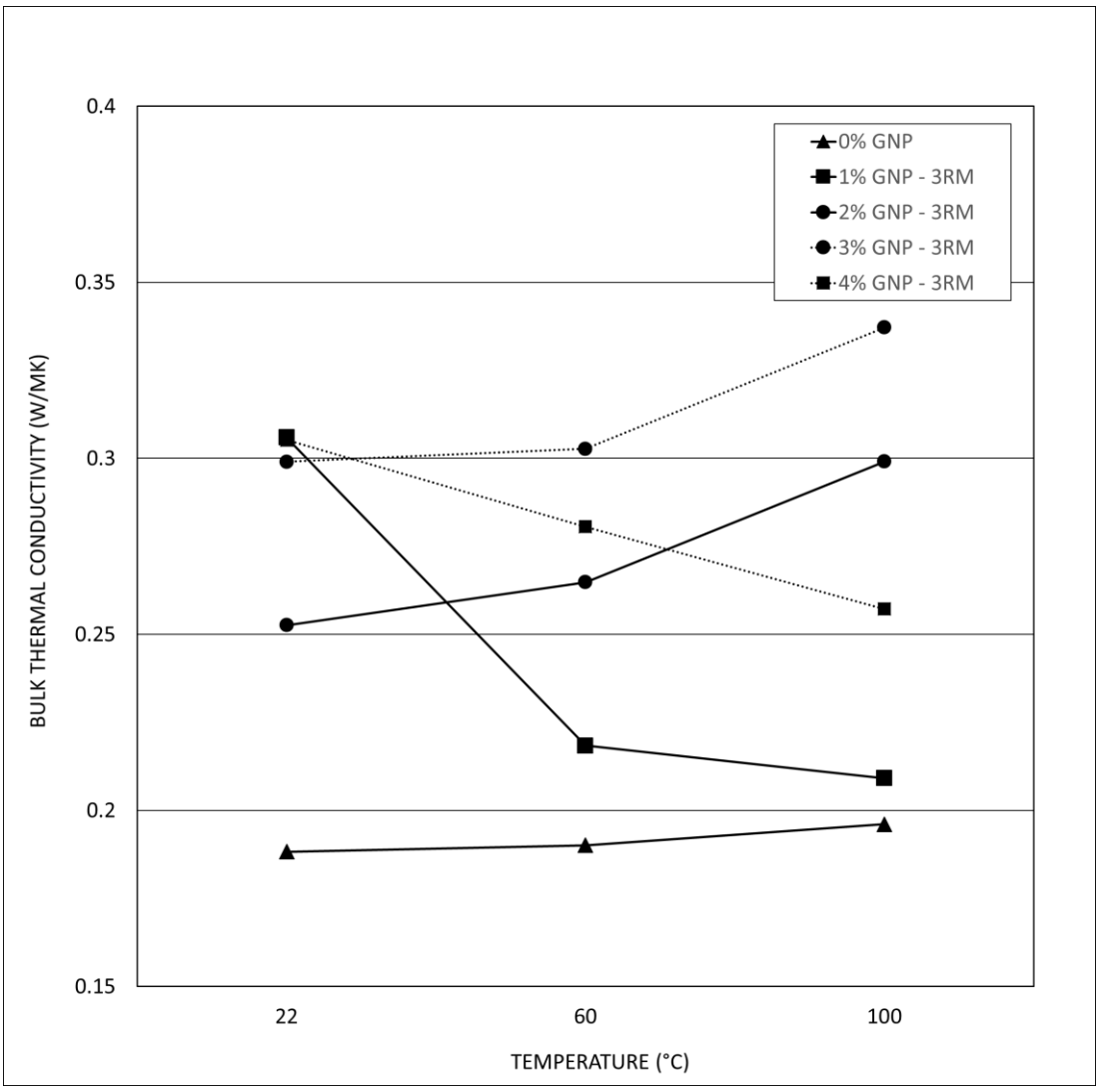

Figure 24: Bulk isotropic thermal conductivity of 3RM GNP-PU nanocomposite samples

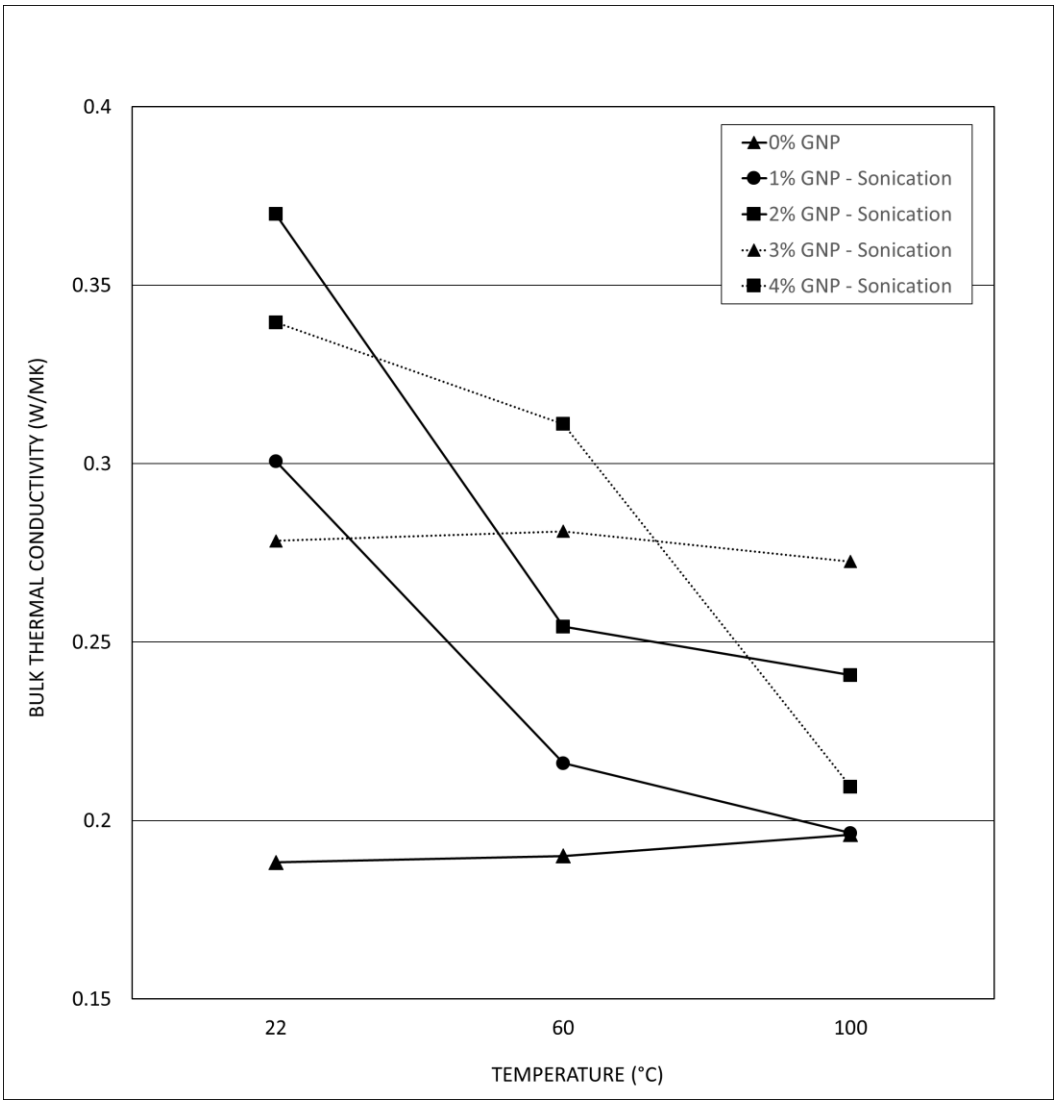

Figure 25: Bulk isotropic thermal conductivity of sonicated GNP-PU nanocomposite samples

The thermal conductivity of samples was analysed at full and half probing depth in order to assess the quality of filler distribution throughout the matrix. For a homogenous distribution, it is expected that thermal conductivity will be the same at both full and half probing depth. As per Figure 26, for the 1 wt% filler loading, the full probing depth thermal conductivity was slightly lower than the half probing depth thermal conductivity for both the sonicated and three roll milled samples. This suggests that there was some degree of settling of GNP which resulted in higher thermal conductivity in the half probing depth. However, for the 2 wt% filler loading, unlike its sonicated counterpart, the three-roll milled sample does not show any sign of settling. The most homogenous distribution can be observed for samples with 3 wt% filler loading where both the sonicated and 3RM samples exhibited thermal conductivities of similar magnitude

for both full and half probing depth. The sonication method also provided more homogeneous thermal conductivity for the 4 wt% GNP nanocomposites compared to the 3RM counterparts. Thus, the thermal conductivity results are in line with the XRD analysis from which it was deduced that sonication method had yielded more homogenously distributed GNP in the PU matrix.

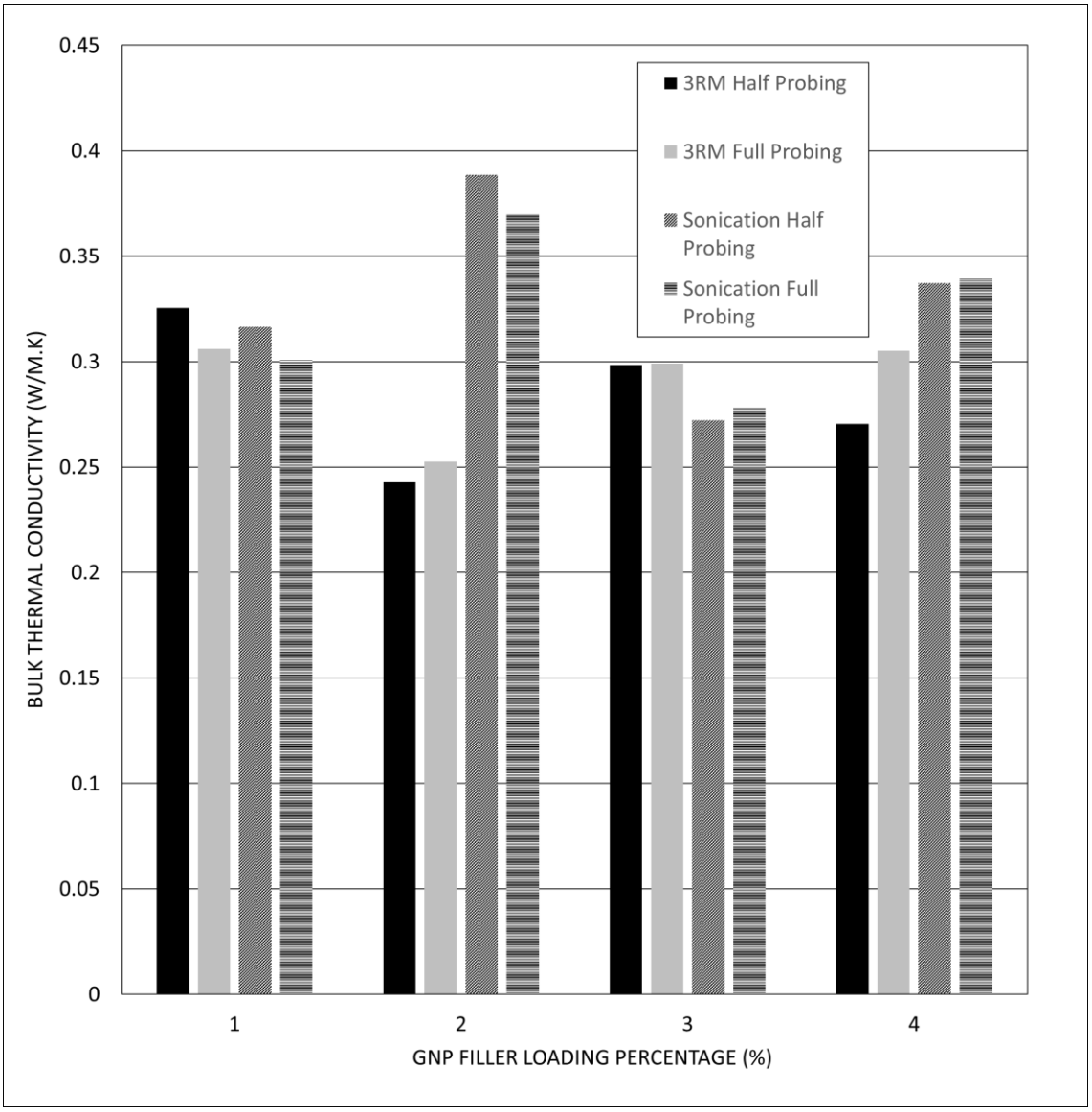

Figure 26: Bulk isotropic thermal conductivity of GNP-PU nanocomposite samples at full and half probing depth

5.5. Anisotropic Thermal Conductivity Measurements

The anisotropic thermal conductivity measurements gave insight into the effect of alignment on the thermal conductivity of nanocomposites in the in-plane (radial) and through-thickness (axial) direction. As expected, it can be seen from Figure 27 that for pure polyurethane the axial and radial thermal conductivity are practically identical, indicating that the sample is isotropic. For nanocomposites with 3 wt% filler loading prepared by sonication, thermal conductivity is higher in the axial direction compared to the radial direction, which suggests that there is some degree of anisotropy due to the presence of GNP. If GNP were randomly oriented, testing would have showed that the sample is isotropic. The result also suggests that vertical platelet alignment occurred. Anisotropic thermal conductivity may stem from a self-alignment effect of filler platelets while setting due to gravity. The 3 wt% GNP-PU_{3RM} nanocomposite exhibited even higher thermal conductivity in the axial direction compared to the radial direction, which suggests an even higher degree of alignment of platelets in the matrix. These observation correspond with findings in literature discussed in Section 3.5.1.3, where it was stated that a higher degree of filler alignment can be attained by 3RM due to the shear forces applied by the rollers.

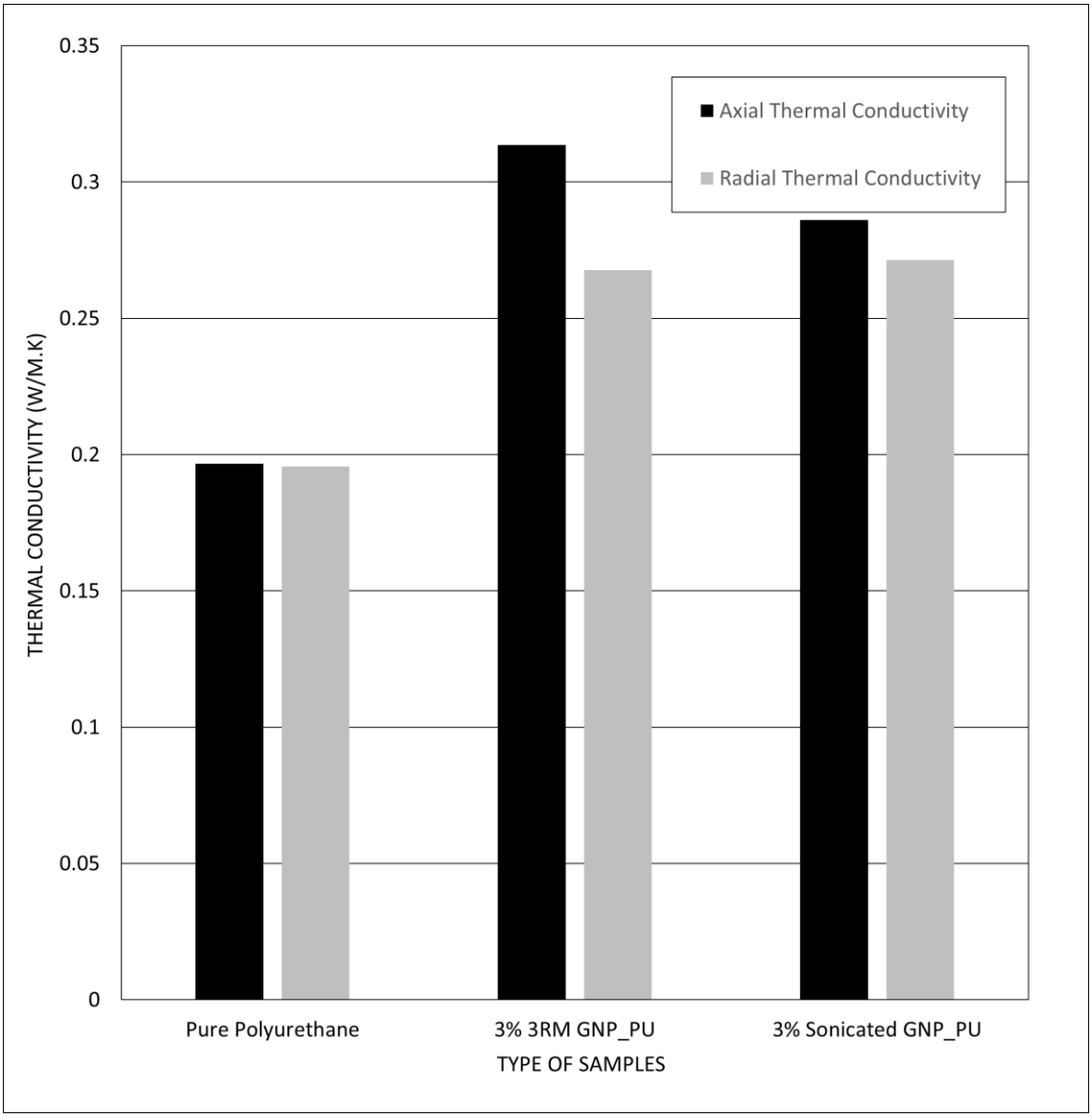

Figure 27: Anisotropic thermal conductivity of pure PU and 3 wt% GNP-PU nanocomposite samples

5.6. Erosion Tests

The results from the erosion tests, with raw data shown in Table A1 in the Appendix, are depicted in Figure 28 and Figure 29. Pure PU eroded at a rate of 0.028 mg/g at 22°C. This rate increased nearly 8-fold and 30-fold at elevated temperatures of 60°C and 100°C, respectively. The observed trend resembles previous research by Hossain et al. [[6], [190]] where at 22°C the erosion rate for four pure commercial grade PU samples ranged from 0.016 mg/g to 0.054 mg/g. However, in the research by Hossain et al., on average, the erosion rate rose only by ~74% when the temperature was elevated to 100°C, with a maximum increase of ~325% for one of the four neat PU samples. It should be mentioned that the PU samples tested previously by Hossain et al. were different commercial grade materials and were also produced in a different manner as done for this research. Therefore, the material properties in the work by Hossein et al. may have been different compared to the PU samples that were used in the present research.

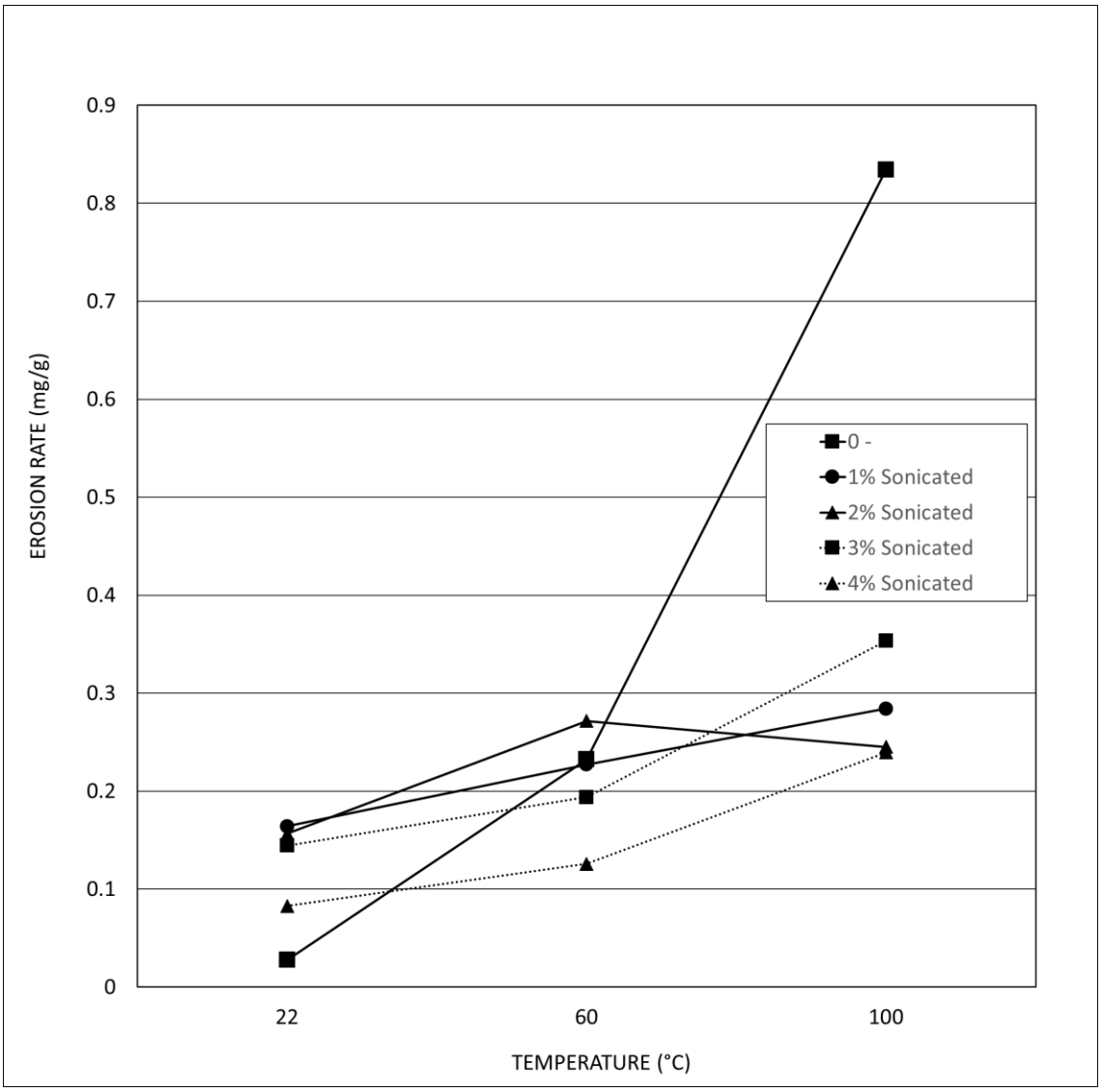

Figure 28: Erosion rate of sonicated GNP-PU nanocomposite samples at elevated temperature compared to pure PU

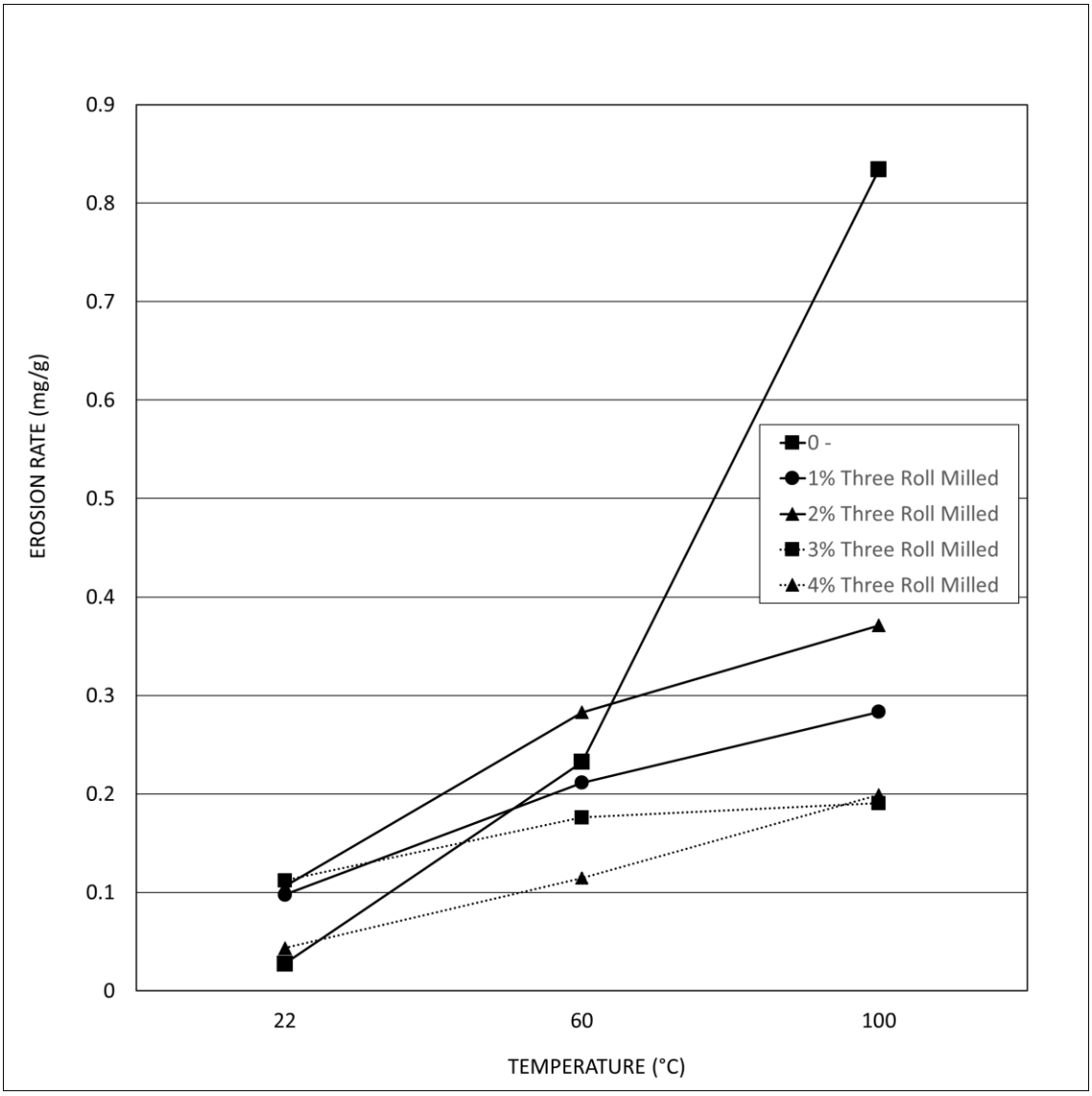

Figure 29: Erosion rate of 3RM GNP-PU nanocomposite samples at elevated temperature compared to pure PU

The results from this experiment with GNP reinforced PU showed that at 22°C, pure PU eroded at a lower rate compared to the GNP-PU nanocomposite samples. The introduction of 1 wt% GNP (by sonication as well as 3RM method) increased the erosion rate to 0.16 mg/g and 0.098 mg/g. But, with rising GNP filler loading it was possible to lower the erosion rate. At 4 wt% filler loading, the erosion rates were reduced to 0.083 mg/g and 0.043 mg/g for sonicated and 3RM samples, respectively. It is speculated that the initial introduction of GNP to the matrix may have obstructed some polymer chain formation during the curing process. This may have altered the ductility or hardness of the matrix itself, leading to higher erosion rates. Furthermore, with increase in GNP filler loading concentration in the matrix, the distance between each

GNP decreases. As van der Wall's forces increase with decrease in intermolecular distance, it can be deduced that due to this intermolecular attraction between GNP in the PU matrix, the erosion rate decreases with increase in GNP concentration in the matrix. With the combined effect of van der Waals-based interface cohesion, the GNP filler in this case acts as a reinforcement that keeps the matrix intact [191]–[194], [194]–[198].

While GNP reinforcement at low concentration deteriorates the erosive wear performance of polyurethane at room temperature, the filler plays a critical role in enhancing wear performance at elevated temperatures. Erosion tests for samples prepared by both sonication and 3RM showed that the presence of GNP reinforcement lowered the rate of erosion at 100°C when compared to pure PU. Even though erosion rates for GNP-PU nanocomposites still increased with rising temperature, the increase occurred at a much lower rate compared to pure PU. At 100°C, compared to pure PU, the erosion rate of the samples with 1 wt% GNP was 65.9% and 66% lower for the sonicated and 3RM GNP-PU samples, respectively. Similarly, at 100°C, the erosion rate of the sonicated and 3RM samples with 4 wt% GNP was 71.3% and 76.14% lower, respectively. With slight variances, in general, it can be noted that increasing GNP filler loading enhanced the erosive wear performance at elevated temperatures, with an overall better wear performance demonstrated by GNP-PU nanocomposites prepared by 3RM.

Average erosion rates over the three temperatures are plotted in Figure 30 for the samples with varying degree of filler loading and method of dispersion. This graph shows that erosion rates typically decreased with the increase in filler loading, with overall lower erosion rates demonstrated by the samples prepared by the 3RM method. The exception is the 2 wt% GNP nanocomposites, where the erosion rate of the 3RM samples are on average higher than those prepared by sonication. As discussed in Section 3.7.3, and referring to the results in Section 5.2 and 5.5, it can be deduced that due to some through-thickness filler alignment (perpendicular to the eroding surface) obtained by the 3RM method, the erosion rates of corresponding samples is lower than for samples prepared by the sonication process. For the 3RM samples, thermal conductivity in the axial direction (normal to the eroded surface) is also higher, and so is the bulk thermal conductivity due to conductive network formation. The thermal conductivity did not rise significantly at elevated temperatures, but it did rise with increase in filler loading. Since the erosion rate increased at a lower rate for the GNP-PU nanocomposite samples with increase in temperature, the increase in thermal conductivity is seen to be one of the reasons for lower erosion rate of the GNP-PU samples at elevated temperatures compared to pure PU. However, since the increase in thermal conductivity is

marginally higher compared to the level of improvement in the erosion rate at elevated temperatures of GNP-PU samples compared to pure PU samples, there may be other factors that are affecting the erosion rate.

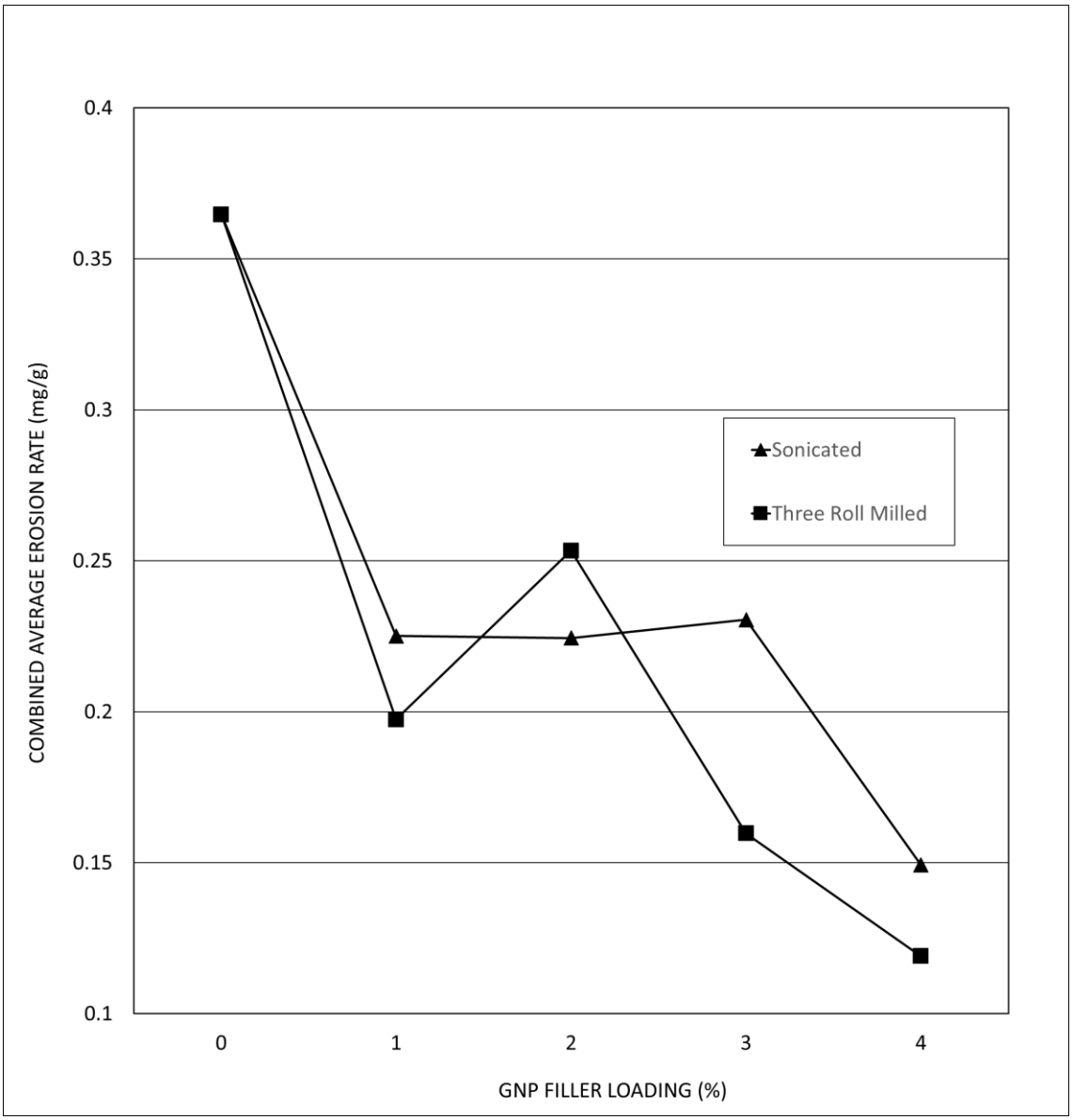

Figure 30: Combined average erosion rate with increase in filler loading for pure PU and GNP-PU nanocomposite samples

5.7. Surface Morphology Evaluation

After the erosion tests, the eroded surfaces were evaluated through SEM imaging for the pure PU sample and the 4 wt% GNP-PU_S and 4 wt% GNP-PU_{3RM} samples that were eroded at 22°C and 100°C. From the SEM image for the pure PU sample at eroded at 22°C, as shown in Figure 31, there is evidence of embedment of erodent particles into the surface. There is also the presence of small asperities, which, combined with the embedment of the erodent particles, suggest that the pure PU at 22°C underwent ductile erosion with plastic deformation. If it was brittle erosion, there would not be any embedment of the erodent particles on the eroded surface [6], [139], [142], [199], [200].

Figure 32 shows the SEM image of pure PU eroded at 100°C, under which condition the pure PU eroded the most. Asperities on the eroded surface are much larger and there is more embedment of the erodent particles. Increased plastic deformation and ductile erosion with rising temperature were the result of changes in PU material properties. As previously mentioned, with increase in temperature, ultimate strength and elastic modulus of polyurethane decreases, which may be the reason for the higher erosion rate [6].

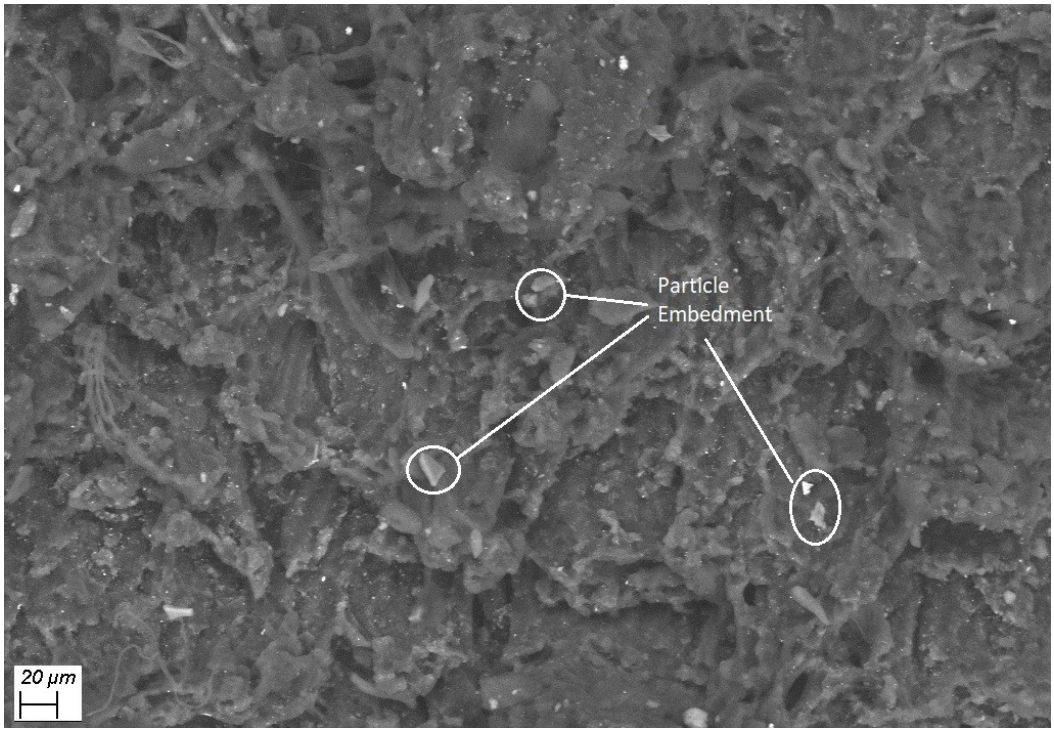

Figure 31: SEM image of eroded surface of pure PU at 22°C

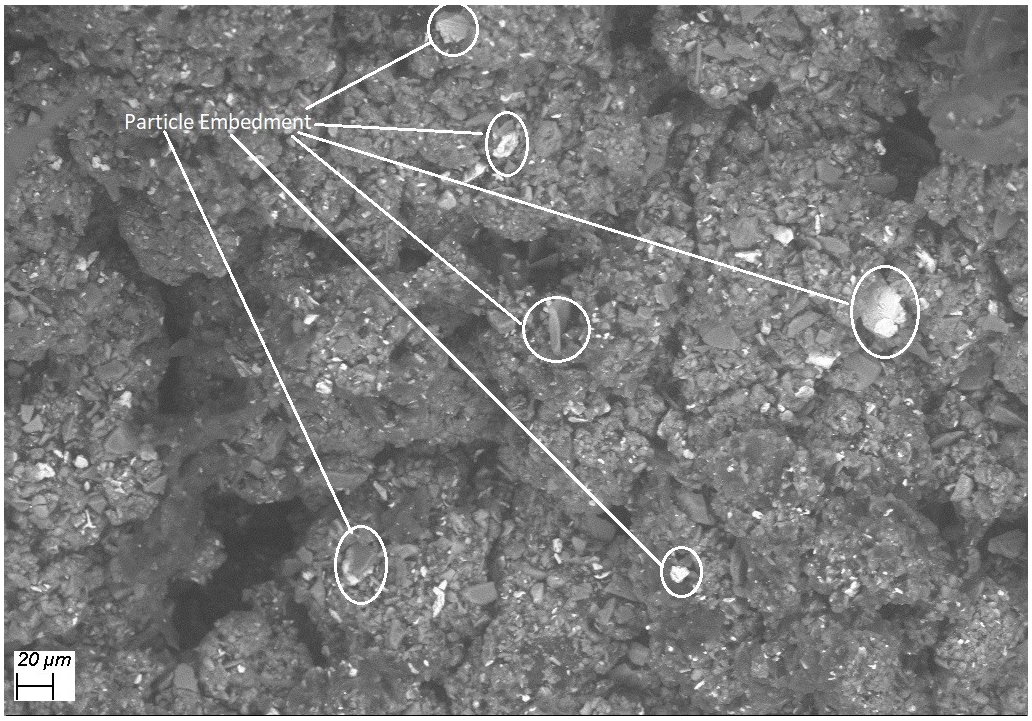

Figure 32: SEM image of eroded surface of pure PU at 100°C

For the 4 wt% GNP-PU_S nanocomposite samples, SEM imaging of the surface eroded at 22°C as seen in Figure 33, shows that the surface has fewer asperities, with noticeably less embedment of erodent particles, compared to the pure PU eroded at the same temperature. The surface appears to be smoother, and although subsurface cracks are not visible through SEM imaging, due to lower ductile erosion, the sample may have undergone more of brittle erosion. Previous research described a brittle to ductile erosion transition due to changes in kinetic energy of the solid eroding particles [201]. When erodent particles with low kinetic energies are used to erode brittle targets, the impacts lack the energy to initiate cracks, and thus the erosion in that case is ductile instead of brittle. In the present case, the erodent particles have the same kinetic energy in both the normal and tangential direction to the eroding surface. However, a potential ductile to brittle erosion transition may have taken place due to changes in the nanocomposite material physical properties imparted by the GNP reinforcement [145], [158], [160], [202].

SEM imaging of the eroded surface of the 4 wt% GNP-PU_S sample at 100°C, as shown in Figure 34, shows that there is little change in the surface morphology compared to the eroded surface at 22°C. There are small traces of solid particle embedment and small asperities and ridges present suggesting that there was some degree of ductile plastic deformation erosion at the elevated temperature.

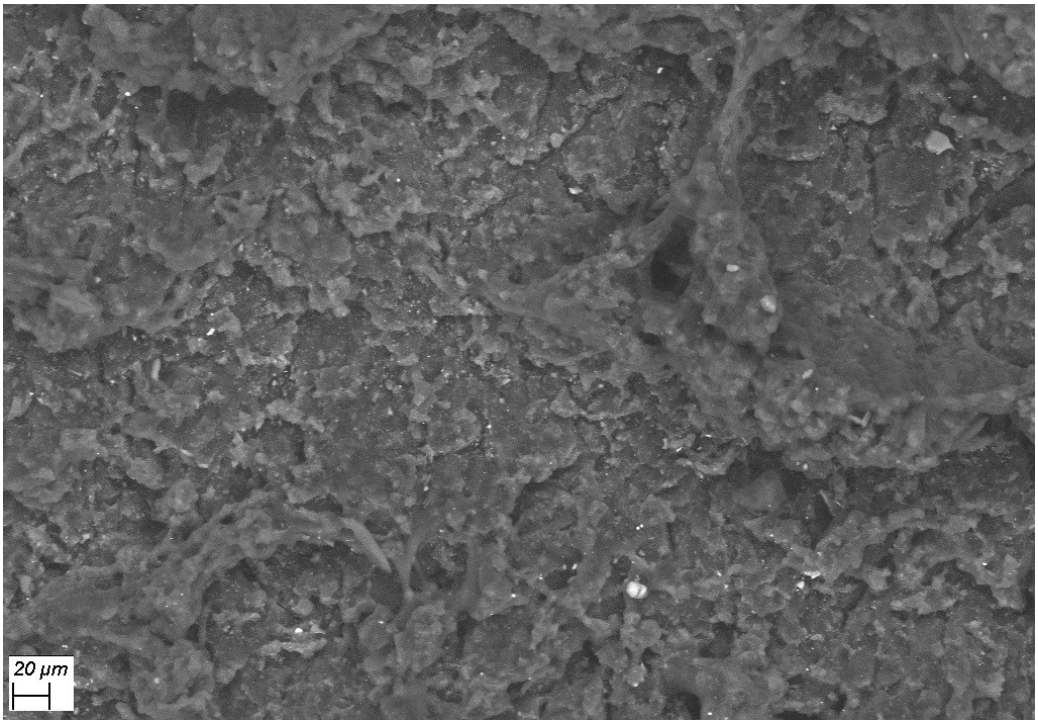

Figure 33: SEM image of eroded surface of 4 wt% GNP-PU sample prepared by sonication at 22°C

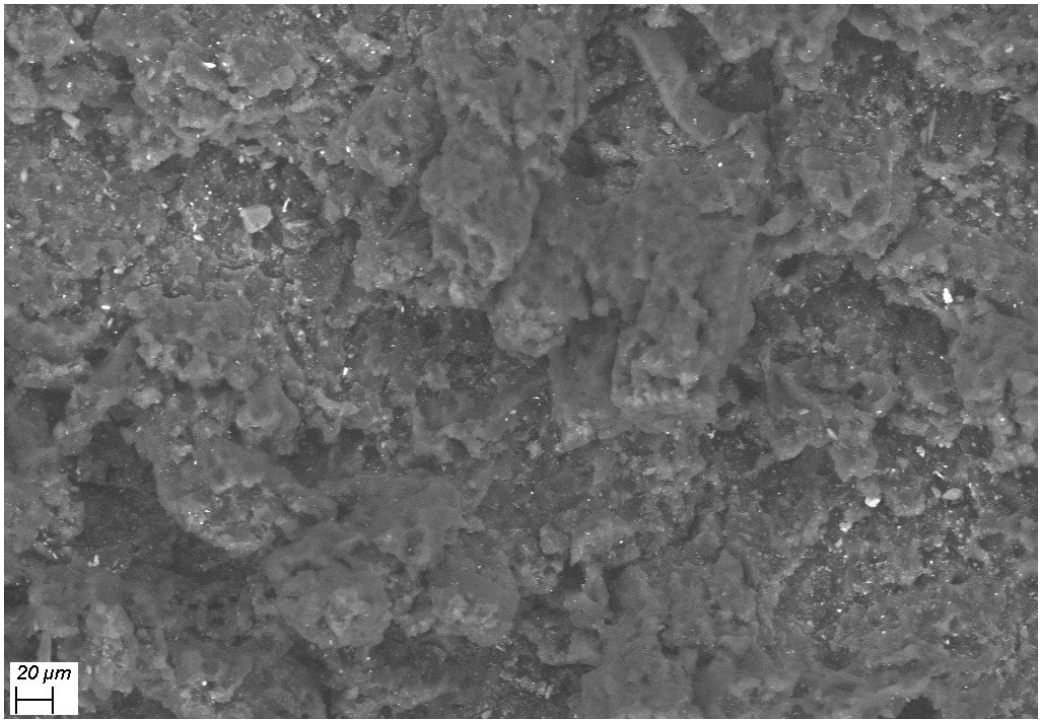

Figure 34: SEM image of eroded surface of 4 wt% GNP-PU sample prepared by sonication at 100°C

Recall that the rate of erosion for 4 wt% GNP-PU_{3RM} was typically lower than for sonicated samples, at 22°C and elevated temperatures of up to 100°C. Figure 35 shows a SEM image of the surface of the 4 wt% GNP-PU_{3RM} sample eroded at 22°C. The image indicates a similar level of surface roughness and mode of erosion compared to the samples prepared by sonication. On the other hand, for the 4 wt% GNP-PU_{3RM} sample eroded at 100°C, the surface appears to be smoother compared to the 4 wt% GNP-PU_S sample eroded at the same temperature, as seen in Figure 36. Asperities appear smaller for the 4 wt% GNP-PU_{3RM} sample which suggests that there was a lesser degree of ductile erosion in the 3RM samples at elevated temperature compared to the sonicated samples.

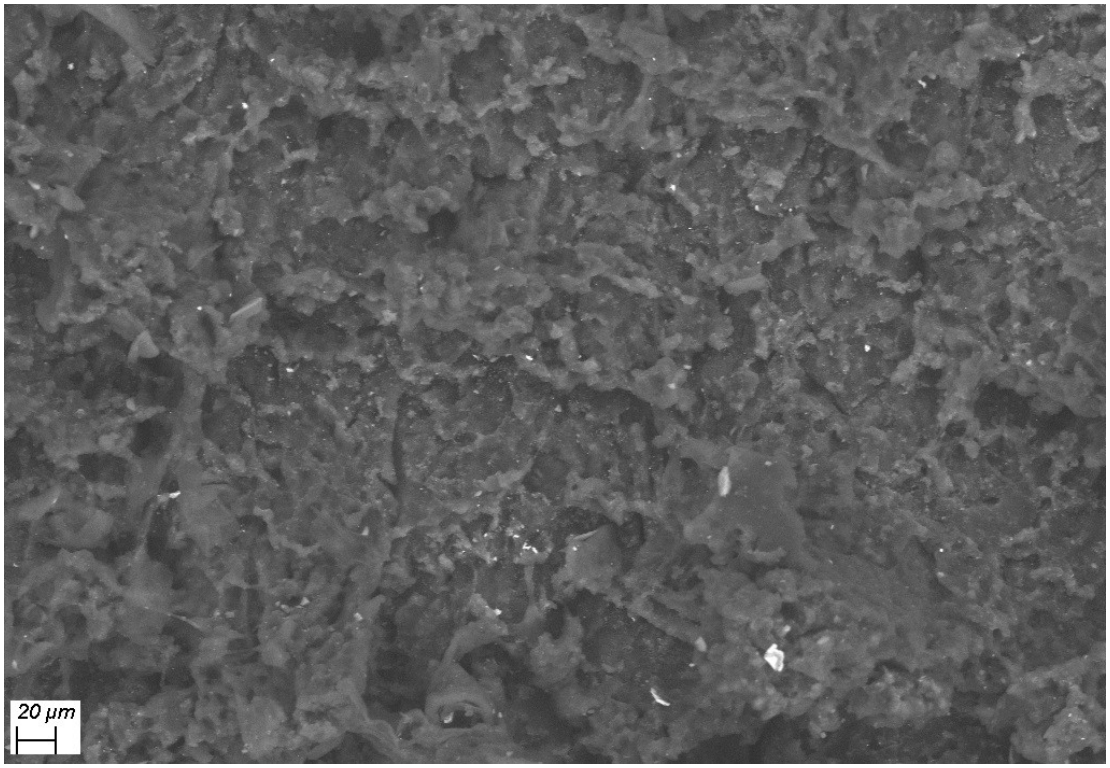

Figure 35: SEM image of eroded surface of 4 wt% GNP-PU sample prepared by 3RM at 22°C

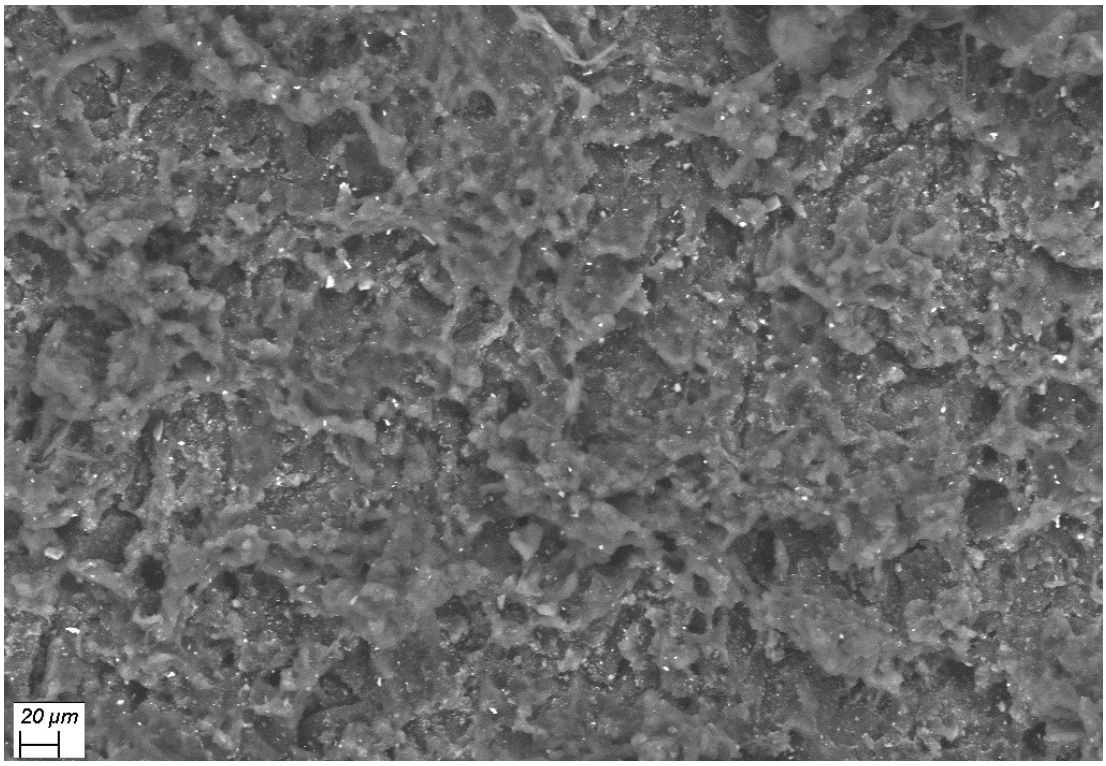

Figure 36: SEM image of eroded surface of 4 wt% GNP-PU sample prepared by 3RM at 100°C

6. Conclusions:

This research investigated the thermal conductivity and erosive wear resistance performance of polyurethane by embedding graphene nanoplatelets as reinforcement particles. Samples were prepared using sonication or three-roll milling as the method for filler dispersion in order to facilitate studying the effects of these methods on thermal conductivity and wear performance. SEM images of samples with dispersed GNP in PU showed that GNP was well distributed, except for a few noticeable agglomerates. It was also found that GNP can potentially self-align when in proximity to each other inside the matrix. By the sonication dispersion method, with increase in GNP filler loading, more dispersed GNP was attainable, and the degree of dispersion was found to increase. On the other hand, by 3RM, the degree of dispersion was found to be higher than the sonication method at lower filler loadings. However, unlike the sonication dispersion method, no significantly noticeable trend was found to conclude that the quality of dispersion increased with increasing filler loading in the 3RM method. An increase in d-spacing was ascertained at lower filler loading in the 3RM method suggesting there was potential intercalation of polymer chains through GNP layers. There was also no indication of settling of graphene platelets in the sonication method. On the contrary, XRD peak intensity counts were much larger in the bottom surface of the samples prepared by 3RM method, suggesting settling of graphene platelets.

With an increase in graphene filler loading, thermal conductivity was found to increase substantially. This increase was more prominent in samples prepared by three-roll milling compared to the sonication method. This phenomenon can be attributed to a higher degree of alignment by the 3RM dispersion method, allowing for better phonon transfer through quasi-percolating directional conductive network formation. At some instances, a sharp drop in thermal conductivity was noticed when filler loading was increased beyond 3 wt%. This effect may be caused by disrupted conductive network as a result of greater particle agglomeration. As mentioned above, there was some degree of settling of graphene, which gave higher thermal conductivity when testing samples with a low probing depth. Settling of GNP was observed for both the sonicated and 3RM samples, however it was more pronounced for nanocomposite samples prepared by 3RM. Overall, by comparing thermal conductivities from different probing depths, findings derived from thermal conductivity testing agreed with observations made by XRD analyses. It was deduced from these findings that the sonication process yielded more homogenous filler distribution and mitigated particle settling in the polyurethane matrix. Anisotropic thermal conductivity testing showed that regardless of the method of dispersion, there was some degree of anisotropy that may have been produced by particle alignment in the sample through-thickness direction during particle settling. The 3RM method caused a

greater degree of alignment of graphene platelets which resulted in a higher magnitude of thermal conductivity in the through-thickness direction.

The erosion rate of pure PU increased up to 30-fold at an elevated temperature of 100°C when compared to erosion at 22°C. With increasing filler loading, it was possible to achieve significantly lower erosion rates at higher temperatures. At 100°C, the erosion rate of the sample with 4 wt% filler loading was 71.3% and 76.14% lower for the sonicated and three-roll milled samples, respectively, compared to the pure polyurethane samples. On average, lower erosion rates were demonstrated by the samples prepared by the three-roll milling method, compared to those made by sonication. It can be deduced that due to graphene nanoplatelets being aligned in the through thickness direction in the samples prepared by three-roll milling, the erosion rate of these samples was lower than samples prepared by the sonication method. Since the thermal conductivity increased with filler loading, it can be considered to be one of the reasons for enhanced erosive wear performance of GNP-PU at elevated temperatures.

Evaluation of the surface morphology revealed that pure polyurethane underwent ductile erosion with plastic deformation. Due to change in material properties at elevated temperatures, ductile erosion mechanisms became dominant as judged by larger asperities and higher concentration of erodent particle embedment in the matrix. By reinforcing the matrix with graphene, a transition from ductile to brittle erosion was achieved, which is noticeable in the samples prepared by both sonication and three-roll milling. Hence, the erosive wear rate was lower at elevated temperatures due to the change in material properties and type of erosion, in addition to the increase in thermal conductivity. This research thus demonstrated the effectiveness of adding graphene filler to polyurethane liners to better wear performance at elevated temperatures.

7. Future Work Recommendation:

This research focussed on improving the erosive wear performance of polyurethane by incorporating graphene particles. Erosion tests at elevated temperatures were performed, yet, only one impingement angle (i.e. 30°) was tested. Further erosion testing may be done to evaluate wear performance at different angles to explore transitioning between ductile to brittle erosion. Erosion testing with different size erodent particles could also be explored to study their effect on the surface morphology. Potentially, the addition of graphene particles may also alter the material coefficient of friction. Hence, friction tests may be performed. Greater understanding of filler alignment effects should also be sought. Findings from such studies would be useful, for example, to the transportation industry as tires tend to wear faster at elevated temperatures. Conceivably, graphene particle enhance thermal conductivity can help reduce temperature elevation of tires during rigorous usage, as well as extend service life by reducing wear.

To reduce particle settling and re-agglomeration due to van der Wall's forces, sample preparation process may be modified to explore areas for improvements, for example, by utilising polymer resins that have a faster curing rate. More detailed material characterisation can also be performed using other techniques such as Raman spectroscopy for determining the filler platelet layer thickness or quality of exfoliation. Micro-CT or nano-CT scanning can also be explored to model the dispersion of graphene within the sample and detect agglomeration that might be present inside the nanocomposite samples, which otherwise is not noticeable through SEM imaging and XRD analysis alone.

As thermal conductivity enhancements and erosive wear performance of polymer nanocomposites depend on a large number of interconnected variable factors, further controlled experiments can be performed by altering some of these variables, such as using alternative filler materials of different shapes or sizes. Different filler concentrations, as well as alternative sample preparation processes can also be explored. As the overall quality of enhancement of the composite material is affected by the interaction by the matrix and the filler material, experiments with different matrix materials may also be evaluated.

References

[1] T. Alam, Md. Aminul Islam, and Z. N. Farhat, "Slurry Erosion of Pipeline Steel: Effect of Velocity and Microstructure," *J. Tribol.*, vol. 138, no. 2, pp. 021604-021604–10, Nov. 2015, doi: 10.1115/1.4031599.

[2] S. H. Bush, "The National Board of Boiler and Pressure Vessel Inspectors." [Online]. Available: http://www.nationalboard.org/. [Accessed: 22-Jan-2019].

[3] K. Juss and P. Mertiny, "Assessment of adhesion between polyurethane liner and epoxy based substrate: Methodology and experiment," *Polym. Test.*, vol. 28, no. 7, pp. 764–769, Oct. 2009, doi: 10.1016/j.polymertesting.2009.06.009.

[4] J. S. A, M. M. B, and H. T. B, "Erosion resistance testing of plastic pipes," *Achiev. Mater. Manuf. Eng.*, vol. 25, no. 2, 2007.

[5] P. Mertiny, K. Juss, and T. Bell, "Corrosion And Erosion Resistant Polymer Composite Pipe For Oil Sands Hydrotransport," presented at the Corrosion 2008, 2008.

[6] H. Ashrafizadeh, P. Mertiny, and A. McDonald, "Evaluation of the effect of temperature on mechanical properties and wear resistance of polyurethane elastomers," *Wear*, vol. 368–369, pp. 26–38, Dec. 2016, doi: 10.1016/j.wear.2016.08.008.

[7] U. Akram, "Graphite Nanoplatelet Filler-Modified Polyurethane Nanocomposites for Thermal Transport Enhancement," *ERA*, Nov-2017. [Online]. Available: https://era.library.ualberta.ca/items/586abc55-8bcf-49ee-907f-6e6c70d0c3c8. [Accessed: 20-Jan-2019].

[8] J. Rösler, Martin. Bäker, and Harald. Harders, "The structure of materials," in *Mechanical Behaviour of Engineering Materials*, Berlin, Heidelberg: Springer Berlin Heidelberg, 2007, pp. 1–29.

[9] D. S. Bag, *Principles of Polymers: An Advanced Book. Edited by Dibyendu Sekhar Bag*, UK ed. edition. New York: Nova Science Pub Inc, 2012.

[10] J. W. Nicholson, "Polymer chemistry," in *The Chemistry of Polymers*, 2006, pp. 1–22.

[11] D. Braun, H. Cherdron, M. Rehahn, H. Ritter, and B. Voit, *Polymer Synthesis: Theory and Practice: Fundamentals, Methods, Experiments*, 5th ed. Berlin Heidelberg: Springer-Verlag, 2013.

[12] J. Rösler, Martin. Bäker, and Harald. Harders, "Mechanical behaviour of polymers," in *Mechanical Behaviour of Engineering Materials*, Berlin, Heidelberg: Springer Berlin Heidelberg, 2007, pp. 257–293.

[13] D. G. Peiffer, "Degrees of freedom of polymeric molecules and their effect on physical properties," *J. Macromol. Sci. Part B*, vol. 15, no. 4, pp. 595–611, Nov. 1978, doi: 10.1080/00222347808212275.

[14] P. J. Flory and A. Vrij, "Melting Points of Linear-Chain Homologs. The Normal Paraffin Hydrocarbons," *J. Am. Chem. Soc.*, vol. 85, no. 22, pp. 3548–3553, Nov. 1963, doi: 10.1021/ja00905a004.

[15] J. W. Nicholson, "Crosslinking," in *The Chemistry of Polymers*, 2006, pp. 54–65.

[16] M. Chanda and S. K. Roy, "1. Industrial Polymers," in *Industrial Polymers, Specialty Polymers, and Their Applications*, CRC Press, 2008, pp. 1.1-1.159.

[17] J. B. de Oliveira, L. G. T. dos Reis, and F. Semaan, "Polyurethanes in analytical chemistry: A myriad of applications from sorbent foams to conductive materials and sensors," *Polyurethane Prop. Struct. Appl.*, pp. 1–24, Aug. 2012.

[18] T. Thomson, "Polyurethane Chemistry in Brief," in *Polyurethanes as Specialty Chemicals : Principles and Applications*, CRC Press, 2004, pp. 17–37.

[19] K. Ashida, "Chapter Two: Historical Developments of Polyurethane and Polyisocyanurate Foams," in *Polyurethane and Related Foams: Chemistry and Technology*, 1 edition., Boca Raton, FL: CRC Press, 2006, pp. 5–10.

[20] I. R. Clemitson, “Chapter 1 - Introduction,” in *Polyurethane Casting Primer*, CRC Press, 2011, pp. 1–9.
[21] L. I. Cavaco and J. A. Melo, *Polyurethane: Properties, structure and applications*. 2012.
[22] H. Ashrafizadeh, A. McDonald, and P. Mertiny, “Deposition of Electrically Conductive Coatings on Castable Polyurethane Elastomers by the Flame Spraying Process,” *J. Therm. Spray Technol.*, vol. 25, no. 3, pp. 419–430, Feb. 2016, doi: 10.1007/s11666-015-0376-2.
[23] P. Król, “Chapter One Introduction,” in *Linear Polyurethanes: Synthesis Methods, Chemical Structures, Properties and Applications*, 1 edition., Leiden ; Boston: CRC Press, 2008, pp. 1–5.
[24] Y. Wang, Z. Sun, J. Tian, H. Wang, H. Wang, and Y. Ji, “Influence of Environment on Ageing Behaviour of the Polyurethane Film,” *Mater. Sci.*, vol. 22, no. 2, pp. 290-294–294, Jan. 2016, doi: 10.5755/j01.ms.22.2.12935.
[25] H. M. C. C. Somarathna, S. N. Raman, K. H. Badri, A. A. Mutalib, D. Mohotti, and S. D. Ravana, “Quasi-Static Behavior of Palm-Based Elastomeric Polyurethane: For Strengthening Application of Structures under Impulsive Loadings,” *Polymers*, vol. 8, no. 5, p. 202, May 2016, doi: 10.3390/polym8050202.
[26] R. Zhou, D. H. Lu, Y. H. Jiang, and Q. N. Li, “Mechanical properties and erosion wear resistance of polyurethane matrix composites,” *Wear*, vol. 259, no. 1, pp. 676–683, Jul. 2005, doi: 10.1016/j.wear.2005.02.118.
[27] K. Ashida, “Chapter One: Introduction,” in *Polyurethane and Related Foams: Chemistry and Technology*, 1 edition., Boca Raton, FL: CRC Press, 2006, pp. 1–3.
[28] K. Ashida, “Chapter Three: Fundamentals,” in *Polyurethane and Related Foams: Chemistry and Technology*, 1 edition., Boca Raton, FL: CRC Press, 2006, pp. 11–64.
[29] I. R. Clemitson, “Chapter 2 - Fundamentals,” in *Polyurethane Casting Primer*, CRC Press, 2011, pp. 11–31.
[30] M. Szycher, “Structure–Property Relations in Polyurethanes,” in *Szycher’s Handbook of Polyurethanes, Second Edition*, 2 edition., Boca Raton, FL: CRC Press, 2012, pp. 37–86.
[31] M. Šercer, P. Raos, and M. Rujnic-Sokele, “Study on thermal properties of synthetic and bio-based polyurethane,” *Therm. Sci.*, vol. 19, pp. 165–165, Jan. 2013, doi: 10.2298/TSCI130629165S.
[32] W. Sakulsaknimitr, S. Wirasate, K. Pipatpanyanugoon, and P. Atorngitjawat, “Structure and Thermal Properties of Polyurethanes Synthesized from Cardanol Diol,” *J. Polym. Environ.*, vol. 23, no. 2, pp. 216–226, Jun. 2015, doi: 10.1007/s10924-014-0707-2.
[33] E. Orgiles-Calpena, P. Aran, A. M. Torró-Palau, E. Montiel-Parreño, and C. Orgilés-Barceló, “Sustainable Polyurethane Adhesives Derived from Carbon Dioxide,” *Polym. Renew. Resour.*, vol. 7, Sep. 2015, doi: 10.1177/204124791600700101.
[34] I. R. Clemitson, *Castable Polyurethane Elastomers*, 2nd Edition. CRC Press, 2008.
[35] P. Król, “Chapter Two Basic Raw Materials For The Production Of Linear Polyurethanes,” in *Linear Polyurethanes: Synthesis Methods, Chemical Structures, Properties and Applications*, 1 edition., Leiden ; Boston: CRC Press, 2008, pp. 7–16.
[36] G. Oertel and L. Abele, Eds., *Polyurethane handbook: chemistry, raw materials, processing, application, properties*, 2. ed. Munich: Hanser, 1994.
[37] M. Szycher, “Introduction,” in *Szycher’s Handbook of Polyurethanes, Second Edition*, 2 edition., Boca Raton, FL: CRC Press, 2012, pp. 1–12.
[38] M. Nayani, S. Gunashekar, and N. Abu-Zahra, “Synthesis and Characterization of Polyurethane-Nanoclay Composites,” *International Journal of Polymer Science*, 2013. [Online]. Available: https://www.hindawi.com/journals/ijps/2013/717895/. [Accessed: 24-Jan-2019].
[39] J. Rösler, Martin. Bäker, and Harald. Harders, “Mechanical behaviour of fibre reinforced composites,” in *Mechanical Behaviour of Engineering Materials*, Berlin, Heidelberg: Springer Berlin Heidelberg, 2007, pp. 295–325.
[40] V. R. A. Prakash and A. Rajadurai, “Mechanical, Thermal and Dielectric Characterization of Iron Oxide Particles Dispersed Glass Fiber Epoxy Resin Hybrid Composite,” *Dig. J. Nanomater. Biostructures*, vol. 11, no. 2, pp. 373–380, Jun. 2016.

[41] M. Kumaresan, S. S, and N. Karthi, “Effect of fiber orientation on mechanical properties of sisal fiber reinforced epoxy composites,” vol. 18, pp. 289–294, Jan. 2015, doi: 10.6180/jase.2015.18.3.09.
[42] S. Naseva, V. Srebrenkoska, S. Risteska, M. Stefanovska, and S. Srebrenkoska, “Mechanical Properties of Filament Wound Pipes: Effects of Winding Angles,” *Qual. Life Banja Luka - APEIRON*, vol. 11, no. 1–2, Jul. 2015, doi: 10.7251/QOL1501010N.
[43] T. P. Nguyen, “Applications of Polymer-Based Nanocomposites,” in *Polymer Composites*, John Wiley & Sons, Ltd, 2013, pp. 249–277.
[44] M. Alexandre and P. Dubois, “Polymer-layered silicate nanocomposites: preparation, properties and uses of a new class of materials,” *Mater. Sci. Eng. R Rep.*, vol. 28, no. 1, pp. 1–63, Jun. 2000, doi: 10.1016/S0927-796X(00)00012-7.
[45] A. Saritha, S. K. Malhotra, S. Thomas, K. Joseph, K. Goda, and M. S. Sreekala, “State of the Art – Nanomechanics,” in *Polymer Composites*, John Wiley & Sons, Ltd, 2013, pp. 1–12.
[46] Z. Han and A. Fina, “Thermal conductivity of carbon nanotubes and their polymer nanocomposites: A review,” *Prog. Polym. Sci.*, vol. 36, no. 7, pp. 914–944, Jul. 2011, doi: 10.1016/j.progpolymsci.2010.11.004.
[47] S. Agarwal and R. Gupta, “Thermal Conductivity of Polymer Nanocomposites,” in *Polymer Nanocomposites Handbook*, 1st Edition., CRC Press, 2009, p. 568.
[48] A. A. Balandin *et al.*, “Superior Thermal Conductivity of Single-Layer Graphene,” *Nano Lett.*, vol. 8, no. 3, pp. 902–907, Mar. 2008, doi: 10.1021/nl0731872.
[49] H. Chen *et al.*, “Thermal conductivity of polymer-based composites: Fundamentals and applications,” *Prog. Polym. Sci.*, vol. 59, pp. 41–85, Aug. 2016, doi: 10.1016/j.progpolymsci.2016.03.001.
[50] P. Deepalekshmi, P. M. Visakh, Aji. P. Mathew, A. K. Chandra, and S. Thomas, “Advances in Elastomers: Their Composites and Nanocomposites: State of Art, New Challenges and Opportunities,” in *Advances in Elastomers II: Composites and Nanocomposites*, P. M. Visakh, S. Thomas, A. K. Chandra, and Aji. P. Mathew, Eds. Berlin, Heidelberg: Springer Berlin Heidelberg, 2013, pp. 1–9.
[51] C. A. Stergiou, A. Z. Stimoniaris, and C. G. Delides, “Hybrid Nanocomposites With Organoclay and Carbon-Based Fillers for EMI Suppression,” *IEEE Trans. Electromagn. Compat.*, vol. 57, no. 3, pp. 470–476, Jun. 2015, doi: 10.1109/TEMC.2014.2384014.
[52] M. Oliveira and A. Machado, “Preparation of Polymer-Based Nanocomposites by Different Routes,” in *Nanocomposites: Synthesis, Characterization and Applications*, Nova, 2013, p. 21.
[53] Q. Zeng and A. Yu, “Theory and Simulation in Nanocomposites,” in *Polymer Composites*, John Wiley & Sons, Ltd, 2013, pp. 53–74.
[54] C. I. Idumah and A. Hassan, “Recently emerging trends in thermal conductivity of polymer nanocomposites,” *Rev. Chem. Eng.*, vol. 32, no. 4, pp. 413–457, 2016, doi: 10.1515/revce-2016-0004.
[55] A. Kausar, Z. Anwar, and B. Muhammad, “Recent Developments in Epoxy/Graphite, Epoxy/Graphene, and Epoxy/Graphene Nanoplatelet Composites: A Comparative Review,” *Polym.-Plast. Technol. Eng.*, vol. 55, no. 11, pp. 1192–1210, Jul. 2016, doi: 10.1080/03602559.2016.1163589.
[56] W. Evans, R. Prasher, J. Fish, P. Meakin, P. Phelan, and P. Keblinski, “Effect of aggregation and interfacial thermal resistance on thermal conductivity of nanocomposites and colloidal nanofluids,” *Int. J. Heat Mass Transf.*, vol. 51, no. 5, pp. 1431–1438, Mar. 2008, doi: 10.1016/j.ijheatmasstransfer.2007.10.017.
[57] N. Q. Khuyen, B. S. Kim, J. H. Byun, and S. Lee, “Mechanical Properties of VGCF/MAPP and Atmospheric Plasma-Treated VGCF/PP by Melt-Mixing Process,” *Adv. Compos. Mater.*, vol. 19, no. 4, pp. 381–392, Jan. 2010, doi: 10.1163/092430410X504161.

[58] D. Kotnarowska, M. Przerwa, and T. Szumiata, “Resistance to Erosive Wear of Epoxy-Polyurethane Coating Modified With Nanofillers,” *J. Mater. Sci. Res.*, vol. 3, p. 52, Feb. 2014, doi: 10.5539/jmsr.v3n2p52.
[59] X. Zheng *et al.*, “The effects of nanoparticle shape and orientation on the low frequency dielectric properties of nanocomposites,” *J. Mater. Sci.*, vol. 47, no. 12, pp. 4914–4920, Jun. 2012, doi: 10.1007/s10853-012-6364-8.
[60] R. Kotsilkova, E. Ivanov, D. Bychanok, A. Paddubskaya, and P. Kuzhir, “Effect of Matrix Viscosity on Rheological and Microwave Properties of Polymer Nanocomposites with Multiwall Carbon Nanotubes,” *J. Theor. Appl. Mech.*, vol. 44, pp. 83–96, Jun. 2014, doi: 10.2478/jtam-2014-0012.
[61] R. Taherian, “Experimental and analytical model for the electrical conductivity of polymer-based nanocomposites,” *Compos. Sci. Technol.*, vol. 123, pp. 17–31, Feb. 2016, doi: 10.1016/j.compscitech.2015.11.029.
[62] A. Naz, A. Kausar, and M. Siddiq, “Influence of Graphite Filler on Physicochemical Characteristics of Polymer/Graphite Composites: A Review,” *Polym.-Plast. Technol. Eng.*, vol. 55, no. 6, pp. 604–625, Apr. 2016, doi: 10.1080/03602559.2015.1098697.
[63] H. Ashton, “The Incorporation of Nanomaterials into Polymer Media,” in *Polymer Nanocomposites Handbook*, 1st Edition., CRC Press, 2009, p. 568.
[64] R. Y. Hong *et al.*, “Surface-modified silica nanoparticles for reinforcement of PMMA,” *J. Appl. Polym. Sci.*, vol. 105, no. 4, pp. 2176–2184, 2007, doi: 10.1002/app.26164.
[65] L. Wang, K. Wang, L. Chen, Y. Zhang, and C. He, “Preparation, morphology and thermal/mechanical properties of epoxy/nanoclay composite,” *Compos. Part Appl. Sci. Manuf.*, vol. 37, no. 11, pp. 1890–1896, Nov. 2006, doi: 10.1016/j.compositesa.2005.12.020.
[66] A. Patti, P. Russo, D. Acierno, and S. Acierno, “The effect of filler functionalization on dispersion and thermal conductivity of polypropylene/multi wall carbon nanotubes composites,” *Compos. Part B Eng.*, vol. 94, pp. 350–359, Jun. 2016, doi: 10.1016/j.compositesb.2016.03.072.
[67] F. Lionetto, E. Calò, F. Di Benedetto, D. Pisignano, and A. Maffezzoli, “A methodology to orient carbon nanotubes in a thermosetting matrix,” *Compos. Sci. Technol.*, vol. 96, pp. 47–55, May 2014, doi: 10.1016/j.compscitech.2014.02.016.
[68] B. E. Smith, H. Yazdani, and K. Hatami, “Three-dimensional imaging and quantitative analysis of dispersion and mechanical failure in filled nanocomposites,” *Compos. Part Appl. Sci. Manuf.*, vol. 79, pp. 23–29, Dec. 2015, doi: 10.1016/j.compositesa.2015.08.019.
[69] W. Benhadjala *et al.*, “Inorganic/organic nanocomposites: Reaching a high filler content without increasing viscosity using core-shell structured nanoparticles,” *Appl. Phys. Lett.*, vol. 107, no. 21, p. 211903, Nov. 2015, doi: 10.1063/1.4936339.
[70] M. Wang, D. Galpaya, Z. B. Lai, Y. Xu, and C. Yan, “Surface functionalization on the thermal conductivity of graphene–polymer nanocomposites,” *Int. J. Smart Nano Mater.*, vol. 5, no. 2, pp. 123–132, Apr. 2014, doi: 10.1080/19475411.2014.904828.
[71] P. B. Atienza, *Superconductivity in Graphene and Carbon Nanotubes: Proximity effect and nonlocal transport*. Springer International Publishing, 2014.
[72] A. K. Geim and K. S. Novoselov, “The rise of graphene,” *Nat. Mater.*, vol. 6, no. 3, pp. 183–191, Mar. 2007, doi: 10.1038/nmat1849.
[73] C. Lee, X. Wei, J. W. Kysar, and J. Hone, “Measurement of the Elastic Properties and Intrinsic Strength of Monolayer Graphene,” *Science*, vol. 321, no. 5887, pp. 385–388, Jul. 2008, doi: 10.1126/science.1157996.
[74] A. Naz, A. Kausar, M. Siddiq, and M. A. Choudhary, “Comparative Review on Structure, Properties, Fabrication Techniques, and Relevance of Polymer Nanocomposites Reinforced with Carbon Nanotube and Graphite Fillers,” *Polym.-Plast. Technol. Eng.*, vol. 55, no. 2, pp. 171–198, Jan. 2016, doi: 10.1080/03602559.2015.1055504.
[75] C. Dinh Van and T. Dinh Van, “The MEH-PPV/YAG:Ce Hybrid Nanocomposite Material for Solution Processing Fabrication of Optoelectronic Device,” *Journal of Nanomaterials*, 2015.

[Online]. Available: https://www.hindawi.com/journals/jnm/2015/313472/. [Accessed: 06-Jan-2019].
[76] S.-Y. Yang *et al.*, "Synergetic effects of graphene platelets and carbon nanotubes on the mechanical and thermal properties of epoxy composites," *Carbon*, vol. 49, no. 3, pp. 793–803, Mar. 2011, doi: 10.1016/j.carbon.2010.10.014.
[77] X. Sciences, "Technical Data Sheet-xGnP Graphene Nanoplatelets- Grade M." XG Sciences, 2015.
[78] Z. H. Ni *et al.*, "Graphene Thickness Determination Using Reflection and Contrast Spectroscopy," *Nano Lett.*, vol. 7, no. 9, pp. 2758–2763, Sep. 2007, doi: 10.1021/nl071254m.
[79] H. S. Kim, H. S. Bae, J. Yu, and S. Y. Kim, "Thermal conductivity of polymer composites with the geometrical characteristics of graphene nanoplatelets," *Sci. Rep.*, vol. 6, p. 26825, May 2016, doi: 10.1038/srep26825.
[80] S. G. Prolongo, R. Moriche, M. Sánchez, and A. Ureña, "Self-stratifying and orientation of exfoliated few-layer graphene nanoplatelets in epoxy composites," *Compos. Sci. Technol.*, vol. 85, pp. 136–141, Aug. 2013, doi: 10.1016/j.compscitech.2013.06.015.
[81] M. Martin-Gallego, M. M. Bernal, M. Hernandez, R. Verdejo, and M. A. Lopez-Manchado, "Comparison of filler percolation and mechanical properties in graphene and carbon nanotubes filled epoxy nanocomposites," *Eur. Polym. J.*, vol. 49, no. 6, pp. 1347–1353, Jun. 2013, doi: 10.1016/j.eurpolymj.2013.02.033.
[82] W. Steinmann *et al.*, "Extrusion of CNT-modified Polymers With Low Viscosity - Influence of Crystallization and CNT Orientation on the Electrical Propertie," *Polym. Polym. Compos.*, vol. 21, pp. 473–482, Oct. 2013, doi: 10.1177/096739111302100801.
[83] S. Y. Kim, Y. J. Noh, and J. Yu, "Thermal conductivity of graphene nanoplatelets filled composites fabricated by solvent-free processing for the excellent filler dispersion and a theoretical approach for the composites containing the geometrized fillers," *Compos. Part Appl. Sci. Manuf.*, vol. 69, pp. 219–225, Feb. 2015, doi: 10.1016/j.compositesa.2014.11.018.
[84] P.-C. Ma, N. A. Siddiqui, G. Marom, and J.-K. Kim, "Dispersion and functionalization of carbon nanotubes for polymer-based nanocomposites: A review," *Compos. Part Appl. Sci. Manuf.*, vol. 41, no. 10, pp. 1345–1367, Oct. 2010, doi: 10.1016/j.compositesa.2010.07.003.
[85] R. Janardhan, K. Ramamurthy, and J. S. Anand, "Solution properties of polyurethane," *Polym. Test.*, vol. 13, no. 5, pp. 397–404, Jan. 1994, doi: 10.1016/0142-9418(94)90049-3.
[86] S. N. Bhattacharya, M. R. Kamal, and R. K. Gupta, *Polymeric Nanocomposites: Theory and Practice*. München: Carl Hanser Verlag GmbH & Co. KG, 2007.
[87] M. Moniruzzaman and K. I. Winey, "Polymer Nanocomposites Containing Carbon Nanotubes," *Macromolecules*, vol. 39, no. 16, pp. 5194–5205, Aug. 2006, doi: 10.1021/ma060733p.
[88] G. Mittal, V. Dhand, K. Y. Rhee, S.-J. Park, and W. R. Lee, "A review on carbon nanotubes and graphene as fillers in reinforced polymer nanocomposites," *J. Ind. Eng. Chem.*, vol. 21, pp. 11–25, Jan. 2015, doi: 10.1016/j.jiec.2014.03.022.
[89] "Surface tension values of some common test liquids for surface energy analysis." [Online]. Available: http://www.surface-tension.de/. [Accessed: 02-Feb-2019].
[90] A. Ciesielski and P. Samorì, "Graphene via sonication assisted liquid-phase exfoliation," *Chem. Soc. Rev.*, vol. 43, no. 1, pp. 381–398, Dec. 2013, doi: 10.1039/C3CS60217F.
[91] Y. Xu, H. Cao, Y. Xue, B. Li, and W. Cai, "Liquid-Phase Exfoliation of Graphene: An Overview on Exfoliation Media, Techniques, and Challenges," *Nanomaterials*, vol. 8, no. 11, Nov. 2018, doi: 10.3390/nano8110942.
[92] H. D. d'Oliveira, X. Davoy, E. Arche, P. Malfreyt, and A. Ghoufi, "Test-area surface tension calculation of the graphene-methane interface: Fluctuations and commensurability," *J. Chem. Phys.*, vol. 146, no. 21, p. 214112, Jun. 2017, doi: 10.1063/1.4984577.
[93] Q.-A. Poutrel, Z. Wang, D. Wang, C. Soutis, and M. Gresil, "Effect of pre and Post-Dispersion on Electro-Thermo-Mechanical Properties of a Graphene Enhanced Epoxy," *Appl. Compos. Mater.*, vol. 24, no. 2, pp. 313–336, Apr. 2017, doi: 10.1007/s10443-016-9541-0.

[94] F. Wang, L. T. Drzal, Y. Qin, and Z. Huang, "Mechanical properties and thermal conductivity of graphene nanoplatelet/epoxy composites," *J. Mater. Sci.*, vol. 50, no. 3, pp. 1082–1093, Feb. 2015, doi: 10.1007/s10853-014-8665-6.
[95] J. Li, P. C. Ma, W. S. Chow, C. K. To, B. Z. Tang, and J.-K. Kim, "Correlations between Percolation Threshold, Dispersion State, and Aspect Ratio of Carbon Nanotubes," *Adv. Funct. Mater.*, vol. 17, no. 16, pp. 3207–3215, 2007, doi: 10.1002/adfm.200700065.
[96] A. Yasmin, J.-J. Luo, and I. M. Daniel, "Processing of expanded graphite reinforced polymer nanocomposites," *Compos. Sci. Technol.*, vol. 66, no. 9, pp. 1182–1189, Jul. 2006, doi: 10.1016/j.compscitech.2005.10.014.
[97] D. Pedrazzoli, A. Pegoretti, and K. Kalaitzidou, "Synergistic effect of exfoliated graphite nanoplatelets and short glass fiber on the mechanical and interfacial properties of epoxy composites," *Compos. Sci. Technol.*, vol. 98, pp. 15–21, Jun. 2014, doi: 10.1016/j.compscitech.2014.04.019.
[98] A. Tessema *et al.*, "Effect of filler loading, geometry, dispersion and temperature on thermal conductivity of polymer nanocomposites," *Polym. Test.*, vol. 57, pp. 101–106, Feb. 2017, doi: 10.1016/j.polymertesting.2016.11.015.
[99] Y. S. Song and J. R. Youn, "Influence of dispersion states of carbon nanotubes on physical properties of epoxy nanocomposites," *Carbon*, vol. 43, no. 7, pp. 1378–1385, Jun. 2005, doi: 10.1016/j.carbon.2005.01.007.
[100] F. Yavari *et al.*, "Enhanced Thermal Conductivity in a Nanostructured Phase Change Composite due to Low Concentration Graphene Additives," *J. Phys. Chem. C*, vol. 115, no. 17, pp. 8753–8758, May 2011, doi: 10.1021/jp200838s.
[101] P. He *et al.*, "Surface modification and ultrasonication effect on the mechanical properties of carbon nanofiber/polycarbonate composites," *Compos. Part Appl. Sci. Manuf.*, vol. 37, no. 9, pp. 1270–1275, Sep. 2006, doi: 10.1016/j.compositesa.2005.08.008.
[102] R. Atif and F. Inam, "Reasons and remedies for the agglomeration of multilayered graphene and carbon nanotubes in polymers," *Beilstein J. Nanotechnol.*, vol. 7, no. 1, pp. 1174–1196, Aug. 2016, doi: 10.3762/bjnano.7.109.
[103] M. A. Raza, A. V. K. Westwood, A. P. Brown, and C. Stirling, "Texture, transport and mechanical properties of graphite nanoplatelet/silicone composites produced by three roll mill," *Compos. Sci. Technol.*, vol. 72, no. 3, pp. 467–475, Feb. 2012, doi: 10.1016/j.compscitech.2011.12.010.
[104] S. Chandrasekaran, C. Seidel, and K. Schulte, "Preparation and characterization of graphite nano-platelet (GNP)/epoxy nano-composite: Mechanical, electrical and thermal properties," *Eur. Polym. J.*, vol. 49, no. 12, pp. 3878–3888, Dec. 2013, doi: 10.1016/j.eurpolymj.2013.10.008.
[105] I. D. Rosca and S. V. Hoa, "Highly conductive multiwall carbon nanotube and epoxy composites produced by three-roll milling," *Carbon*, vol. 47, no. 8, pp. 1958–1968, Jul. 2009, doi: 10.1016/j.carbon.2009.03.039.
[106] M. Lampinen, M. E. H. Assad, and E. F. Curd, "4 - PHYSICAL FUNDAMENTALS," in *Industrial Ventilation Design Guidebook*, H. Goodfellow and E. Tähti, Eds. San Diego: Academic Press, 2001, pp. 41–171.
[107] M. Maldovan, "Sound and heat revolutions in phononics," *Nature*, vol. 503, no. 7475, pp. 209–217, Nov. 2013, doi: 10.1038/nature12608.
[108] J.-H. Lee *et al.*, "25th Anniversary Article: Ordered Polymer Structures for the Engineering of Photons and Phonons," *Adv. Mater.*, vol. 26, no. 4, pp. 532–569, 2014, doi: 10.1002/adma.201303456.
[109] A. Li, C. Zhang, and Y.-F. Zhang, "Thermal Conductivity of Graphene-Polymer Composites: Mechanisms, Properties, and Applications," *Polymers*, vol. 9, no. 9, p. 437, Sep. 2017, doi: 10.3390/polym9090437.
[110] T. M. Tritt, Ed., "Theory, Properties, and Applications," in *Thermal Conductivity*, 2004th ed., Berlin: Springer US, 2004, p. 284.

[111] A. A. Balandin, “Thermal properties of graphene and nanostructured carbon materials,” *Nat. Mater.*, vol. 10, no. 8, pp. 569–581, Jul. 2011, doi: 10.1038/nmat3064.
[112] H. H. Pu, S. H. Rhim, C. J. Hirschmugl, M. Gajdardziska-Josifovska, M. Weinert, and J. H. Chen, “Anisotropic thermal conductivity of semiconducting graphene monoxide,” *Appl. Phys. Lett.*, vol. 102, no. 22, p. 223101, Jun. 2013, doi: 10.1063/1.4808448.
[113] A. L. Moore and L. Shi, “Emerging challenges and materials for thermal management of electronics,” *Mater. Today*, vol. 17, no. 4, pp. 163–174, May 2014, doi: 10.1016/j.mattod.2014.04.003.
[114] E. Pop, V. Varshney, and A. K. Roy, “Thermal properties of graphene: Fundamentals and applications,” *MRS Bull.*, vol. 37, no. 12, pp. 1273–1281, Dec. 2012, doi: 10.1557/mrs.2012.203.
[115] L. Zeng *et al.*, “Measuring Phonon Mean Free Path Distributions by Probing Quasiballistic Phonon Transport in Grating Nanostructures,” *Sci. Rep.*, vol. 5, p. 17131, Nov. 2015, doi: 10.1038/srep17131.
[116] H. Kakemoto, *Theoretical specific heat, and thermal conductivity estimated by detailed phonon vibrations*. 2018.
[117] K. E. Goodson, M. I. Flik, L. T. Su, and D. A. Antoniadis, “Prediction and Measurement of the Thermal Conductivity of Amorphous Dielectric Layers,” *J. Heat Transf.*, vol. 116, no. 2, pp. 317–324, May 1994, doi: 10.1115/1.2911402.
[118] P. J. Cumpson, “Estimation of inelastic mean free paths for polymers and other organic materials: use of quantitative structure–property relationships,” *Surf. Interface Anal.*, vol. 31, no. 1, pp. 23–34, 2001, doi: 10.1002/sia.948.
[119] Henry, A, “Chapter 13: Thermal Transport in Polymers,” in *Annual Review of Heat Transfer*, vol. 17, 21 vols., Atlanta, Georgia: Semantic Scholar, 2014, pp. 485–520.
[120] Y. Song, C. Yang, D. Liu, Y. Lin, and C. W. Nan, “Self-orientation of graphite-nanoplates induces anisotropy of nanoplates-epoxy composites,” *Ceram. Int.*, vol. 38, pp. S91–S94, Jan. 2012, doi: 10.1016/j.ceramint.2011.04.057.
[121] T. Luo and J. R. Lloyd, “Enhancement of Thermal Energy Transport Across Graphene/Graphite and Polymer Interfaces: A Molecular Dynamics Study,” *Adv. Funct. Mater.*, vol. 22, no. 12, pp. 2495–2502, 2012, doi: 10.1002/adfm.201103048.
[122] S. Shenogin, L. Xue, R. Ozisik, P. Keblinski, and D. G. Cahill, “Role of thermal boundary resistance on the heat flow in carbon-nanotube composites,” *J. Appl. Phys.*, vol. 95, no. 12, pp. 8136–8144, Jun. 2004, doi: 10.1063/1.1736328.
[123] C.-W. Nan, G. Liu, Y. Lin, and M. Li, “Interface effect on thermal conductivity of carbon nanotube composites,” *Appl. Phys. Lett.*, vol. 85, no. 16, pp. 3549–3551, Oct. 2004, doi: 10.1063/1.1808874.
[124] M.-T. Hung, O. Choi, Y. S. Ju, and H. T. Hahn, “Heat conduction in graphite-nanoplatelet-reinforced polymer nanocomposites,” *Appl. Phys. Lett.*, vol. 89, no. 2, p. 023117, Jul. 2006, doi: 10.1063/1.2221874.
[125] M. B. Bryning, D. E. Milkie, M. F. Islam, J. M. Kikkawa, and A. G. Yodh, “Thermal conductivity and interfacial resistance in single-wall carbon nanotube epoxy composites,” *Appl. Phys. Lett.*, vol. 87, no. 16, p. 161909, Oct. 2005, doi: 10.1063/1.2103398.
[126] F. H. Gojny *et al.*, “Evaluation and identification of electrical and thermal conduction mechanisms in carbon nanotube/epoxy composites,” *Polymer*, vol. 47, no. 6, pp. 2036–2045, Mar. 2006, doi: 10.1016/j.polymer.2006.01.029.
[127] C. H. Liu and S. S. Fan, “Effects of chemical modifications on the thermal conductivity of carbon nanotube composites,” *Appl. Phys. Lett.*, vol. 86, no. 12, p. 123106, Mar. 2005, doi: 10.1063/1.1887839.
[128] A. Yu, P. Ramesh, X. Sun, E. Bekyarova, M. E. Itkis, and R. C. Haddon, “Enhanced Thermal Conductivity in a Hybrid Graphite Nanoplatelet – Carbon Nanotube Filler for Epoxy Composites,” *Adv. Mater.*, vol. 20, no. 24, pp. 4740–4744, 2008, doi: 10.1002/adma.200800401.

[129] E.-C. Cho *et al.*, “Graphene-based thermoplastic composites and their application for LED thermal management,” *Carbon*, vol. 102, pp. 66–73, Jun. 2016, doi: 10.1016/j.carbon.2016.01.097.
[130] Z. Tang, H. Kang, Z. Shen, B. Guo, L. Zhang, and D. Jia, “Grafting of Polyester onto Graphene for Electrically and Thermally Conductive Composites,” *Macromolecules*, vol. 45, no. 8, pp. 3444–3451, Apr. 2012, doi: 10.1021/ma300450t.
[131] P. Zong *et al.*, “Effect of aminopropylisobutyl polyhedral oligomeric silsesquioxane functionalized graphene on the thermal conductivity and electrical insulation properties of epoxy composites,” *RSC Adv.*, vol. 6, no. 13, pp. 10498–10506, Jan. 2016, doi: 10.1039/C5RA24885J.
[132] J. Gu, C. Xie, H. Li, J. Dang, W. Geng, and Q. Zhang, “Thermal percolation behavior of graphene nanoplatelets/polyphenylene sulfide thermal conductivity composites,” *Polym. Compos.*, vol. 35, no. 6, pp. 1087–1092, 2014, doi: 10.1002/pc.22756.
[133] O. Almanza, M. A. Rodríguez-Pérez, and J. A. De Saja, “Applicability of the transient plane source method to measure the thermal conductivity of low-density polyethylene foams: Transient Plane Source Method,” *J. Polym. Sci. Part B Polym. Phys.*, vol. 42, no. 7, pp. 1226–1234, Apr. 2004, doi: 10.1002/polb.20005.
[134] Y. He, “Rapid thermal conductivity measurement with a hot disk sensor,” *Thermochim. Acta*, vol. 436, no. 1–2, pp. 122–129, Oct. 2005, doi: 10.1016/j.tca.2005.06.026.
[135] C. Dixon, “Transient Plane Source Technique for Measuring Thermal Properties of Silicone Materials Used in Electronic Assemblies,” vol. 23, no. 4, p. 7, 2000.
[136] G. Stachowiak and A. W. Batchelor, *Engineering Tribology*, 4th Edition. Butterworth-Heinemann, 2011.
[137] M. K. Padhy and R. P. Saini, “A review on silt erosion in hydro turbines,” *Renew. Sustain. Energy Rev.*, vol. 12, no. 7, pp. 1974–1987, 2008.
[138] C. A. R. Duarte, F. J. de Souza, and V. F. dos Santos, “Mitigating elbow erosion with a vortex chamber,” *Powder Technol.*, vol. 288, pp. 6–25, Jan. 2016, doi: 10.1016/j.powtec.2015.10.032.
[139] V. Javaheri, D. Porter, and V.-T. Kuokkala, “Slurry erosion of steel – Review of tests, mechanisms and materials,” *Wear*, vol. 408–409, pp. 248–273, Aug. 2018, doi: 10.1016/j.wear.2018.05.010.
[140] S. S. Kumar, *Handbook Of Polymer Tribology*. World Scientific, 2018.
[141] H. Arabnejad, “(PDF) Evaluation of Solid Particle Erosion Equations and Models for Oil and Gas Industry Applications,” *ResearchGate*. [Online]. Available: https://www.researchgate.net/publication/301406001_Evaluation_of_Solid_Particle_Erosion_Equations_and_Models_for_Oil_and_Gas_Industry_Applications. [Accessed: 04-Feb-2019].
[142] I. Finnie, “Erosion of surfaces by solid particles,” *Wear*, vol. 3, no. 2, pp. 87–103, Mar. 1960, doi: 10.1016/0043-1648(60)90055-7.
[143] I. Finnie, “Some reflections on the past and future of erosion,” *Wear*, vol. 186–187, pp. 1–10, Jul. 1995, doi: 10.1016/0043-1648(95)07188-1.
[144] I. Finnie, G. R. Stevick, and J. R. Ridgely, “The influence of impingement angle on the erosion of ductile metals by angular abrasive particles,” *Wear*, vol. 152, no. 1, pp. 91–98, Jan. 1992, doi: 10.1016/0043-1648(92)90206-N.
[145] Y. M. Abd-Elrhman, A. Abouel-Kasem, K. M. Emara, and S. M. Ahmed, “Effect of Impact Angle on Slurry Erosion Behavior and Mechanisms of Carburized AISI 5117 Steel,” *J. Tribol.*, vol. 136, no. 1, pp. 011106-011106–9, Nov. 2013, doi: 10.1115/1.4025874.
[146] H. McI. Clark and K. K. Wong, “Impact angle, particle energy and mass loss in erosion by dilute slurries,” *Wear*, vol. 186–187, pp. 454–464, Aug. 1995, doi: 10.1016/0043-1648(95)07120-2.
[147] M. Parsi, K. Najmi, F. Najafifard, S. Hassani, B. S. McLaury, and S. A. Shirazi, “A comprehensive review of solid particle erosion modeling for oil and gas wells and pipelines applications,” *J. Nat. Gas Sci. Eng.*, vol. 21, pp. 850–873, Nov. 2014, doi: 10.1016/j.jngse.2014.10.001.
[148] A. V. Levy, “The solid particle erosion behavior of steel as a function of microstructure,” *Wear*, vol. 68, no. 3, pp. 269–287, May 1981, doi: 10.1016/0043-1648(81)90177-0.

[149] Z. Ping, L. Youwei, Y. Chengqing, and L. Jian, “Erosion Behaviors of Elastic Polymer Coatings,” in *Advanced Tribology*, 2010, pp. 738–741.
[150] R. A. Beck and R. W. Truss, “Effect of chemical structure on the wear behaviour of polyurethane-urea elastomers,” *Wear*, vol. 218, no. 2, pp. 145–152, Jul. 1998, doi: 10.1016/S0043-1648(98)00219-1.
[151] J. Li and I. M. Hutchings, “Resistance of cast polyurethane elastomers to solid particle erosion,” *Wear*, vol. 135, no. 2, pp. 293–303, Jan. 1990, doi: 10.1016/0043-1648(90)90032-6.
[152] I. M. Hutchings, D. W. T. Deuchar, and A. H. Muhr, “Erosion of unfilled elastomers by solid particle impact,” *J. Mater. Sci.*, vol. 22, no. 11, pp. 4071–4076, Nov. 1987, doi: 10.1007/BF01133360.
[153] J. David Ivan and J. M.E., *Abrasion of rubber*, 1st ed. MacLaren, 1967.
[154] A. H. Muhr and A. D. Roberts, “Rubber abrasion and wear,” *Wear*, vol. 158, no. 1, pp. 213–228, Oct. 1992, doi: 10.1016/0043-1648(92)90040-F.
[155] N. Zhang, F. Yang, L. Li, C. Shen, J. Castro, and L. J. Lee, “Thickness effect on particle erosion resistance of thermoplastic polyurethane coating on steel substrate,” *Wear*, vol. 303, no. 1, pp. 49–55, Jun. 2013, doi: 10.1016/j.wear.2013.02.022.
[156] S. W. Zhang, W. Deguo, and Y. Weihua, “Investigation of abrasive erosion of polymers,” *J. Mater. Sci.*, vol. 30, no. 18, pp. 4561–4566, Sep. 1995, doi: 10.1007/BF01153063.
[157] R. F. de Farias, L. Martinez, and C. Airoldi, “Decrease of interlamellar spacing of silica samples induced by external pressure,” *J. Non-Cryst. Solids*, vol. 276, no. 1, pp. 56–60, Oct. 2000, doi: 10.1016/S0022-3093(00)00277-5.
[158] N. Miyazaki, “Solid particle erosion of composite materials: A critical review,” *J. Compos. Mater.*, vol. 50, no. 23, pp. 3175–3217, Sep. 2016, doi: 10.1177/0021998315617818.
[159] G. P. Tilly, “Erosion caused by airborne particles,” *Wear*, vol. 14, no. 1, pp. 63–79, Jul. 1969, doi: 10.1016/0043-1648(69)90035-0.
[160] G. P. Tilly and W. Sage, “The interaction of particle and material behaviour in erosion processes,” *Wear*, vol. 16, no. 6, pp. 447–465, Dec. 1970, doi: 10.1016/0043-1648(70)90171-7.
[161] J. Zahavi and G. F. Schmitt, “Solid particle erosion of reinforced composite materials,” *Wear*, vol. 71, no. 2, pp. 179–190, Sep. 1981, doi: 10.1016/0043-1648(81)90337-9.
[162] L. Zhou, H. Zhang, X. Pei, K. Friedrich, C. Eger, and Z. Zhang, “Erosive wear of transparent nanocomposite coatings,” *Tribol. Int.*, vol. 61, pp. 62–69, May 2013, doi: 10.1016/j.triboint.2012.11.021.
[163] J. Chen, I. M. Hutchings, T. Deng, M. S. A. Bradley, and K. K. K. Koziol, “The effect of carbon nanotube orientation on erosive wear resistance of CNT-epoxy based composites,” *Carbon*, vol. 73, pp. 421–431, Jul. 2014, doi: 10.1016/j.carbon.2014.02.083.
[164] G02 Committee, “Test Method for Conducting Erosion Tests by Solid Particle Impingement Using Gas Jets,” ASTM International.
[165] J. Cho, I. Jeon, S. Y. Kim, S. Lim, and J. Y. Jho, “Improving Dispersion and Barrier Properties of Polyketone/Graphene Nanoplatelet Composites via Noncovalent Functionalization Using Aminopyrene,” *ACS Appl. Mater. Interfaces*, vol. 9, no. 33, pp. 27984–27994, Aug. 2017, doi: 10.1021/acsami.7b10474.
[166] S. Swapp, “Scanning Electron Microscopy (SEM),” *Techniques*. [Online]. Available: https://serc.carleton.edu/research_education/geochemsheets/techniques/SEM.html. [Accessed: 30-Jan-2019].
[167] “EVO Family - Your Modular SEM Platform for Intuitive Operation, Routine Investigations and Research Applications.” [Online]. Available: https://www.zeiss.com/microscopy/int/products/scanning-electron-microscopes/evo.html. [Accessed: 28-Jan-2019].
[168] F. Bensadoun, N. Kchit, C. Billotte, F. Trochu, and E. Ruiz, “A Comparative Study of Dispersion Techniques for Nanocomposite Made with Nanoclays and an Unsaturated Polyester Resin,”

Journal of Nanomaterials, 2011. [Online]. Available: https://www.hindawi.com/journals/jnm/2011/406087/. [Accessed: 30-Jan-2019].
[169] P. P. Ewald, "Introduction to the dynamical theory of X-ray diffraction," *Acta Crystallogr. A*, vol. 25, no. 1, pp. 103–108, Jan. 1969, doi: 10.1107/S0567739469000155.
[170] V. Causin, "Characterization of Nanocomposites by Scattering Methods," in *Polymer Composites*, John Wiley & Sons, Ltd, 2013, pp. 75–115.
[171] F. T. Johra, J.-W. Lee, and W.-G. Jung, "Facile and safe graphene preparation on solution based platform," *J. Ind. Eng. Chem.*, vol. 20, no. 5, pp. 2883–2887, Sep. 2014, doi: 10.1016/j.jiec.2013.11.022.
[172] Normac Adhesives, "NR-606," *MSDS*. [Online]. Available: https://www.normacadhesives.com/. [Accessed: 19-Jan-2019].
[173] "Acetone (Certified ACS), Fisher Chemical." [Online]. Available: https://www.fishersci.ca/shop/products/acetone-certified-acs-fisher-chemical-12/a18sk4. [Accessed: 27-Jan-2019].
[174] "Methyl Ethyl Ketone (Certified ACS), Fisher Chemical." [Online]. Available: https://www.fishersci.ca/shop/products/methyl-ethyl-ketone-certified-acs-fisher-chemical-6/p-216191. [Accessed: 27-Jan-2019].
[175] "Ohaus AV313 Adventurer Pro Digital Balance, 310 x 0.001 g - Free Shipping - Coupons and Discounts May be Available." [Online]. Available: https://www.scalesgalore.com/product/index.cfm?product_id=5982. [Accessed: 09-Feb-2019].
[176] "Q500 Sonicator," *Qsonica*. [Online]. Available: https://www.sonicator.com/products/q500-sonicator. [Accessed: 27-Jan-2019].
[177] "The New EXAKT 80E Plus," *Exakt Technologies*, 30-Oct-2014. [Online]. Available: https://exaktusa.com/pharmacy-equipment/products/exakt-80eplus/. [Accessed: 28-Jan-2019].
[178] H. Gojzewski, B. Imre, C. Check, R. Chartoff, and J. Vancso, "Mechanical mapping and morphology across the length scales unveil structure–property relationships in polycaprolactone based polyurethanes," *J. Polym. Sci. Part B Polym. Phys.*, vol. 54, no. 22, pp. 2298–2310, 2016, doi: 10.1002/polb.24140.
[179] "Multipurpose X-ray diffraction system | Rigaku." [Online]. Available: https://www.rigaku.com/en/products/xrd/ultima. [Accessed: 28-Jan-2019].
[180] J. R. Connolly, "Introduction to X-ray Powder Diffraction," presented at the EPS400-002, Spring-2005.
[181] R. Jenkins and R. Snyder, *Introduction to X-Ray Powder Diffractometry*, 1 edition. New York: Wiley-Interscience, 1996.
[182] "Thermal Conductivity Analyzer - Hot Disk TPS 2500 S," *Thermtest Inc.* [Online]. Available: https://thermtest.com/tps-2500-s. [Accessed: 28-Jan-2019].
[183] E37 Committee, "Test Method for Determining Specific Heat Capacity by Differential Scanning Calorimetry," ASTM International.
[184] "Motoman HP20," *RobotWorx*. [Online]. Available: https://www.robots.com/robots/motoman-hp20. [Accessed: 10-Feb-2019].
[185] "3M™ Scotch-Weld™ Epoxy Adhesive DP460." [Online]. Available: https://www.3m.com/3M/en_US/company-us/all-3m-products/~/3M-Scotch-Weld-Epoxy-Adhesive-DP460/?N=5002385+3293241275&rt=rud. [Accessed: 12-Feb-2019].
[186] X. Zhou *et al.*, "XRD-based quantitative analysis of clay minerals using reference intensity ratios, mineral intensity factors, Rietveld, and full pattern summation methods: A critical review," *Solid Earth Sci.*, vol. 3, no. 1, pp. 16–29, Mar. 2018, doi: 10.1016/j.sesci.2017.12.002.
[187] L. Nielsen *et al.*, "Thermal conductivity of nonporous polyurethane," *High Temp.-High Press.*, vol. 32, no. 6, pp. 701–707, 2000, doi: 10.1068/htwu69.
[188] K. A. Imran and K. N. Shivakumar, "Graphene-modified carbon/epoxy nanocomposites: Electrical, thermal and mechanical properties," *J. Compos. Mater.*, vol. 53, no. 1, pp. 93–106, Jan. 2019, doi: 10.1177/0021998318780468.

[189] P. D. Thacher, “Effect of Boundaries and Isotopes on the Thermal Conductivity of LiF,” *Phys. Rev.*, vol. 156, no. 3, pp. 975–988, Apr. 1967, doi: 10.1103/PhysRev.156.975.
[190] H. Ashrafizadeh, A. McDonald, and P. Mertiny, “Erosive and Abrasive Wear Resistance of Polyurethane Liners,” 2017.
[191] T. F. Kuech, “4.01 - Integration of Dissimilar Materials,” in *Comprehensive Semiconductor Science and Technology*, P. Bhattacharya, R. Fornari, and H. Kamimura, Eds. Amsterdam: Elsevier, 2011, pp. 1–24.
[192] H. Tan, L. Jiang, ying-sheng Huang, B. Liu, and K. Hwang, “The effect of van der Waals-based interface cohesive law on carbon nanotube-reinforced composite materials,” *Compos. Sci. Technol. - Compos. SCI TECHNOL*, vol. 67, pp. 2941–2946, Nov. 2007, doi: 10.1016/j.compscitech.2007.05.016.
[193] A. Castellanos, “The relationship between attractive interparticle forces and bulk behaviour in dry and uncharged fine powders,” *Adv. Phys.*, vol. 54, no. 4, pp. 263–376, Jun. 2005, doi: 10.1080/17461390500402657.
[194] E. J. R. Parteli, J. Schmidt, C. Blümel, K.-E. Wirth, W. Peukert, and T. Pöschel, “Attractive particle interaction forces and packing density of fine glass powders,” *Sci. Rep.*, vol. 4, Sep. 2014, doi: 10.1038/srep06227.
[195] M. Götzinger and W. Peukert, “Particle Adhesion Force Distributions on Rough Surfaces,” *Langmuir*, vol. 20, no. 13, pp. 5298–5303, Jun. 2004, doi: 10.1021/la049914f.
[196] F. L. Leite, C. C. Bueno, A. L. Da Róz, E. C. Ziemath, and O. N. Oliveira, “Theoretical models for surface forces and adhesion and their measurement using atomic force microscopy,” *Int. J. Mol. Sci.*, vol. 13, no. 10, pp. 12773–12856, Oct. 2012, doi: 10.3390/ijms131012773.
[197] M. Götzinger and W. Peukert, “Dispersive forces of particle–surface interactions: direct AFM measurements and modelling,” *Powder Technol.*, vol. 130, no. 1, pp. 102–109, Feb. 2003, doi: 10.1016/S0032-5910(02)00234-6.
[198] A. B. Yu, J. Bridgwater, and A. Burbidge, “On the modelling of the packing of fine particles,” *Powder Technol.*, vol. 92, no. 3, pp. 185–194, Aug. 1997, doi: 10.1016/S0032-5910(97)03219-1.
[199] S. Ahmad Alidokht, P. Vo, S. Yue, and R. R. Chromik, “Erosive wear behavior of Cold-Sprayed Ni-WC composite coating,” *Wear*, vol. 376–377, pp. 566–577, Apr. 2017, doi: 10.1016/j.wear.2017.01.052.
[200] H. S. Grewal, A. Agrawal, and H. Singh, “Identifying Erosion Mechanism: A Novel Approach,” *Tribol. Lett.*, vol. 51, no. 1, pp. 1–7, Jul. 2013, doi: 10.1007/s11249-013-0156-4.
[201] H. Wensink and M. C. Elwenspoek, “A closer look at the ductile–brittle transition in solid particle erosion,” *Wear*, vol. 253, no. 9, pp. 1035–1043, Nov. 2002, doi: 10.1016/S0043-1648(02)00223-5.
[202] I. M. Hutchings, “Ductile-brittle transitions and wear maps for the erosion and abrasion of brittle materials,” *J. Phys. Appl. Phys.*, vol. 25, no. 1A, pp. A212–A221, Jan. 1992, doi: 10.1088/0022-3727/25/1A/033.

Appendix:

Table A1: Data Collected from erosion test of neat PU and GNP-PU nanocomposite samples

GNP wt (%)	Dispersion Method	Temp (°C)	Sample Weight Before Erosion (mg)	Sample Weight After (mg)	Grit weight Before (g)	Grit weight After (g)	Weight Loss of Sample (mg)	Weight of Grit (g)	Erosion Rate (mg/g)
0%	-	22	40.321	40.315	555	337	0.006	218	0.03
0%	-	60	39.916	39.873	561	376	0.043	185	0.23
0%	-	100	41.182	41.016	645	446	0.166	199	0.83
1%	Sonicated	22	41.052	41.02	664	469	0.032	195	0.16
1%	Sonicated	60	40.7	40.658	592	407	0.042	185	0.23
1%	Sonicated	100	41.136	41.084	445	262	0.052	183	0.28
1%	3RM	22	41.502	41.482	626	421	0.02	205	0.10
1%	3RM	60	42.742	42.701	407	213	0.041	194	0.21
1%	3RM	100	41.111	41.06	803	623	0.051	180	0.28
2%	Sonicated	22	40.847	40.816	624	426	0.031	198	0.16
2%	Sonicated	60	39.597	39.556	864	713	0.041	151	0.27
2%	Sonicated	100	40.256	40.206	623	419	0.05	204	0.25
2%	3RM	22	41.231	41.208	502	285	0.023	217	0.11
2%	3RM	60	42.707	42.664	713	561	0.043	152	0.28
2%	3RM	100	41.245	41.173	419	225	0.072	194	0.37
3%	Sonicated	22	39.795	39.766	538	337	0.029	201	0.14
3%	Sonicated	60	40.95	40.912	561	365	0.038	196	0.19
3%	Sonicated	100	40.185	40.126	908	741	0.059	167	0.35
3%	3RM	22	41.186	41.163	520	315	0.023	205	0.11
3%	3RM	60	41.131	41.1	365	189	0.031	176	0.18
3%	3RM	100	41.312	41.275	741	547	0.037	194	0.19
4%	Sonicated	22	39.987	39.968	521	291	0.019	230	0.08
4%	Sonicated	60	40.437	40.418	953	802	0.019	151	0.13
4%	Sonicated	100	40.895	40.85	761	573	0.045	188	0.24
4%	3RM	22	41.082	41.075	722	561	0.007	161	0.04
4%	3RM	60	41.595	41.577	802	645	0.018	157	0.11
4%	3RM	100	41.915	41.875	573	372	0.04	201	0.20

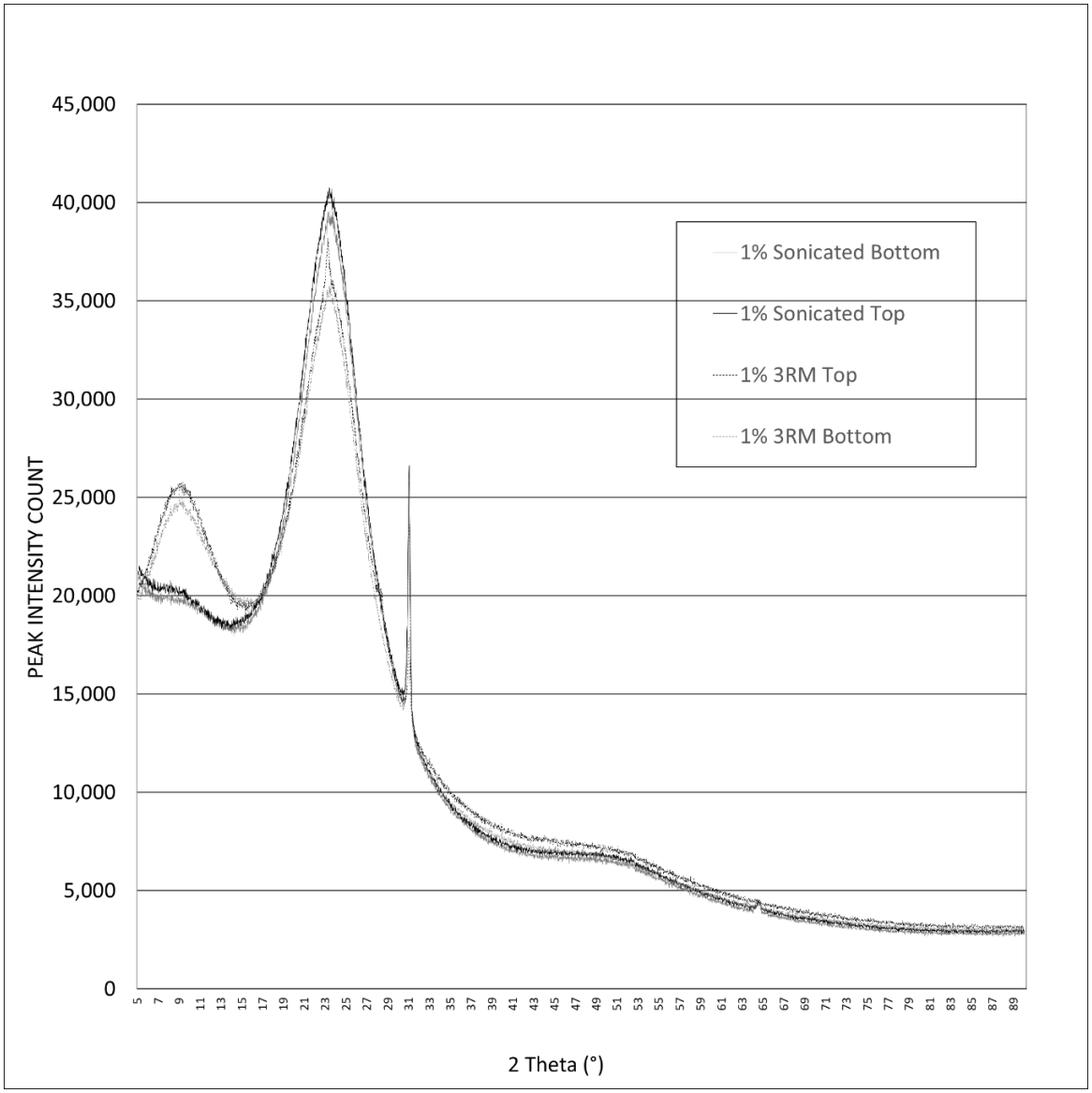

Figure A1: XRD of top and bottom surface of 1 wt% GNP-PU$_S$ and 1 wt% GNP-PU$_{3RM}$

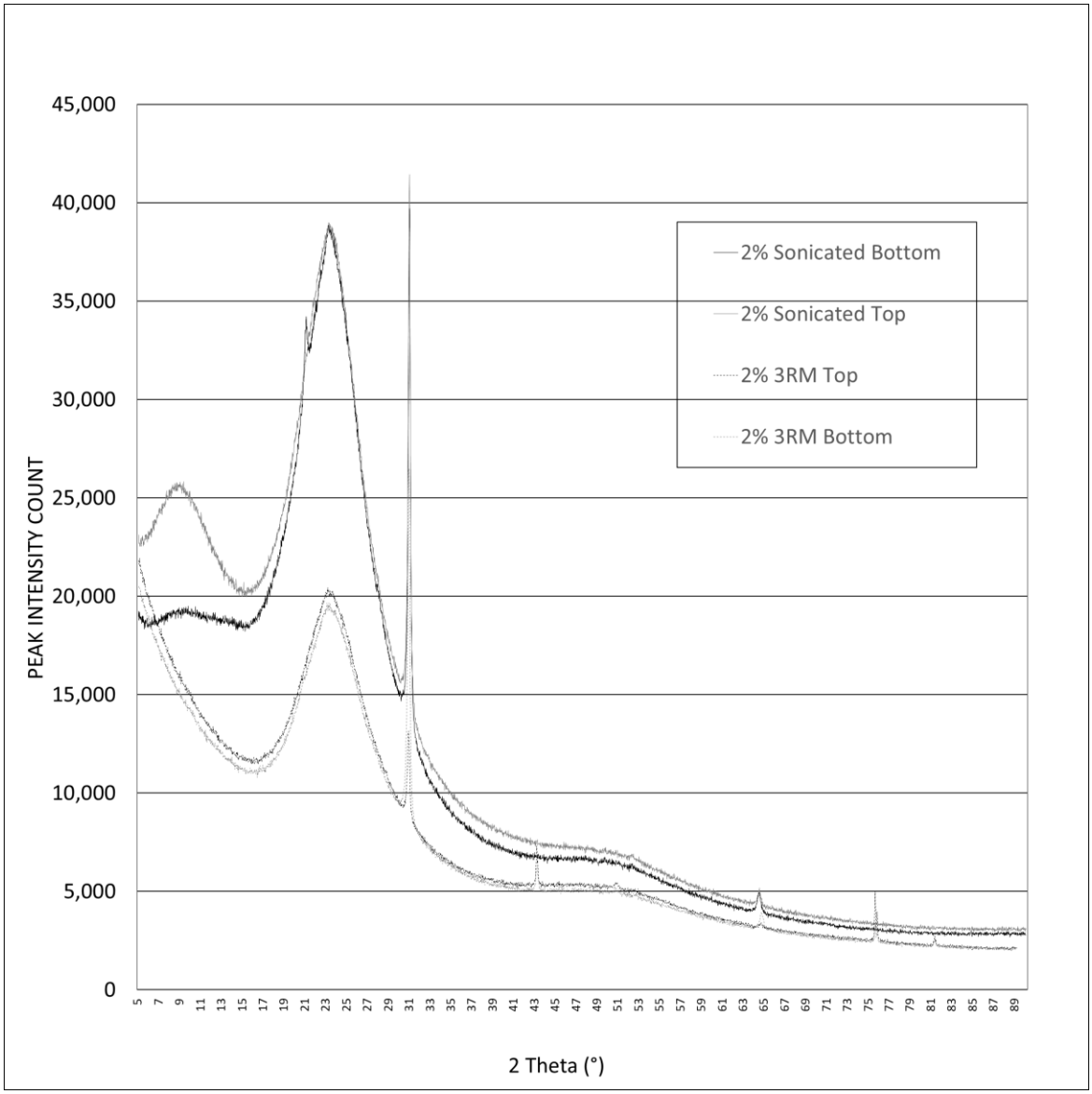

Figure A2: XRD of top and bottom surface of 2 wt% GNP-PU$_S$ and 2 wt% GNP-PU$_{3RM}$

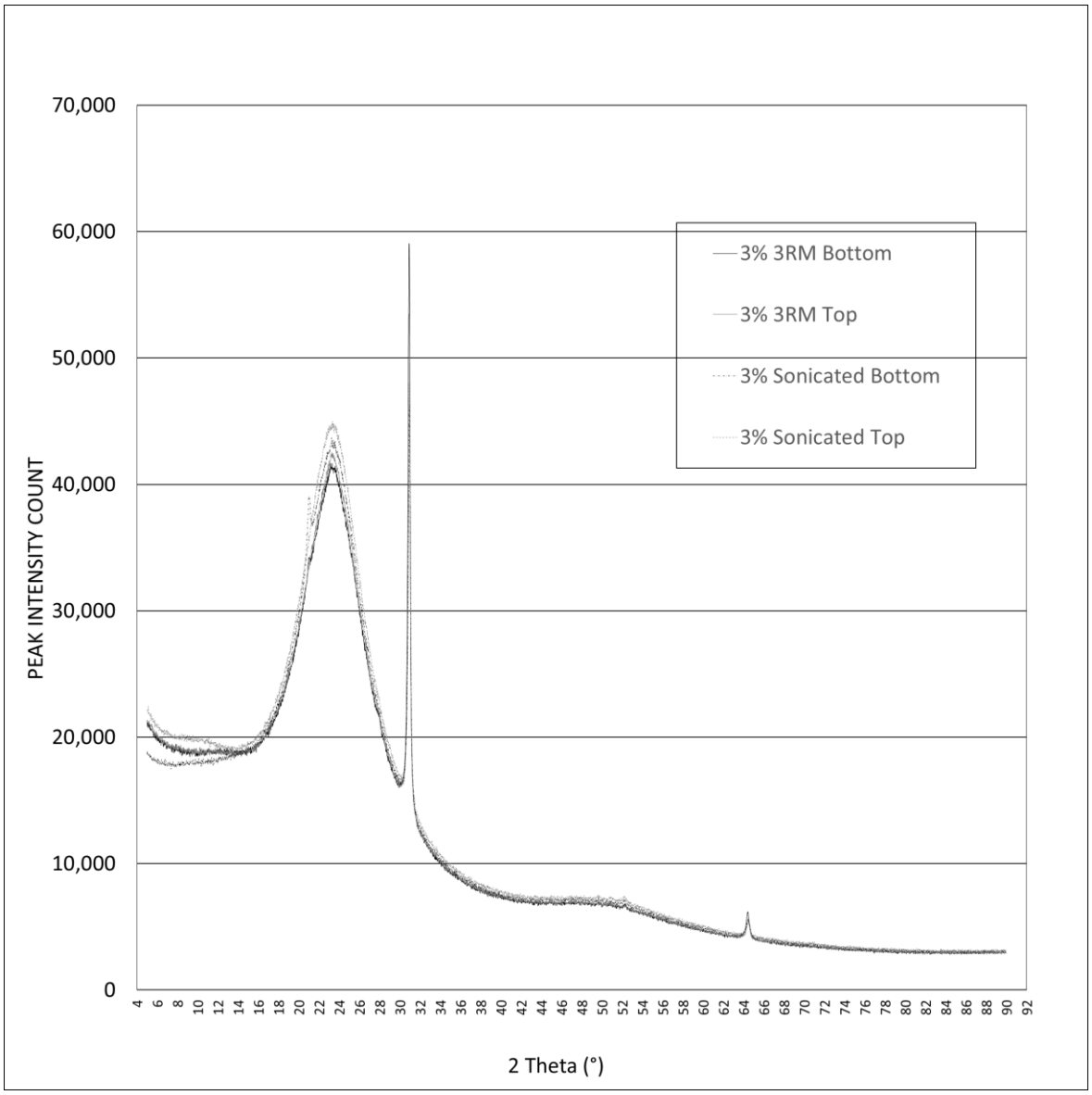

Figure A3: XRD of top and bottom surface of 3 wt% GNP-PU$_S$ and 3 wt% GNP-PU$_{3RM}$

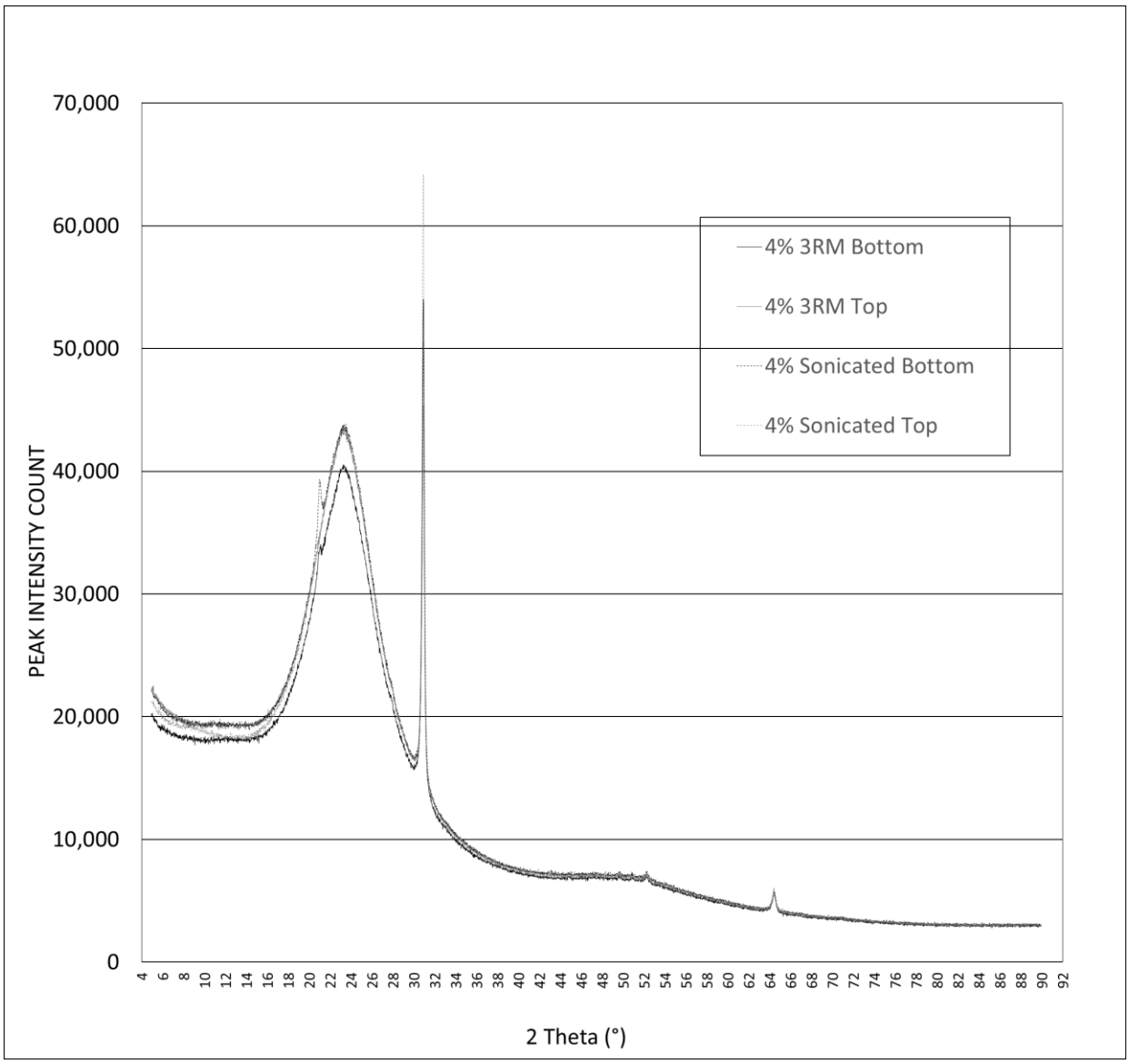

Figure A4: XRD of top and bottom surface of 4 wt% GNP-PU$_S$ and 4 wt% GNP-PU$_{3RM}$

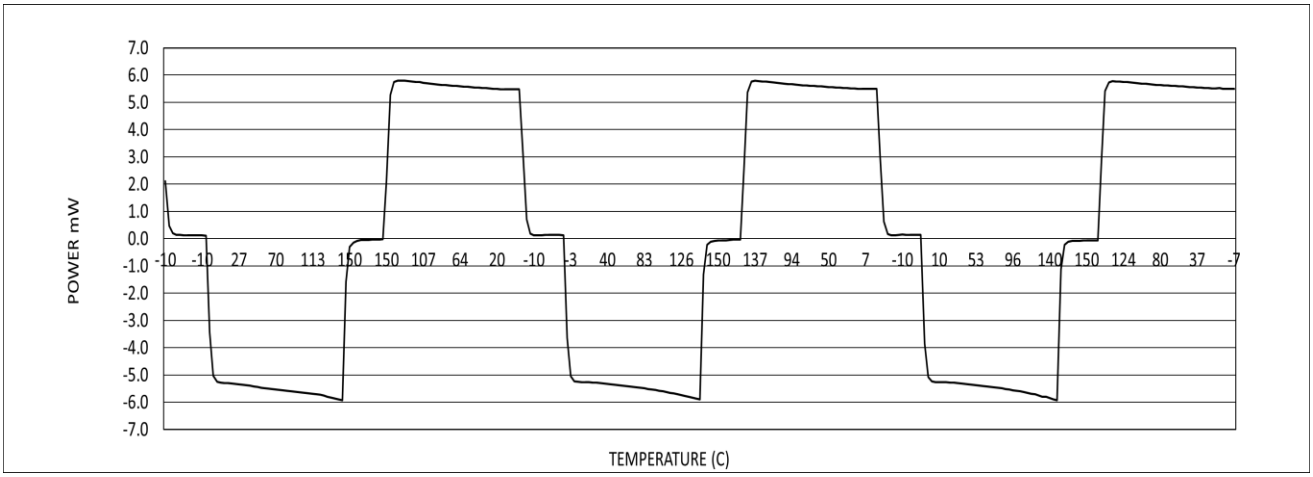

Figure A5: DSC graph of neat Polyurethane